GAUSSIAN BEAM-MODE CIRCUITS FOR MILLIMETRE WAVELENGTHS

by

Richard John Wylde

Department of Physics, Queen Mary College

A Thesis submitted in accordance with the regulations for the degree of Doctor of Philosophy in the University of London

1985

ABSTRACT

Although the Maxwell equations govern the propagation of EM waves at all frequencies, the methods required to generate, direct, analyse and detect radiation differ from band to band.

This thesis is concerned with the development and demonstration of 'Quasi-optical' techniques for millimetre wavelengths, which involve the propagation of Gaussian profiled beams a few wavelengths across, and the realization of a general circuit approach to mm-wave measurement.

Gaussian beam-mode analysis, which is used in later chapters to understand propagation of quasi-optical beams, is reviewed in chapter 1.

Chapter 2 outlines the design, manufacture and testing of corrugated feed horns which generate fundamental Gaussian beam-modes.

The design and manufacture of lenses which control the spreading of the beams and directional couplers which provide desirable signal processing functions in quasi-optical circuits is discussed in chapter 3. Chapter 4 traces the development of a Faraday isolator which operates in free-space and can suppress unwanted reflections in quasi-optical circuits. Chapter 5 discusses a reusable circuit board upon which systems can be easily and quickly constructed. A null reflectometer built using quasi-optical components is outlined in chapter 6 and reflection measurements from lenses and horns presented.

Chapter 7 describes a corrugated feed horn/lens antenna used in a balloon-borne mm-wave cosmic background experiment. Finally, Chapter 8 demonstrates the use of quasi-optical components in a 115 GHz receiver circuit.

ACKNOWLEDGEMENTS

The work described in this thesis would not have been possible without the advice and encouragement of my co-directors and colleagues in Thomas Keating Ltd. I would like to record my special thanks to John White, John Trott, Clive Stevens and Ian Coomber.

Much assistance has come from past and present members of the Engineering Physics Group at Queen Mary College: David Adamson, Kathy Boydon, Dr. Jacqueline Card, Paul Carnie, Dr Nigel Cronin, Dr Y'Quian Gong, Dr Jim Lesurf, Richard Martin, Graham Poulson and Eddie Puplett. I am also indebted to Mr. Fred Hands and the Physics department workshop and Professor David Olver of the Electrical Engineering department. Emeritus Professor W.L. Wilcock of University College of North Wales, Bangor, has given invaluable advice.

Although not directly connected with this work, my past teachers and supervisors are responsible for fostering an interest in Physics and Engineering Design: I owe a debt to Dr. Gerald Bettridge and Christopher Ellis of Eton College and Dr Paul Scott of Sidney Sussex College, Cambridge.

Long term support has come from my family and my fiancee Lucy: my late mother and father always encouraged me to persevere with worthwhile tasks.

Finally, and most importantly, I would like to record my appreciation and thanks to Professor Derek Martin who allowed me to join his research group under unusual circumstances and has been a constant source of ideas, advice and encouragement during the last six years.

CONTENTS

ABSTRACT 2

ACKNOWLEDGEMENTS 3

INTRODUCTION 6

CHAPTER 1 GAUSSIAN BEAM-MODES AND QUASI-OPTICAL CIRCUITS

1.1 Introduction 9
1.2 The propagation of Gaussian beam-modes 10
1.3 Beam confinement 14
1.4 Maximum throw of Gaussian beam-modes 16
1.5 Quasi-optical networks 18

CHAPTER 2 CORRUGATED HORNS

2.1 Introduction 20
2.2 Modes in corrugated waveguide 21
2.3 Excitation of the HE_{11} mode 26
2.4 Corrugated horn design 28
2.5 Gaussian beam-mode analysis of the operation of corrugated horns 29
2.6 The manufacture of corrugated horns 49
2.7 The measurements of performance of corrugated horns 57
2.8 Conclusion 68

CHAPTER 3 POLARIZING DIRECTIONAL COUPLERS AND BEAM-CONTROL LENSES

3.1 Introduction 72
3.2 Polarizing grids 72
3.3 Lens design 73
3.4 The choice of lens material 74

CHAPTER 4 QUASI-OPTICAL ISOLATORS

4.1 Introduction 81
4.2 The operation of a Faraday isolator 81
4.3 Previous measurements on Ferrite materials 90
4.4 The design of a small quasi-optical isolator 91
4.5 Measurements of the performance of the ferrite rotator and isolator 95
4.6 Conclusion 110

CHAPTER 5 A BUILDING-BLOCK APPROACH TO QUASI-OPTICAL CIRCUITS

5.1 Introduction 111
5.2 The size of quasi-optical circuits 111
5.3 The design of split-cube building blocks 112

CHAPTER 6 A QUASI-OPTICAL NULL REFLECTOMETER

6.1 The null reflectometer 116
6.2 A Jones matrix analysis of the reflectometer 120

6.3 Effect of instrument error on the measured reflection coefficient 123
6.4 Measurements using the reflectometer 124

CHAPTER 7 THE DESIGN AND TESTING OF HORN ANTENNAS FOR A COSMIC BACKGROUND EXPERIMENT

7.1 Introduction 127
7.2 A cosmic background radiometer 128
7.3 The antenna for CBS 129
7.4 Forming the beam 131
7.5 Single mode operation 131
7.6 Horn/lens performance 136
7.7 Reflections from the 'back-to-back' horn 140
7.8 Conclusion 142

CHAPTER 8 THE DESIGN AND TESTING OF THE QUASI-OPTICAL PART OF A 115 GHz RECEIVER

8.1 Introduction 143
8.2 The 115 GHz superheterodyne receiver 144
8.3 Quasi-optical systems 144
8.4 Receiver performance measurements 147
8.5 Conclusions 150

CHAPTER 9 CONCLUSIONS 151

APPENDIX I 153

APPENDIX II 161

REFERENCES 164

INTRODUCTION

The millimetre-wave region of the electromagnetic spectrum, between the microwave and infrared bands, is of growing interest to scientists and communication engineers. In cosmology, measurements of the 3 K microwave background at mm wavelengths bear crucially on our knowledge of the very early stages of the big-bang universal expansion. In astronomy, mm-wave measurements are revealing the existence of massive cool clouds of gas and dust in interstellar space which are collapsing under gravitation to form new stars. In experiments on the magnetically confined plasmas of controlled nuclear fusion research (such as Euratom's JET project) electron cyclotron emission at mm wavelengths provides a major diagnostic tool. In communications engineering, inter-satellite communications, remote sensing of weather from space, and high resolution radar are among the applications for mm-waves currently being developed. This thesis is concerned with techniques for measurements at wavelengths from 3 mm to 1 mm which have relevance to each of the above fields of application.

The mm region of the electromagnetic spectrum is an area in which neither the geometrical optical or "wave-directing", nor the microwave or "wave-guiding" techniques, work well. The size of conventional waveguide scales with wavelength; waveguide systems could in principle be built for frequencies above 75 GHz, but manufacturing problems when guides are less than 2 by 1 mm become extremely difficult and optimum performance cannot be maintained. Geometrical optical systems in the IR have high efficiency but to maintain the integrity of the geometrical optical approach the components must be many wavelengths across and for the mm region this requirement would result in huge components.

This thesis is concerned with the development of techniques which involve both wave-directed and wave-guided propagation in a single system. The beams in free space are only a few wavelengths across, hence the term "quasi-optical". Close attention therefore has to be applied to the effects of diffractive spreading of the beams. Gaussian beam-mode analysis of diffractive spreading has previously been used in the contexts of the open resonators of gas lasers and of graded-index optical fibres. Gaussian beam-mode analysis has more recently been used in the development of a general circuit approach to quasi-optical measurement systems (Chapter 1). To realise this approach it was necessary to identify, design, and manufacture the following quasi-optical circuit components, and this is the main concern of the first part of the work described in this thesis.

First, a component that generates a fundamental Gaussian beam-mode was essential. The second chapter is concerned with the development of corrugated feed horns which do this. The chapter covers the theory, construction and testing and use of such horns at mm wavelengths.

Secondly, lenses which control the spreading of the beams and directional couplers which, in combination, provide desirable signal processing functions, were required. These are described in Chapter 3.

Thirdly a free-space Faraday isolator has been developed and is described in Chapter 4. This component is important because coherent mm wave sources are prone to frequency destabilisation caused by reflections back into the source.

Lastly there was a need to construct a reusable circuit board upon which systems could be easily and quickly constructed.

An idea based on a split brass cube which can hold both lenses and a polarizing directional coupler at the correct angles was adopted, and is outlined in Chapter 5. A quasi-optical null reflectometer built using these split brass cubes is described in Chapter 6.

The second part of this thesis is concerned with the demonstration of the use of quasi-optical circuits in two contexts: as a major component in a balloon-borne mm-wave cosmic background experiment (Chapter 7) and as a major part of a 115 GHz receiver (Chapter 8).

In the final chapter the efficacy of the quasi-optical circuitry developed in the course of the work described here is reviewed.

CHAPTER 1

GAUSSIAN BEAM MODES AND QUASI-OPTICAL CIRCUITS

1.1 Introduction

This chapter considers the problems associated with the development of systems operating in the millimetre-wave region, between the microwave and infrared bands. It outlines a quasi-optical approach to circuit design. The mathematical theory of Gaussian beam-mode analysis, which is used in subsequent chapters to design components, is reviewed. Finally the notion of quasi-optical signal-processing networks is discussed.

Although the Maxwell equations govern the propagation of EM waves at all frequencies, the techniques required to generate, direct and detect radiation differ from band to band. Both the "wave-directing" geometrical optical technique used in the IR and the "wave guiding" microwave technique suffer from limitations when applied in the millimetre-wave band. Geometrical optical systems will be limited by diffraction. Consider a beam truncated by an aperture. Diffraction causes the angular spread of the beam to be greater on the emergent side by an amount of order λ/a where λ is the wavelength and a the linear dimension of the aperture. If $a \gg \lambda$ the effect is negligible, but if the aperture is only a few wavelengths across it cannot be ignored. Thus because the wavelength is small in the IR it is easy to construct components whose sizes are many wavelengths across and beams therefore do not suffer from significant diffractive spreading. However at mm wavelengths the equivalent components would be huge, and therefore cumbersome.

In the microwave band, "waveguiding" techniques using conducting tubes or waveguides work well. It is often said that ohmic losses in

the walls of waveguides set a limit to the highest frequency at which waveguides can operate. If one scales all waveguide dimensions with wavelength, losses increase with the square root of the frequency. However, at millimetre wavelengths, the real limitation is in the practical problems of manufacturing waveguides, tuning plungers, and junctions, whose *internal* surfaces need to be made to fractional tolerances of better than 1%, when the waveguide size drops below 2 by 1 mm. It is for this practical reason that waveguide techniques are not appropriate for mm-wave systems.

The present work uses a technique called "quasi-optics" which tries to overcome the deficiencies in both the IR "wave-directing" and the microwave "waveguiding" methods. The technique is "quasi-optical" because the width of beams is only a few wavelengths across. These beams diffractively spread out as they propagate, but this diffraction is precisely controlled by lenses. The beams, whose profiles are Gaussian in form, are generated and received by corrugated waveguide feed horns which taper down to short sections of waveguide to allow matching to low-impedance active devices such as detectors and sources. Since a mathematical theory of Gaussian beam-modes is used to understand the operation of quasi-optical components it is necessary first to review Gaussian beam-mode analysis.

1.2 The propagation of Gussian beam-modes

Kogelnik and Li [1.1] (see also the reviews by Goldsmith [1.2], Martin and Lesurf [1.3], Martin [1.4] or the books by Marcuse and Arnaud [1.5]) show that a solution of the time independent scalar wave equation

$$\nabla^2 \psi + k_o^2 \psi = 0 \,, \qquad (1.1)$$

(where ψ is the amplitude of the scalar wave and the wavenumber $k_o = {}^{w}/_{c}$ where $\frac{2}{2\pi}$ is the frequency of the wave) for a beam propagating in the z-axis can be represented as a superposition of an orthogonal set of propagating Gaussian-Laguerre modes (cylindrical coordinate system) or Gaussian-Hermite modes (cartesian coordinate system), provided that the beam is paraxial in the sense that $\frac{\partial^2 \psi}{\partial z^2}$ is much smaller than $2 k_o \frac{\partial \psi}{\partial z}$ and can therefore be neglected. Restricting ourselves to axially symmetrical solutions of the wave equation expressed in cylindrical coordinates

$$\psi(r,z) = \sum_{p=0}^{\infty} A_p \left[\frac{2}{\pi w^2}\right]^{1/2} L_p^o\left[\frac{2r^2}{w^2}\right] \exp\left\{-i\left[\frac{k_o r^2}{2q}\right] + \phi_p\right\} e^{-ik_o z}, \qquad (1.2)$$

where $p = 0, 1, 2, 3 \ldots$, and $L_p^o(x)$ is a zero-order Laguerre polynomial, e.g.

$$L_o^o(x) = 1, \qquad L_1^o(x) = 1 - x, \qquad L_2^o(x) = 2 - 4x + x^2 \quad \text{and}$$

$$L_3^o(x) = 6 - 18x + 9x^2 - x^3.$$

The parameter q is given by

$$\frac{1}{q} = \frac{1}{R} - \frac{2i}{k_o w^2} \,, \qquad (1.3)$$

where R is the radius of curvature of the equiphase surface, and W is a measure of the width of the mode in the xy plane. The second parameter ϕ_p is a phase-slippage associated with the non-planar phase front of the beam. R, W and ϕ are dependent on z, specifically:

$$R = (z - z_o)\left[1 + \frac{1}{z^2}\right] \,, \qquad (1.4)$$

$$W^2 = W_o^2 \left[1 + \ddot{z}^2\right] , \tag{1.5}$$

$$\phi_p = (2p+1) \tan^{-1} \ddot{z} , \tag{1.6}$$

Here $\ddot{z}$ is the reduced (dimensionless) distance to the beamwaist, i.e. the xy plane in which the beam has its minimum size: it is defined by

$$\ddot{z} = \frac{\lambda (z - z_o)}{\pi W_o^2} , \tag{1.7}$$

where z_o and W_o are the values of z and W at the beamwaist (the wavelength λ is $2\pi/k_o$, i.e. $2\pi c/w$).

From given values of W, R and ϕ_p in one xy plane, one can easily calculate the values in any other xy plane. Note especially that R and W do not depend on the mode number p, but ϕ_p does. (Figure 1a displays R and W as a function of $z-z_o$.)

Dividing (1.5) by (1.4) and substituting (1.7) gives the useful relation for any xy plane

$$\frac{W^2}{R} = \frac{\lambda}{\pi} \ddot{z} , \tag{1.8}$$

which can be used to express W_o and $z-z_o$ in terms of W and R:

$$W_o^2 = \frac{W^2}{\left[1 + \left[\frac{\pi W^2}{\lambda R}\right]^2\right]} , \tag{1.9}$$

$$z-z_o = \frac{R}{\left[1 + \left[\frac{\lambda R}{\pi W^2}\right]^2\right]} . \tag{1.10}$$

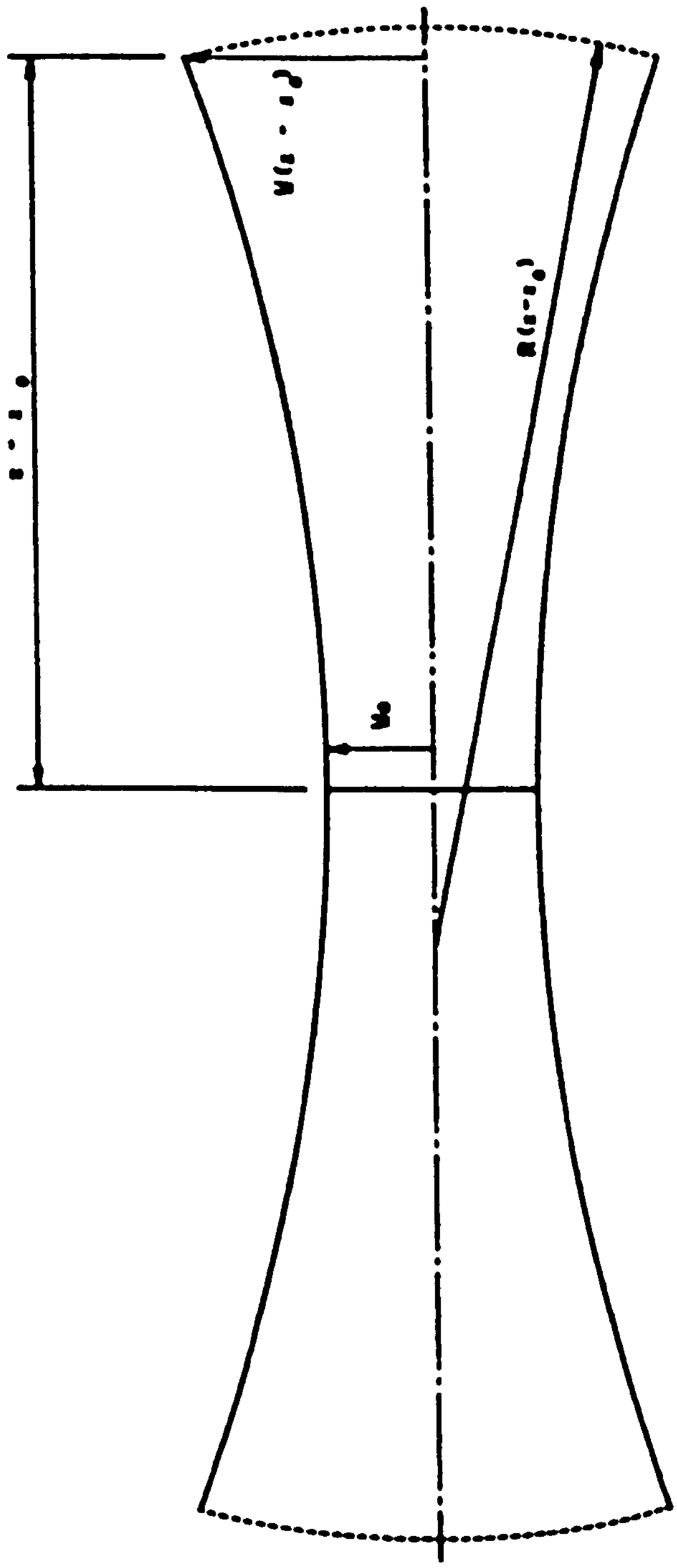

Fig. 1

Although $\psi(r,z)$ is a solution to the <u>scalar</u> wave equation, it can be used to represent orthogonal components of electromagnetic vector fields propagating with the same paraxial assumptions. Indeed the electric and magnetic conponents of any vector solution to Maxwell's equations must satisfy the scalar wave equation. Appropriate combinations of the electric field components then ensure that $\nabla.\underline{E} = 0$.

One can therefore represent the transversely polarized $\underline{E}$ field components of any coherent (single frequency) propagating electromagnetic wave by $\psi(r,z)$ multiplied by an appropriate complex coefficient. Suppose we use a cartesian coordinate system. Then let $E_x = A\,\psi(r,z)$, $E_y = B\,\psi(r,z)$, where A and B are amplitude coefficients. Then for an x polarised wave $A = E_o$, $B = 0$ and similarly for a y polarized wave, $B = E_o$ and $A = 0$. Diagonally polarized waves are given by $A = B = E_o/\sqrt{2}$. Other linearly polarized waves are given by appropriate real combinations of A and B, elliptical polarizations require complex values of A and B. For example, a circularly polarized wave is given by $A = E_o/\sqrt{2}$, $B = iE_o/\sqrt{2}$.

The integral of $\psi(r,z)^*\psi(r,z)$ over any cross-sectional plane is proportional to the power carried by the beam and is the same for all z, equal to $\sum_{p=0}^{\infty} A_p^{o\,2}$ indicating that power is conserved as the beam propagates. We shall hereon call any of the modes represented by equation 1.2 simply a Gaussian beam-mode.

1.3 Beam confinement

One immediate advantage of representing a paraxial beam as a super-position of independently propagating Gaussian beam-modes is that it is easy to determine the effect of placing an ideal lens on the axis of the beam; it causes a discrete change in the radius

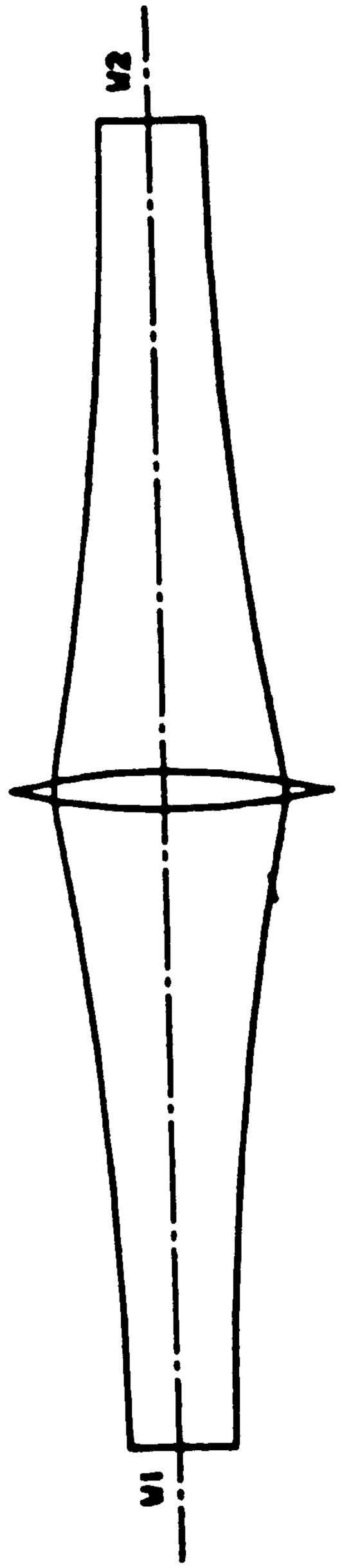

FIG. 1 b IDEAL LENS COUPLING

of curvature of the phase front of each mode but without disturbing the amplitude distribution over the cross-section.

$$\Delta \left[\frac{1}{R}\right] = \frac{1}{f} \quad , \tag{1.11}$$

where f is the focal length of the lens. It is therefore possible to determine W_2 and z_2, the size and position of the waist of the beam emerging from a lens of a given power, provided the beam size W_1 and phase radius of curvature R_1 of the incoming beam at the lens are known. See Fig. 1b.

1.4 Maximum throw of Gaussian beam-modes

The following result from Gaussian beam-mode analysis, derived by Martin [1.6], is important in the design of quasi-optical circuits: if the beam width at a lens is W, there is no choice of focal length that would give a beam-waist at a distance from the lens greater than $\pi W/2\lambda$. One can prove this result by differentiating (1.10) with respect to R and equating the RHS to zero. This result means that the maximum distance of propagation from the lens before the beam diverges beyond the width W is $\pi W^2/\lambda$. To achieve this maximum throw, the focal length should be such that the radius of curvature of the beam as it leaves the lens is $\pi W^2/\lambda$ and, for this critical condition, the beamwaist will be $W_o = W/\sqrt{2}$ and the distance between lens and beam-waist will correspond to $\bar{z} = 1$. If the incident and emergent beams at a lens are <u>both</u> maximum-throw beams of width W at the lens, the radii of curvature of the incident and emergent beams will both be equal to $\pi W^2/\lambda$ and the focal length of the lens will therefore be $\pi W_o/\lambda$. Thus the beam-waists for the incident and emergent beams are both at a distance f from the lens.

This result applies not only to the fundamental but to all Gaussian beam-modes because W and R are the same for all modes having the same beamwaist W_o. It is, however, necessary to consider the relative phases of the different modes. In a maximum-throw lens train, the mode of mode-number p will suffer a phase-slip $2(2p+1)\pi/4$ between successive lenses. Thus, with a chain comprising an even number of lenses, even and odd Gaussian beam-modes suffer phase changes differing by 180°, while for an odd number of lenses, all modes will suffer the same phase change (modulo 2π). The latter condition is helpful but it must be noted that additional phase-slippages will occur between the lenses and feed-horns at the ends of the train which, in general, will not be multiples of $\pi/4$. Because there is such a phase slippage, the input and output horns may not be ideally coupled by a lens train. The problem of evaluating the coupling is pursued further in Chapter 2.

In quasi-optical circuits the lenses must be sufficiently large that beam-truncation and consequent mode-mixing is kept below acceptable limits. For a beam containing only low-order Gaussian beam-modes, the power falls away rapidly for $r > W$. For example, for a fundamental mode, the power outside a circle of diameter 3W is 20 dB down on the total power. The effect of truncation of a beam at an aperture is mode conversion to higher order Gaussian beam-modes which, being non-paraxial, will not follow the intended paths through the system and will be lost. The Geometric Theory of Diffraction (GTD) indicates that the power lost in this way will not exceed that falling outside a circle approximately one wavelength less than the aperture in radius. We have therefore adopted the value 3W for the diameter D of lenses used in the quasi-optical circuits developed in later chapters. L, the maximum-throw distance between lenses, is then

$$L = 2f = \frac{\pi}{\lambda}\left[\frac{D}{3}\right]^2 . \qquad (1.12)$$

This relation is the starting point for the calculations of the size of the split-cube circuit components described in Chapter 5.

1.5 Quasi-optical networks

The previous section has discussed linear propagation of Gaussian beam-modes whose diffractive spreading is controlled by lenses. It is possible to construct directional couplers using polarizing wire grids (Chapter 3). Beams can easily be split and combined in varying amplitudes and polarizations. The utility to split and combine beams allows the construction of multi-port networks. The effect of a network can be completely described by a scattering matrix which [1.7] relates the output from the network to the input signals to it.

The microwave circuit designer has available a range of waveguide components, such as Hybrid T's, EH tuners, isolators and directional couplers, from which to construct circuits. The action of each component is well known and it is possible to design circuits by considering only the effect of each component: knowledge of its internal workings is not necessary. This is possible because the effect of a component in a circuit can also be completely described by a scattering matrix. The effect of an interconnected set of components can be calculated by simple matrix algebra.

It is a central proposition of this thesis that waveguide components have quasi-optical analogues. For example, the analogue of a straight piece of waveguide is a correctly formed train of lenses. A plane mirror set at 45° to an oncoming beam is equivalent to a 90° waveguide bend. Polarising grids serve as directional couplers. A quasi-optical isolator can be made using two correctly fixed polarising wire grids and an impedance-matched piece of suitable Ferrite

placed at a beam-waist. A 'building block' approach to the assembly of a system similar to that used by microwave engineers is therefore possible using quasi-optical components at mm wavelengths. The benefits of such an approach will be considerable: knowledge and experience of waveguide system design will be directly transferable to the mm region. The extent to which this approach has been realised is reviewed in the final chapter.

CHAPTER 2

CORRUGATED HORNS

2.1 Introduction

The theory and design of waveguide-fed corrugated horns which launch and receive Gaussian beam-modes are presented in this chapter and the manufacture and testing of horns described.

The chapter starts with a consideration of previous work on the propagation and excitation of modes in corrugated waveguide, especially in relation to their field characteristics (Sections 2.2 and 2.3). An understanding of these modes is a prerequisite to the understanding of why corrugated horns can generate fields in their apertures which couple well to low order Gaussian beam-modes.

Use is then made of the dispersion equation to show that the HE_{11} mode in a corrugated guide with a large radius has an axially symmetric plane polarized $\underline{E}$ field distribution over a wide frequency band (Section 2.4).

The coupling of this field to Gaussian beam-modes is then derived (Section 2.5). Just under 98% of the power radiated from a corrugated horn is found to be in the fundamental mode. Corrugated horns are therefore almost ideal for launching and receiving fundamental Gaussian beam-modes. To illustrate the power of the Gaussian beam-mode approach to the understanding of corrugated horns, the antenna patterns of horns are obtained using an analysis in terms of Gaussian beam-modes and these are compared with patterns produced using the standard Fresnel integral method. The Gaussian beam-mode method is also used to predict the phase centres of horns and the maximum coupling between them.

The work done to manufacture such corrugated horns is then outlined in Section 2.6. For this, the facilities at Thomas Keating Ltd. for the manufacture of high precision moulds and press tools were made available to us.

Finally, a microprocessor-driven antenna range which was designed and assembled to measure the antenna patterns of horns is described and the patterns obtained with both smooth and corrugated horns are presented as 2D contour plots. They confirm the expectation, based on the analysis referred to above, that corrugated horns produce axially symmetrical patterns with low sidelobes and near-Gaussian forms.

2.2 Modes in corrugated waveguide

We start by summarising the results of the work of Clarricoats [2.1] and others [2.2] who investigated theoretically the propagation of modes in cylindrical corrugated guide having infinitely thin fins and a pitch much smaller than the wavelength of forward propagation in the guide. We show that their results do not depend critically on the depth of the corrugations.

It is found that the fields of the forward propagating modes can be represented as superpositions of the TE and TM fields which separately are the modes of propagation in smooth circular guide. In smooth guide the TE and TM fields propagate separately (with different values of the forward propagation vector β). In corrugated guide the true modes are inseparable superpositions with well defined β and are often called hybrid modes.

Writing γ for the relative amplitudes of the TE and TM-like components of the 'hybrid' mode, omitting the phase factor $e^{i(\omega t+m\phi-\beta z)}$, the electric and magnetic field components obtained in [2.2] are as follows:

In the region $r < a$ (see Fig. 2a),

$$E_z = J_m(k_c r) \quad , \tag{2.1a}$$

$$H_z = -\frac{i}{Z_o}\gamma J_m(k_c r) \quad , \tag{2.1b}$$

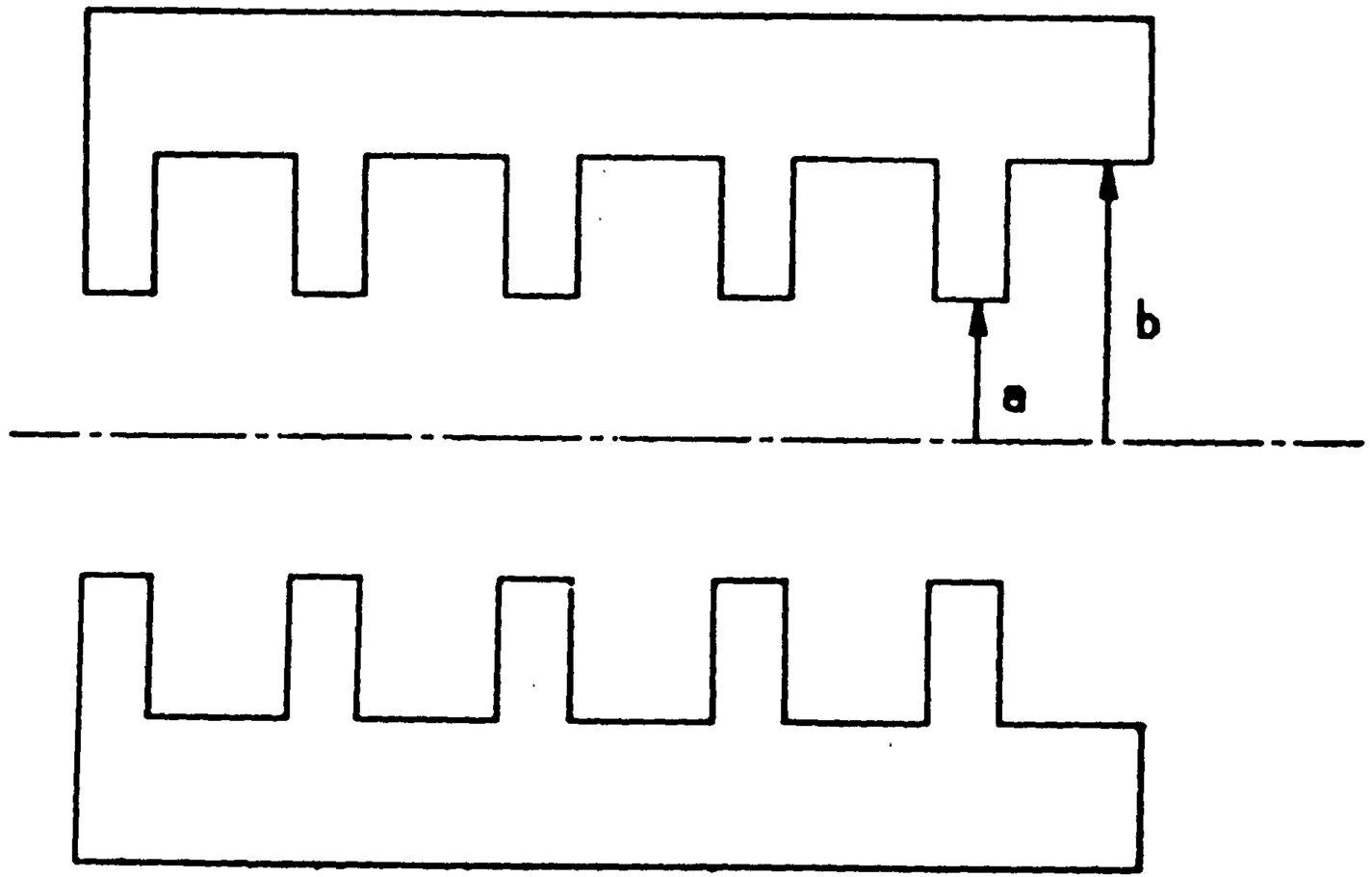

Fig. 2a

$$E_r = - i \frac{k_o}{k_c} \left[\beta' J_m(k_c r) + \gamma m \frac{J_m(k_c r)}{k_c r} \right] , \qquad (2.1c)$$

$$E_\phi = \frac{k_o}{k_c} \left[m \beta' \frac{J_m(k_c r)}{k_c r} + \gamma J'_m(k_c r) \right] , \qquad (2.1d)$$

$$H_r = - \frac{k_o}{Z_o k_c} \left[\beta' \gamma J'_m(k_c r) + m \frac{J_m(k_c r)}{k_c r} \right] , \qquad (2.1e)$$

$$H_\phi = - i \frac{k_o}{Z_o k_c} \left[m \beta' \gamma \frac{J_m(k_c r)}{k_c r} + J'_m(k_c r) \right] . \qquad (2.1f)$$

Here k_c is a parameter whose value is to be chosen to satisfy boundary conditions at r = a and r = b (see below) and can be regarded as a transverse wave-vector,

m is the azimuthal mode number,

$\beta' = \beta / k_o$ where $k_o \equiv \omega / c$, and β is the forward wave-vector,

$\beta^2 = k_o^2 - k_c^2$,

Z_o is the impedence of free space,

$J_m(x)$ are Bessel functions of the 1^{st} kind,

and ' indicates differentiation with respect to x.

In the region $a \leq r \leq b$,

$$E_z = c_m [J_m(k_o r) Y_m(k_o b) - Y_m(k_o r) J_m(k_o b)] , \qquad (2.2a)$$

$$H_\phi = - i \frac{c_m}{Z_o} [J'_m(k_c r) Y_m(k_o b) - Y'_m(k_o r) J_m(k_o b)] , \qquad (2.2b)$$

$$H_r = - \frac{m}{Z_o k_o r} E_z , \qquad (2.2c)$$

$$E_\phi \approx E_r \approx H_z \approx 0 , \qquad (2.2d)$$

where c_m is an amplitude coefficient determined by the boundary conditions and $Y_m(x)$ are Bessel functions of the 2nd kind. No E_ϕ and E_r components are permitted because of the presence of the fins.

Boundary conditions on the fields at the surfaces of the guide are used to give the values of the unknown parameters γ and k_c.

As $E_\phi = 0$ at $r = a$ then, from 2.1d

$$\gamma = - \frac{m \beta' J_m(k_c a)}{k_c a \; J'_m(k_c a)} \quad . \tag{2.3}$$

The condition that E_z and H_ϕ be continuous at $r = a$ requires that k_c satisfy the dispersion equation:

$$k_c a \; \frac{J'_m(k_c a)}{J_m(k_c a)} - \frac{(m\beta')^2 J_m(k_c a)}{k_c a \; J'_m(k_c a)} = - \frac{(k_c a)^2}{k_o a} \cdot \frac{Z_o}{X_{slot}} \quad , \tag{2.4}$$

where $X_{slot} = -\left[\dfrac{J_m(k_c a)Y_m(k_c b) - J_m(k_o b)Y_m(k_o a)}{J'_m(k_c a)Y_m(k_o b) - J_m(k_o b)Y'_m(k_o a)} \right] Z_o \; .$

X_{slot} is the input surface impedance of the slots, seen from the the waveguide.

We now consider the special case of the HE_{1N} mode - i.e. the mode whose azimuthal mode number $m = 1$ and whose γ-value is positive. To reduce mathematical complexity we further restrict the analysis to the case where γ is +1. The condition for this to be the case is examined in Section 2.4 below. Then from equation (2.1), putting $\gamma = +1$ and $m = 1$, and introducing the constant part $e^{im\phi}$ of the phase factor we have

$$E_z = J_1(k_c r) \; \mathrm{Cos} \; \phi \quad , \tag{2.5a}$$

$$H_z = \frac{1}{Z_o} J_1(k_c r) \; \mathrm{Sin} \; \phi \quad , \tag{2.5b}$$

$$E_r = - i \frac{k_o}{k_c} [\beta' J'_1(k_c r) + \frac{J_1(k_c r)}{k_c r}] \text{Cos } \phi \quad , \qquad (2.5c)$$

$$E_\phi = i \frac{k_o}{k_c} [\beta' \frac{J_1(k_c r)}{k_c r} + J'_1(k_c r)] \text{Sin } \phi \quad , \qquad (2.5d)$$

$$H_r = - i \frac{k_o}{Z_o k_c} [\beta' J'_1(k_c r) + \frac{J_1(k_c r)}{k_c r}] \text{Sin } \phi \quad , \qquad (2.5e)$$

$$H_\phi = - i \frac{k_o}{Z_o k_c} [\beta' \frac{J_1(k_c r)}{k_c r} + J'_1(k_c r)] \text{Sin } \phi \quad . \qquad (2.5f)$$

These can be more usefully expressed in rectangular coordinates:

$$E_x = - i \frac{k_o}{2 k_c} [(\beta'+1) J_o(k_c r) - (\beta'-1) J_2(k_c r) \text{ Cos } 2\phi] \quad , \qquad (2.6a)$$

$$E_y = - i \frac{k_o}{2 k_c} (-\beta'+1) J_2(k_c r) \text{ Sin } 2\phi \quad , \qquad (2.6b)$$

$$H_x = - i \frac{k_o}{Z_o 2 k_c} (-\beta'+1) J_2(k_c r) \text{ Sin } 2\phi \quad , \qquad (2.6c)$$

$$H_y = - i \frac{k_o}{Z_o 2 k_c} [(\beta'+1) J_o(k_c r) + (\beta'-1) J_2(k_c r) \text{ Cos } 2\phi] \quad . \qquad (2.6d)$$

If now β' is taken to be close to unity, as it will be in a corrugated guide whose reduced diameter is large (say $k_o a > 5$), then the $\underline{E}$ field of the HE_{1N} mode is

$$E_x(r) \propto J_o(k_c r) \quad , \quad E_y(r) = 0 \qquad r \leq a \qquad (2.7)$$

The boundary condition that there be no radial $\underline{E}$ field at r = a ensures that $k_c a$ for an HE_{1N} mode is equal to the N^{th} zero of the first order Bessel function. In particular for HE_{11}, $k_c a = 2.405$.

The HE_{11} mode is of special importance to us. First, it can be seen that in the xy cross-section it is plane-polarized (i.e. $E_y = 0$) at every point. Secondly, the modulus of the $\underline{E}$ in the cross-section depends only on distance from the axis, i.e. is axially symmetric.

(Note that we will have to examine the conditions in which γ is indeed + 1: see Section 2.4.)

2.3 Excitation of the HE_{11} mode

We must now consider how the HE_{11} mode in corrugated guide can be excited. Sources such as IMPATT's are conventionally mounted in rectangular waveguide. A transition is therefore required to convert a rectangular TE_{11} mode to a circular corrugated HE_{11} mode. This is done in two sections [2.1]. First the rectangular guide is conventionally tapered to circular guide. Secondly, this circular guide is juxtaposed directly with a corrugated transition section as shown in Fig. 2b. The guide dimensions are determined by the need for only the desired HE_{11} mode to propagate. The guide radius and slot depth are chosen to ensure that the guide is single moded over as wide a bandwidth as possible about the design centre frequency. (The conditions for the guide to be single moded are discussed in Appendix I.) The forward wave vector β in the corrugated section is also to be well-matched to that in the smooth circular section. It is worth noting that the HE_{11} mode is not balanced at this point, i.e. $\gamma \neq 1$.

Machining tolerances are most exacting in the transition section. Flaws in the form of the fins will make a horn highly attenuating and give it a poor antenna pattern. However, with care, the transition can be made to work well as will be seen when we present results of measurements on

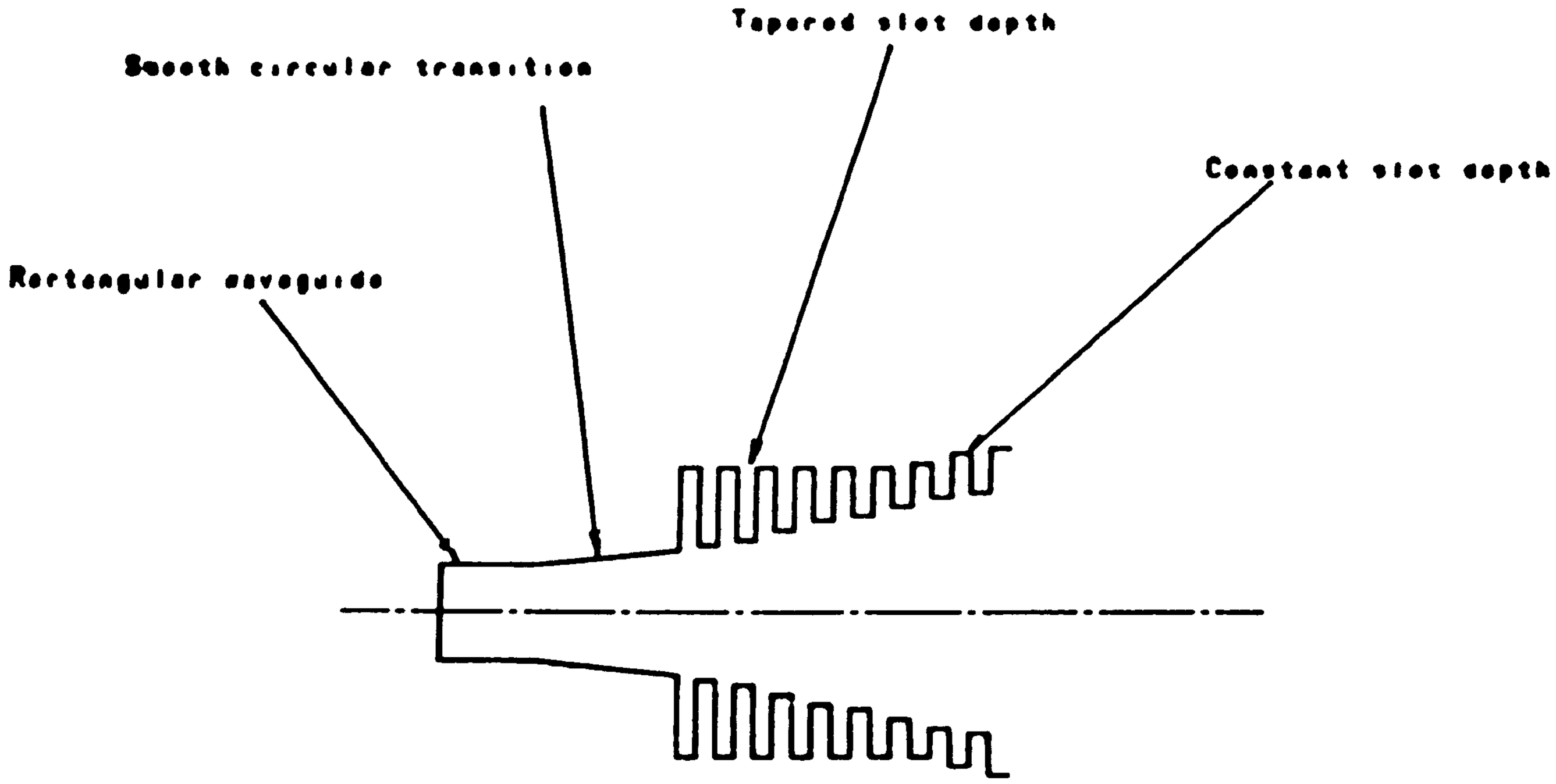

Fig. 2 b RECTANGULAR-TO-CORRUGATED WAVEGUIDE TRANSITION

horns using a null reflectomer in Chapter 6. They indicate that very little mismatch occurs in the transition.

2.4 Corrugated horn design

A desirable characteristic of conical horn antennas is that power radiated should be concentrated in an axially symmetrical beam. The antenna designer aims to achieve these characteristics over as wide a bandwidth as possible. The condition for a horn to generate an axially symmetrical beam is that the field on the aperture be axially symmetric. We have seen that this is the case for a corrugated horn excited with the HE_{11} mode when the guide dimensions are such that $\gamma = 1$. We now consider the design of a horn formed from tapered waveguide. Such horns have been treated by [2.1] and [2.2]. The guide is slowly tapered up from the transition and the slot depth reduced to a depth at which Z_{slot} is close to ∞, where $\gamma = +1$. A slow taper is used (5^{o} half-angle) to ensure that higher modes are not generated in the wider ports of the guide where they can propagate. Our objective here is to find the condition for γ to be close to unity over as wide a bandwidth as possible.

Recalling that

$$\gamma = - \frac{m \beta' J_m(k_c a)}{k_c a \; J'_m(k_c a)} \quad . \qquad (2.3 \text{ bis})$$

This equation for γ can be combined with the dispersion relation in equation 2.4 to give a value for γ in terms of the slot impedance:

$$m \beta' \left[\gamma - \frac{1}{\gamma} \right] = - \frac{[k_c a]^2}{k_o a} \left[\frac{Z_o}{X_{slot}} \right] \quad . \qquad (2.8)$$

When the reduced waveguide is large ($k_o a > 5$) the asymptotic expansion of X_{slot} is

$$\lim_{k_o a \to \infty} \frac{X_{slot}}{Z_o} - \tan k_o d \quad , \qquad (2.9)$$

where d = b − a, the depth of the slot.

For γ to equal unity the RHS of equation (2.8) must be vanishingly small. For large values of $k_o a$ we have shown that for the HE_{11} mode, $k_c a = 2.405$ if $\gamma = 1$. Taking this value of $k_c a$, a computer program was written to generate values of γ as a function of reduced frequency of corrugated waveguide. The reduced frequency is the frequency divided by the frequency for $Z_{slot} = \infty$. Fig. 2c shows results from these calculations for two values of $k_o a$ as a parameter.

The results are consistent with the use of the value 2.405 for $k_c a$. The large bandwidth observed in Fig. 2c ensure that horns with large apertures perform well over a wide frequency range. It also relaxes the machining tolerances required at the aperture. In practice the useful bandwidth is determined therefore not by the need to have γ close to 1 at the aperture, but by the range of frequency over which the transition will excite only the HE_{11} mode (see Appendix I).

Fig. 2d gives details of the complete horn antenna provided by considerations set out in this and the preceding section.

2.5 Gaussian beam-mode analysis of the operation of corrugated horns.

This thesis is based on the view that paraxial propagation is best analysed using Gaussian beam-modes. We therefore now proceed to apply Gaussian beam-mode theory, reviewed in Chapter 1, to the analysis of radiation from the aperture of corrugated horns. A surprising result from the analysis is that almost 98% of the power radiated from corrugated horns lies in the fundamental Gaussian beam-mode.

Consider a conical corrugated horn placed along the Z axis of a Cartesian co-ordinate system so that the aperture of the horn lies in the X Y plane. Suppose the horn is excited with an X axis polarized HE_{11} mode,

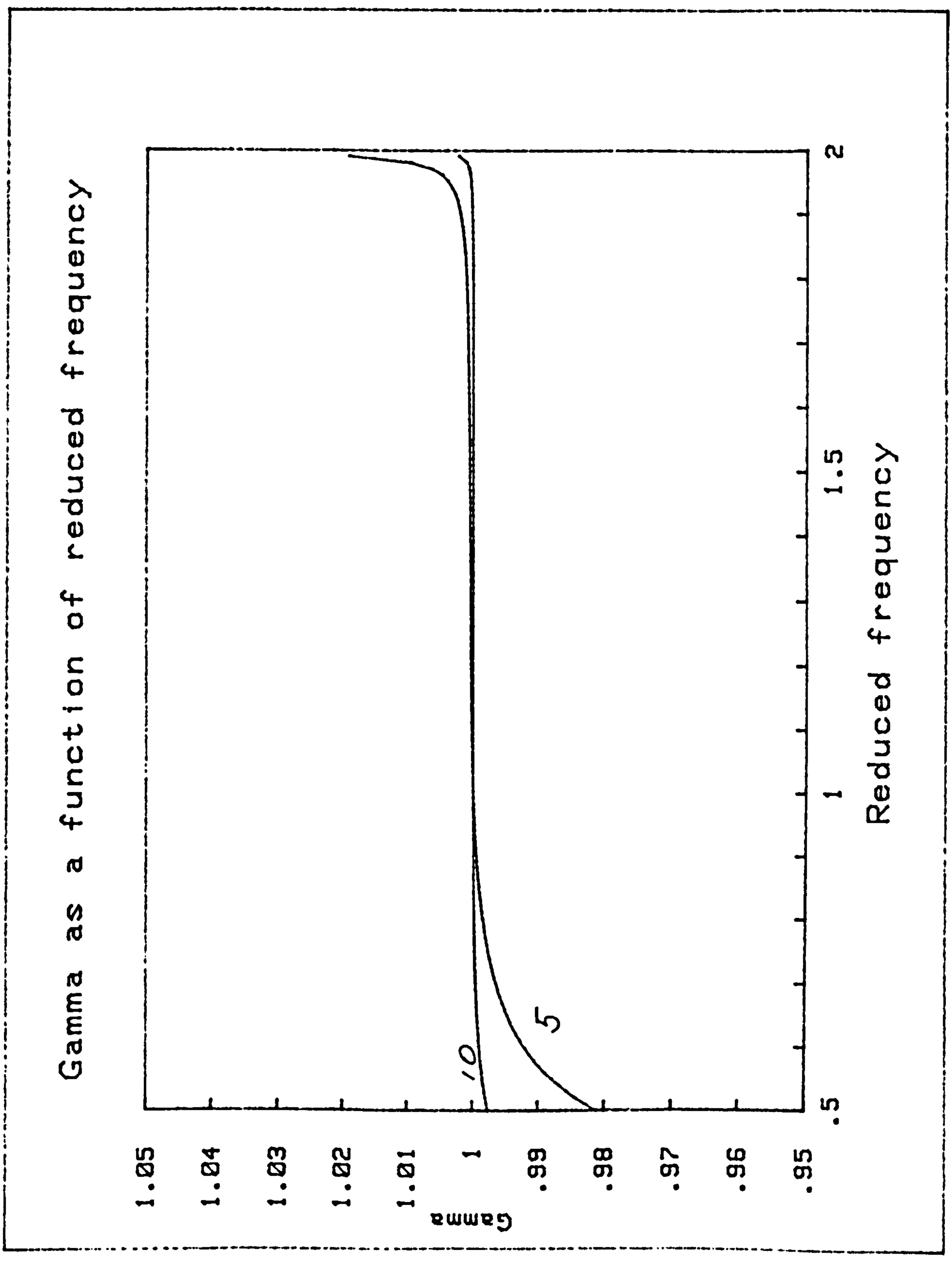
Gamma as a function of reduced frequency
Gamma
1.05
1.04
1.03
1.02
1.01
1
.99
.98
.97
.96
.95
10
5
.5
1
1.5
2
Reduced frequency

Fig. 2c

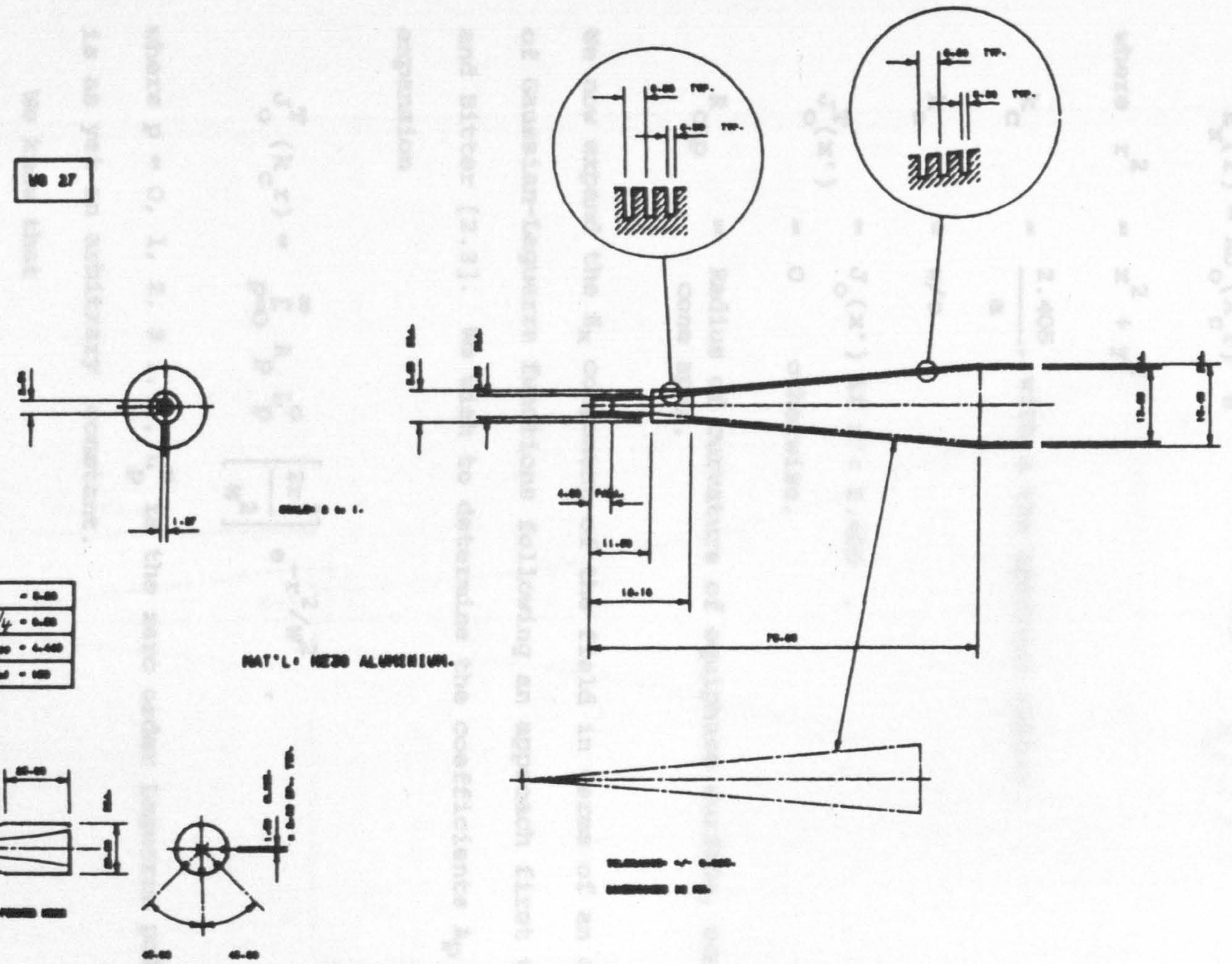

COMPUTER AIDED DRAUGHTING. THIRD ANGLE PROJECTION.	THOMAS KEATING LTD.					TK	SCALAR HORN

under balanced hybrid conditions [2.1], [2.2]. Using the results of section 2.2 (Equations 2.7), but adding a phase term to allow for the curvature of the phase front of the conical waveguide section, the time independent factor of the E field in the aperture is (see Fig. 2e)

$$E_x(r) = A J_o^T(k_c r)\ e^{-i\, k_o r^2/(2\, R_{cap})}\ ,\ E_y(r) = 0\ , \qquad (2.10)$$

where $r^2 = x^2 + y^2$,

$k_c = \frac{2.405}{a}$, with a the aperture radius ,

$k_o = w/c$

$J_o^T(x') = J_o(x')$ if $x' < 2.405$,

$= 0$ otherwise,

R_{cap} = Radius of curvature of equiphase surface, centred at the cone apex.

We now expand the E_x component of the field in terms of an orthogonal set of Gaussian-Laguerre functions following an approach first taken by Aubry and Bitter [2.3]. We wish to determine the coefficients A_p in the expansion

$$J_o^T(k_c r) = \sum_{p=0}^{\infty} A_p\, L_p^o \left[\frac{2r^2}{w^2}\right] e^{-r^2/w^2}\ , \qquad (2.11)$$

where p = 0, 1, 2, 3 ...., L_p^o is the zero order Laguerre polynomial and W is as yet an arbitrary constant.

We know that

$$\int_o^{\infty} L_N^o \left[\frac{2r^2}{w^2}\right] L_M^o \left[\frac{2r^2}{w^2}\right] e^{-2r^2/w^2}\, 2\pi r dr = \frac{2\pi w^2}{4}\, \delta_{NM}\ . \qquad (2.12)$$

Thus multiplying equation (2.11) by $L_N^o \left[\frac{2r^2}{w^2}\right] e^{-r^2/w^2}\, 2\pi r$

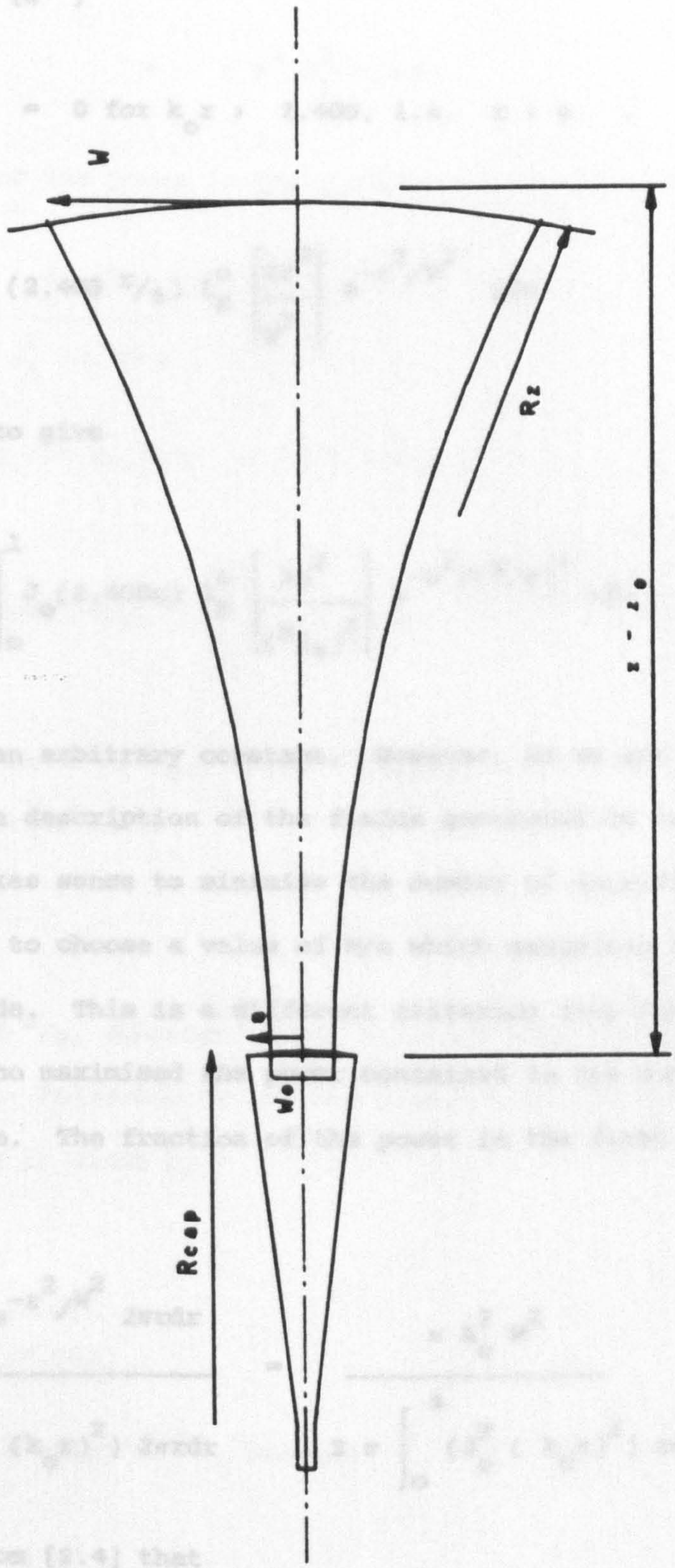

Fig. 2 e

and integrating with respect to r gives

$$\int_0^\infty J_o^T(k_c r)\, L_N^o\left[\frac{2r^2}{w^2}\right] e^{-r^2/w^2}\, 2\pi r dr = \frac{A_N \pi w^2}{2} \quad , \qquad (2.13)$$

so since $J_o^T(k_o r) = 0$ for $k_o r > 2.405$, i.e. $r > a$,

$$A_N = \frac{4}{w^2} \int_0^a J_o(2.405\, r/a)\, L_N^o\left[\frac{2r^2}{w^2}\right] e^{-r^2/w^2}\, r dr \quad . \qquad (2.14)$$

Substitute r = au to give

$$A_N = \frac{4}{(w/a)^2} \int_0^1 J_o(2.405u)\, L_N^o\left[\frac{2u^2}{(w/a)^2}\right] e^{-u^2/(w/a)^2}\, u du \quad . \qquad (2.15)$$

W/a is still an arbitrary constant. However, as we are interested in finding as simple a description of the fields generated by corrugated horns as possible, it makes sense to minimise the number of significant modes. This idea leads us to choose a value of W/a which maximises the power in the fundamental mode. This is a different criterion from that used by Aubry and Bitter who maximised the power contained in the sum of the modes under consideration. The fraction of the power in the first mode is given by:

$$\eta_o = \frac{\int_0^\infty A_o^2\, e^{-r^2/w^2}\, 2\pi r dr}{\int_0^a (J_o^T(k_c r)^2)\, 2\pi r dr} = \frac{\pi A_o^2 w^2}{2\pi \int_0^a (J_o^T(k_c r)^2)\, r dr} \quad . \qquad (2.16)$$

However we know from [2.4] that

$$\int_0^x J_m^2(kx)\, x\, dx = \frac{x^2}{2} J_{m+1}^2(kx) \quad , \qquad (2.17)$$

so

$$2\pi \int_0^a (J_o^T(k_c r))^2 \, r dr = \pi a^2 J_1^2 (k_c a)$$

$$= \pi a^2 J_1^2(2.405) \quad . \qquad (2.18)$$

Thus the fraction of the power in the fundamental mode is given by

$$\eta_o = \frac{A_o^2 W^2}{J_1^2 (2.405)} \quad , \qquad (2.19)$$

whence substituting for A_o from (2.15), since $L_o^o = 1$

$$\eta_o(W/a) = 5.9292 (a/W)^2 \left[\int_0^1 J_o (2.405u) \, e^{-u^2/(W/a)^2} \, u du \right]^2 . \qquad (2.20)$$

The maximum value of $\eta(W/a)$, when $\partial\eta/\partial(W/a) = 0$, is found by numerical approximation to be

$$\frac{W}{a} = 0.6435 \, . \qquad (2.21)$$

Using this value of W/a, equation (2.15) then generates the amplitude A_p given in Fig. 2f.i. Following (2.19) the fraction of the total power in the higher modes is given by

$$\eta_p = \frac{A_p^2 W^2}{a^2 J_1^2(2.405)} \quad , \qquad (2.22)$$

which with the above value of W/a becomes

$$\eta_p = 0.76726 \, A_p^2 \quad .$$

The values calculated from Fig. 2f.i using this relation are given in Fig. 2f.ii. The coefficients in Fig. 2f are the same for all

i		ii	
A_0	= 1.12972	P_0	= 0.9792
A_1	= - 0.00008	P_1	= 4.90×10^{-9}
A_2	= - 0.13757	P_2	= 1.45×10^{-2}
A_3	= - 0.04923	P_3	= 1.86×10^{-3}
A_4	= 0.02228	P_4	= 3.81×10^{-4}
A_5	= 0.03887	P_5	= 1.16×10^{-3}
A_6	= 0.02276	P_6	= 3.97×10^{-4}
A_7	= 0.00014	P_7	= 1.50×10^{-8}
A_8	= - 0.01437	P_8	= 2.33×10^{-4}
A_9	= - 0.01742	P_9	= 2.33×10^{-4}
A_{10}	= - 0.01209	P_{10}	= 1.12×10^{-4}

Figure 2f : Unnormalised amplitude, and normalised power coefficients for the Gaussian-Laguerre beam-mode expansion of the field at corrugated feed horns.

narrow flare-angle corrugated horns operating under balanced hybrid conditions regardless of dimensions.

We can now make use of propagating Gaussian beam-modes, which have been shown in chapter 1 to be solutions to the scalar wave equation, to derive the field propagating from, or received by, a horn. The propagation of each mode from the aperture of the horn to the far field is calculated. The magnitude of each mode is given by the Gaussian-Laguerre expansion of the field in the aperture. The contributions from each mode are then summed at the point of interest.

First the values of the beam parameters R, W, ϕ_p are determined at the cap of the horn. Equation (2.21) is used to give the beam size from the aperture size. The curvature R_{cap} is determined directly from the aperture size and length extended cone. Values of ϕ_{po} at $z = z_o$ are chosen to ensure that there is no phase slippage between the modes at the cap ($z = z_1$). Thus, at $z = z_1$,

$$w_1^2 = (0.6435)^2 a^2 , \tag{2.23}$$

$$R_1 = R_{cap} , \tag{2.24}$$

$$\phi_{p1} = 0 , \tag{2.25}$$

Then, using (1.8)

$$z_1 = \frac{k_o w_1^2}{2 R_1} = \frac{k_o (0.6435)^2 a^2}{2 R_{cap}} . \tag{2.26}$$

Let us introduce a parameter

$$M \equiv \frac{k_o a^2}{2 R_{cap}} , \tag{2.27}$$

which is equal to the total phase change over the aperture plane, between the axis and r = a. Then (2.25) becomes

$$\ddot{z}_1 = (0.6435)^2 M \quad . \tag{2.28}$$

Second, these values are used to find the beam parameters at the imaginary beam-waist inside the throat of the horn, where, by definition, $W = W_o$ and $z = z_o$. Using (1.5), (1.4),(1.6) and (1.7), and remembering that the phase slippage ϕ_p has been chosen to be zero on the cap,

$$W_o^2 = \frac{W_1^2}{1 + \ddot{z}_1^2} \tag{2.29}$$

$$= \frac{(0.6435)^2 a^2}{1+(0.6435)^4 M^2} \tag{2.30}$$

$$R_o = \infty \quad , \tag{2.31}$$

$$\phi_p = -(2p+1) \tan^{-1} \ddot{z}_1 \quad , \tag{2.32}$$

$$= -(2p+1) \tan^{-1} (0.6435)^2 M \quad , \tag{2.33}$$

$$\ddot{z}_o = 0 \quad . \tag{2.34}$$

Third, these values are used to deduce the beam parameters at the near or far-field position required, say z_2 :

$$W_2^2 = W_o^2[1+ \ddot{z}_2^2] \tag{2.35}$$

$$= \frac{(0.6435)^2 a^2}{(1+(0.6435)^4 M^2)} [1 + \bar{z}_2^2] \quad , \tag{2.36}$$

$$R_2 = (z_2 - z_o) \left[1 + \frac{1}{\bar{z}_2^2}\right] \quad , \tag{2.37}$$

$$\Phi_{p2} = (2p + 1) \left[\tan^{-1} \bar{z}_2 - \tan^{-1} (0.6435)^2 M\right] \quad . \tag{2.38}$$

The field $\psi(r,z_2)$ is then derived by substituting these beam parameters for z_2 into equation (1.2). The phase term in $\psi(r,z_2)$ associated with the phase front curvature, and the $e^{ik_o z}$ term are common to all modes; they do not contribute to $\psi(r,z_2)\ \psi^*(r,z_2)$ and they have therefore been omitted from the equations for $\psi(r,z_2)$ below.

To illustrate the use of Gaussian beam-mode analysis, the far-field antenna pattern is now derived. In the far-field:

$$\bar{z}_2 \to \infty \quad , \tag{2.39}$$

$$W_2^2 \to W_o^2 \bar{z}_2^2 \tag{2.40}$$

$$= \frac{4}{k_o^2} \frac{(z_2 - z_o)^2}{\left[\frac{(0.6435)^2 a^2}{1+(0.6435)^4 M^2}\right]} \quad , \tag{2.41}$$

$$R_2 \to (z_2 - z_o) \quad , \tag{2.42}$$

and

$$\Phi_{p2} \to (2p+1) \left[\pi/_2 - \tan^{-1} (0.6435)^2 M\right] \quad . \tag{2.43}$$

Let θ be the angle of boresight, i.e.

$$\tan\theta = \frac{r}{z_2 - z_o}, \tag{2.44}$$

and F be the far-field distance. Then substituting (2.41), (2.42), (2.43) and (2.44) into equation (1.2) gives

$$\psi(\theta) = \sum_{p=o}^{\infty} A_p \left[\frac{k_o^2 a^2}{2\pi F^2 \cos^2\theta \frac{(1+(0.6435)^4 M^2)}{(0.6435)^2}}\right]^{1/2} L_p^o\left[\frac{k_o^2 a^2 \tan^2\theta}{\frac{2(1+(0.6435)^4 M^2)}{(0.6435)^2}}\right]$$

$$\exp-\left[\frac{k_o^2 a^2 \tan^2\theta}{\frac{4(1+(0.6435)^4 M^2)}{(0.6435)^2}}\right] \exp i(2p+1)\left[\pi/2 - \tan^{-1}(0.6435)^2 M\right]. \tag{2.45}$$

Normalised far-field antenna patterns for narrow-flare angle horns, evaluated using the Gaussian-Laguerre expansion are plotted in Figs. 2g and 2h. In both cases the parameter is $M/2\pi$. Fig. 2g gives the pattern for horns with a small phase change over the aperture ($M/2\pi \leq 0.4$) as a function of $k_o a \sin\theta$. The patterns of these horns are sensitive to frequency changes.

Fig. 2h gives the pattern for horns with a large phase change over the aperture as a function of θ/θ_o where θ_o is the half flare angle of the horn. The pattern of these horns is frequency insensitive.

It is instructive to compare the plots with similar plots made by Thomas [2.5], Figs. 2 and 6. The plots are almost indistinguishable. (Note that the parameter $M/2\pi$ is that denoted Δ by Thomas.)

It should be stressed that the method of analysis can be applied to calculating antenna patterns in the near field as well. For example,

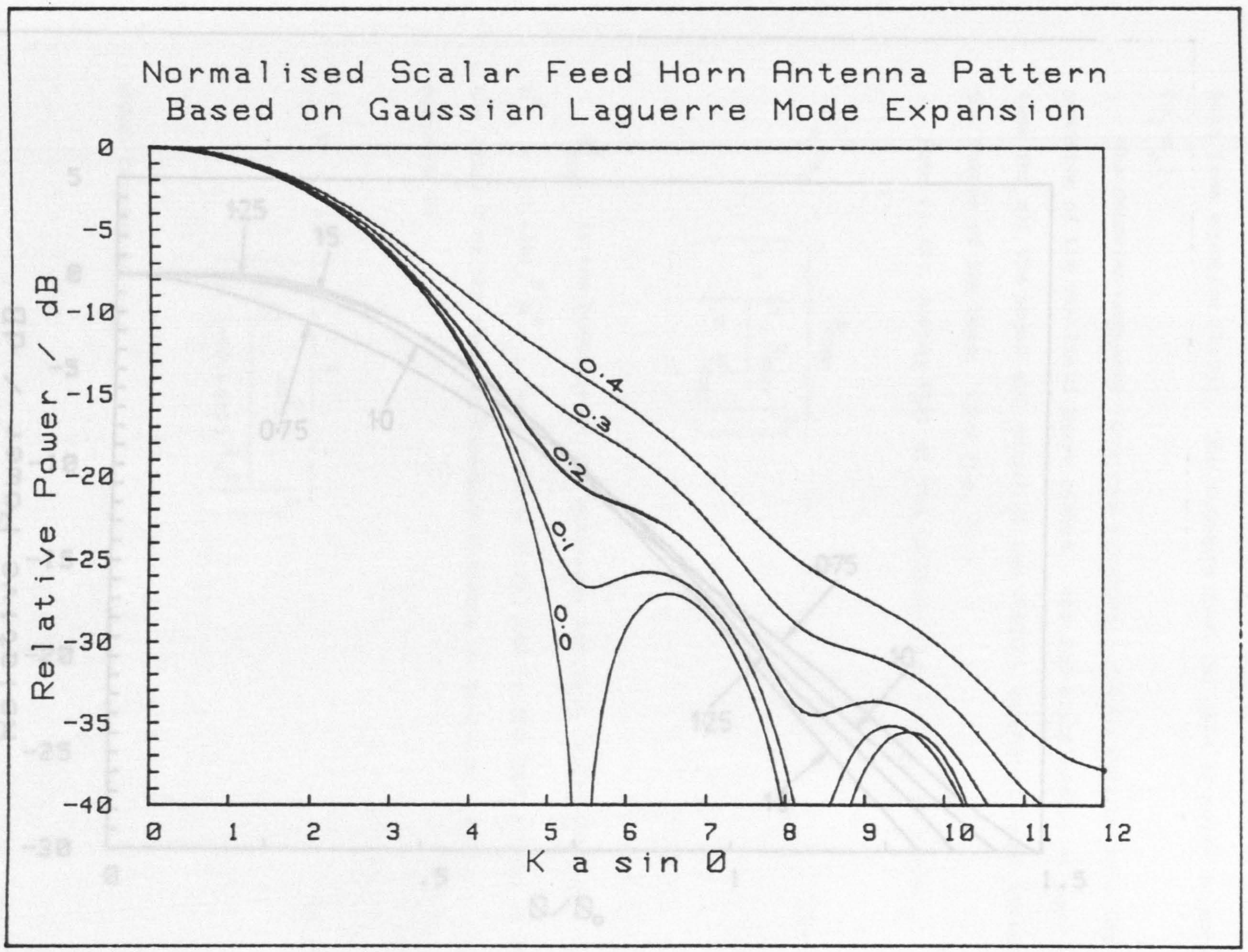
Normalised Scalar Feed Horn Antenna Pattern
Based on Gaussian Laguerre Mode Expansion
Relative Power / dB
0
-5
-10
-15
-20
-25
-30
-35
-40
0.4
0.3
0.2
0.1
0.0
0
1
2
3
4
5
6
7
8
9
10
11
12
K a sin Ø

Fig. 2g

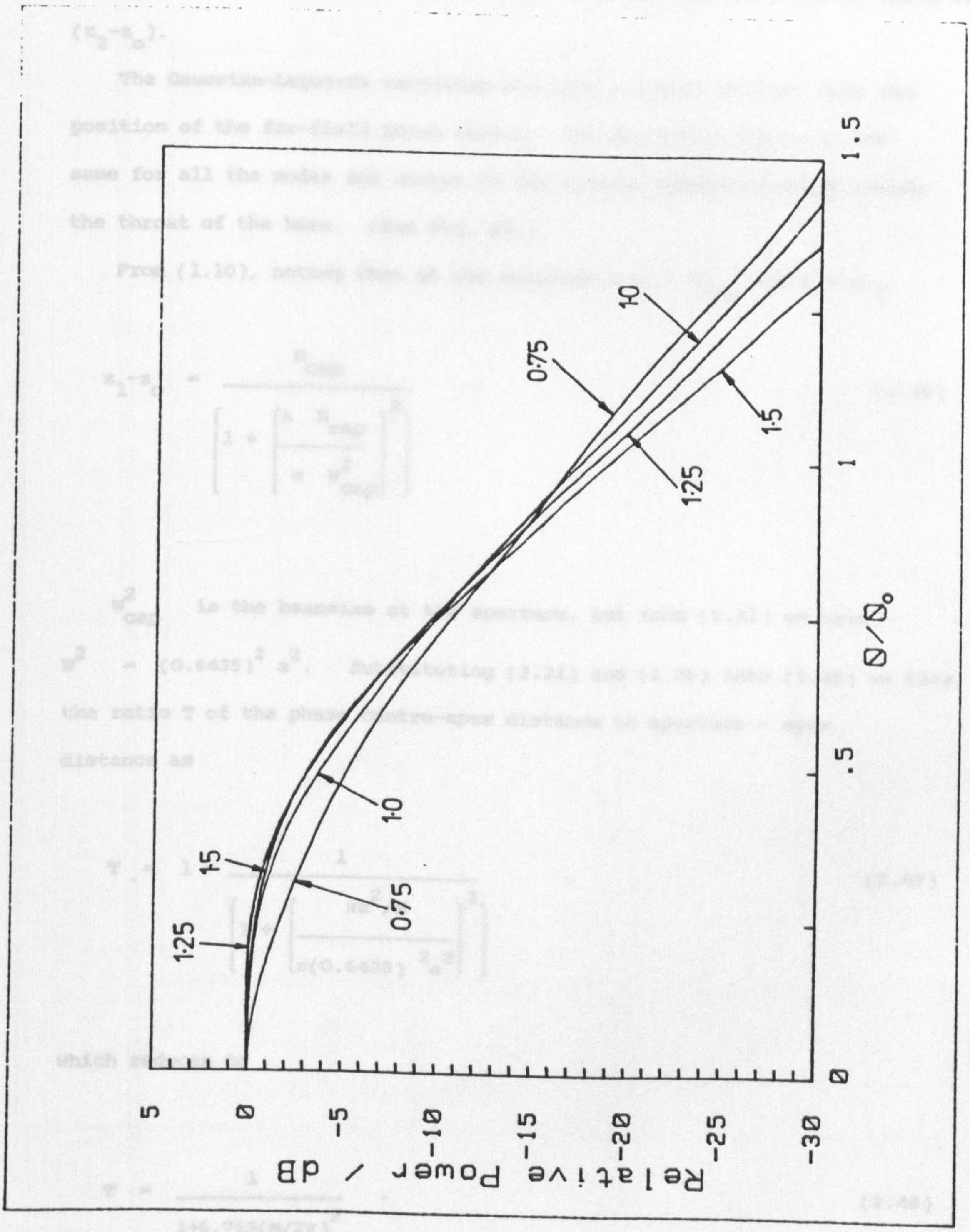
Relative Power / dB
5
0
-5
-10
-15
-20
-25
-30
0
.5
1
1.5
θ/θ₀
1·0
0·75
1·5
1·25
1·5
1·25
1·0
0·75

Fig. 2h

Fig. 2.i shows a pattern a horn for which $k_o a = 10$ and $M/2\pi = 0.1$. The plane of interest is taken at $\bar{z} = 1$ from the virtual beam waist inside the horn (see equation (1.7)). The distance from the axis is given in units of $(z_2 - z_o)$.

The Gaussian-Laguerre technique provides a simple insight into the position of the far-field phase centre. The far-field centre is the same for all the modes and occurs at the virtual beamwaist found inside the throat of the horn. (See Fig. 2d.)

From (1.10), noting that at the aperture $R(z) = R_{cap}$ and $z = z_{1'}$

$$z_1 - z_o = \frac{R_{cap}}{\left[1 + \left[\frac{\lambda \; R_{cap}}{\pi \; W_{cap}^2}\right]^2\right]} \quad . \tag{2.46}$$

W_{cap}^2 is the beamsize at the aperture, but from (2.21) we have $W^2 = (0.6435)^2 a^2$. Substituting (2.21) and (2.26) into (2.46) we have the ratio T of the phase centre-apex distance to aperture - apex distance as

$$T = 1 - \frac{1}{\left[1 + \left[\frac{\pi a^2/M}{\pi (0.6435)^2 a^2}\right]^2\right]} \quad , \tag{2.47}$$

which reduces to

$$T = \frac{1}{1+6.769(M/2\pi)^2} \quad . \tag{2.48}$$

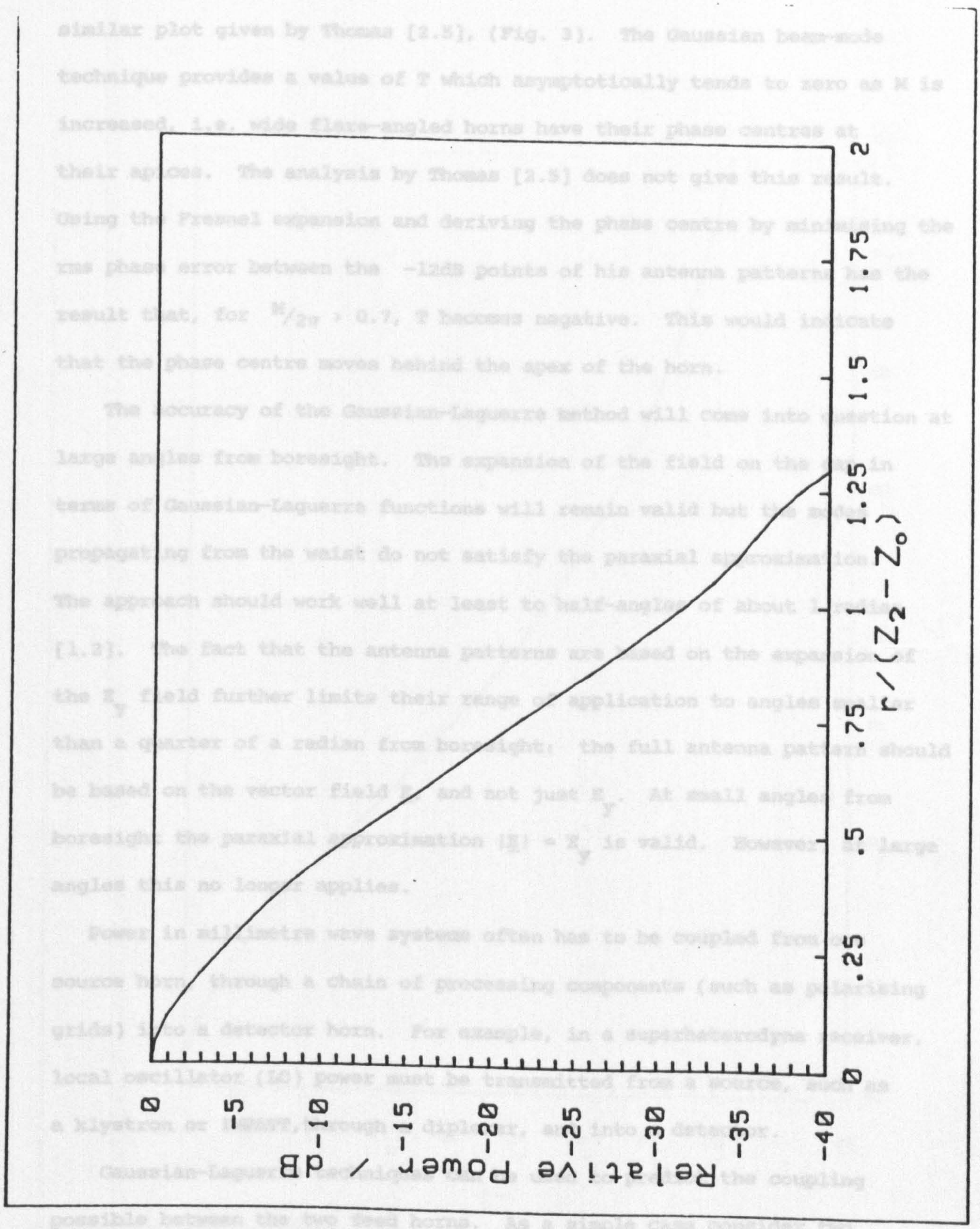
Relative Power / dB
0
-5
-10
-15
-20
-25
-30
-35
-40
0
.25
.5
.75
1
1.25
1.5
1.75
2
r/(Z2 - Z0)

Fig. 2i

This function is plotted in Fig. 2j and can be compared with a similar plot given by Thomas [2.5], (Fig. 3). The Gaussian beam-mode technique provides a value of T which asymptotically tends to zero as M is increased, i.e. wide flare-angled horns have their phase centres at their apices. The analysis by Thomas [2.5] does not give this result. Using the Fresnel expansion and deriving the phase centre by minimising the rms phase error between the -12dB points of his antenna patterns has the result that, for $M/2\pi > 0.7$, T becomes negative. This would indicate that the phase centre moves behind the apex of the horn.

The accuracy of the Gaussian-Laguerre method will come into question at large angles from boresight. The expansion of the field on the cap in terms of Gaussian-Laguerre functions will remain valid but the modes propagating from the waist do not satisfy the paraxial approximation. The approach should work well at least to half-angles of about 1 radian [1.2]. The fact that the antenna patterns are based on the expansion of the E_y field further limits their range of application to angles smaller than a quarter of a radian from boresight: the full antenna pattern should be based on the vector field $\underline{E}$, and not just E_y. At small angles from boresight the paraxial approximation $|\underline{E}| = E_y$ is valid. However, at large angles this no longer applies.

Power in millimetre wave systems often has to be coupled from one source horn, through a chain of processing components (such as polarising grids) into a detector horn. For example, in a superheterodyne receiver, local oscillator (LO) power must be transmitted from a source, such as a klystron or IMPATT,through a diplexer, and into a detector.

Gaussian-Laguerre techniques can be used to predict the coupling possible between the two feed horns. As a simple case consider two identical horns. Let them lie on the z axis (Fig. 2k). It is well known that the coupling between two antennas is given by the integral of the product of the normalised $\underline{E}$ field antenna pattern of one, and the complex

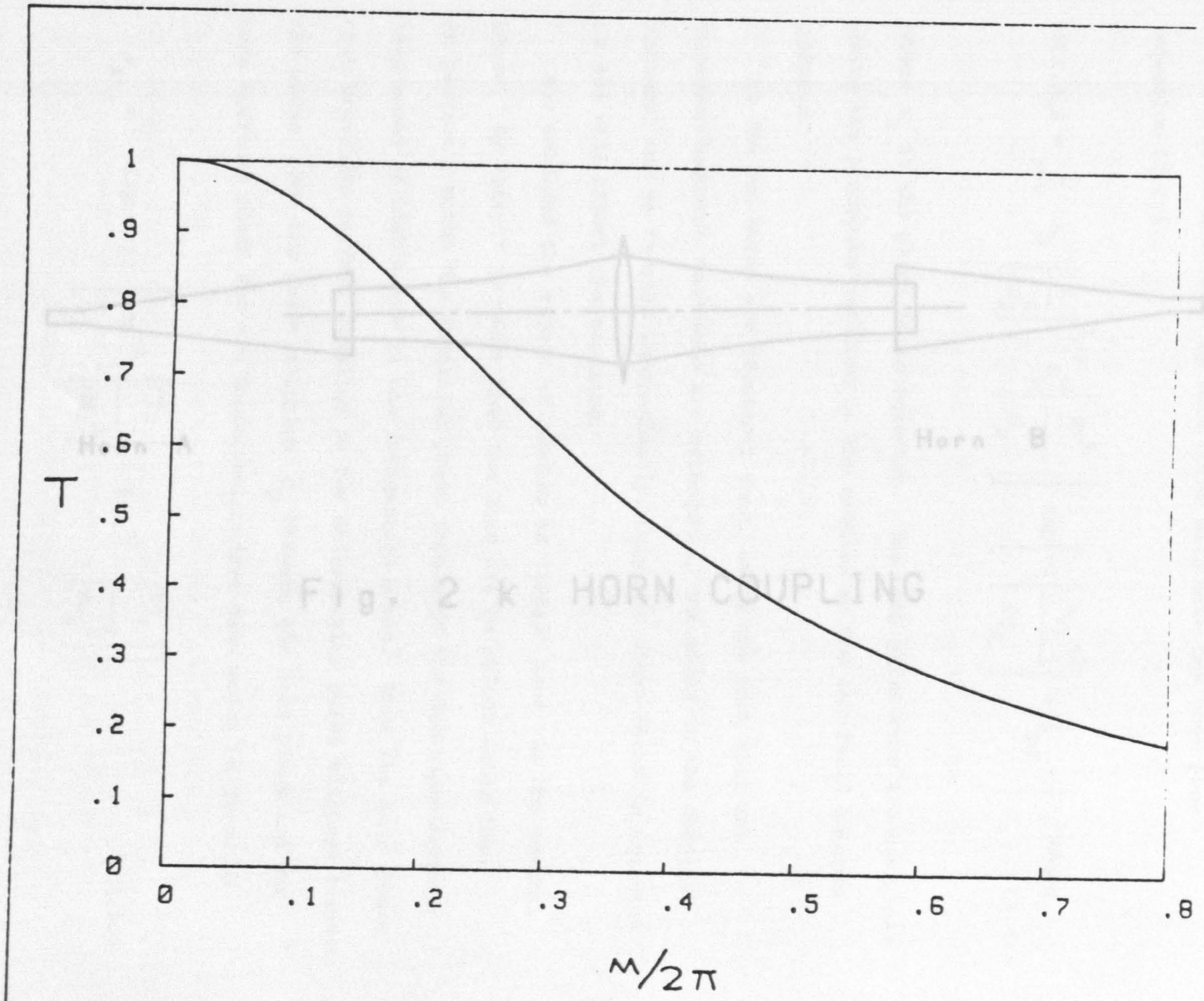

Fig. 2j

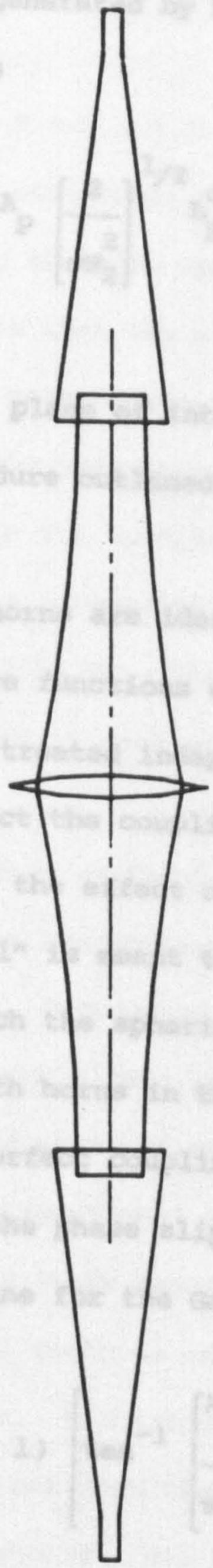

Fig. 2 K HORN COUPLING

conjugate of the normalised $\underline{E}$ field antenna pattern of the other, over any surface between them. For simplicity, we choose to integrate over the plane perpendicular to the z axis and equidistant from both horns.

The field generated by both horns will have the form (see equation (1.2))

$$\psi(r,z_2) = \sum_{p=0}^{\infty} A_p \left[\frac{2}{\pi W_2^2}\right]^{1/2} L_p^o\left[\frac{2r^2}{W_2^2}\right] \exp\left\{-i\left[\frac{k_o r^2}{2q_2}\right] + \phi_{p2}\right\} e^{-ik_o z_2} \quad , \qquad (2.49)$$

where z_2 is the plane of integration. The beam parameters are evaluated using the procedure outlined in the section on the far-field antenna pattern.

As the two horns are identical then, using the fact that the Gaussian-Laguerre functions are orthogonal, the modes in the coupling integral can be treated independently. Only the phase terms in equation (2.49) will affect the coupling.

Now consider the effect of placing an "ideal" lens in the central plane. By "ideal" is meant that the lens has no effect other than to perfectly match the spherical phase fronts of the Gaussian-Laguerre beam modes of both horns in the integration plane. Thus the only factor that precludes perfect coupling is the differential phase slippage between the modes. Now the phase slippage ϕ_p between the lens plane and the horn aperture plane for the Gaussian-Laguerre beam modes is given by

$$\phi_p = (2p + 1)\left[\tan^{-1}\left[\frac{\lambda z_2}{\pi W_o^2}\right] - \tan^{-1}\left[\frac{\lambda z_o}{\pi W_o^2}\right]\right] \quad , \qquad (2.50)$$

where p is the mode number.

Thus the fraction of power coupled from one horn to the other is given by

$$\frac{\left[\sum_{N=0}^{\infty} A_N A_N^* e^{i2\phi_N(z_2)} \sum_{M=0}^{\infty} A_M A_M^* e^{-i2\phi_M(z_2)}\right]^{1/2}}{\sum_{K=0}^{\infty} A_K A_K^*} \quad , \qquad (2.51)$$

where N,M and K = 0,1,2,3.....

The maximum efficiency is plotted against fundamental mode phase slippage between the horn aperture and the lens (Fig. 21). Perfect efficiency occurs when the slippage between the horn aperture and lens for the fundamental mode equals 0 or $\pi/2$. A slippage of zero occurs if the two horns are directly juxtaposed. A slippage of $\pi/2$ occurs only in the far-field and only in the special case that the horn has no phase change across the cap (a "waveguide" horn). The coupling losses are not serious, at maximum only 0.15 dB. This is in most cases insignificant compared with losses caused in real systems by beam truncation and non-ideal lenses.

2.6 The manufacture of Corrugated Horns

A design for the internal form of a waveguide fed corrugated horn is shown in Fig. 2d. Corrugated horns for frequencies in the microwave region have previously been manufactured [2.6]. At microwave wavelengths the slot depth and aperture size of corrugated horns are large enough to allow conventional machining methods, such as milling and turning, to be used in their manufacture. However, horn dimensions scale directly with wavelength as one moves from the microwave region into the mm-wave region. Mechanical rigidity and breaking stress of horns, and the mandrels that form them, therefore reduce as the wavelength of operation is reduced. For wavelength below 3 mm, the slot depths required are less than 500 μm.

From detailed practical experience of the techniques used for the manufacture of injection moulds and press-tools gained in another

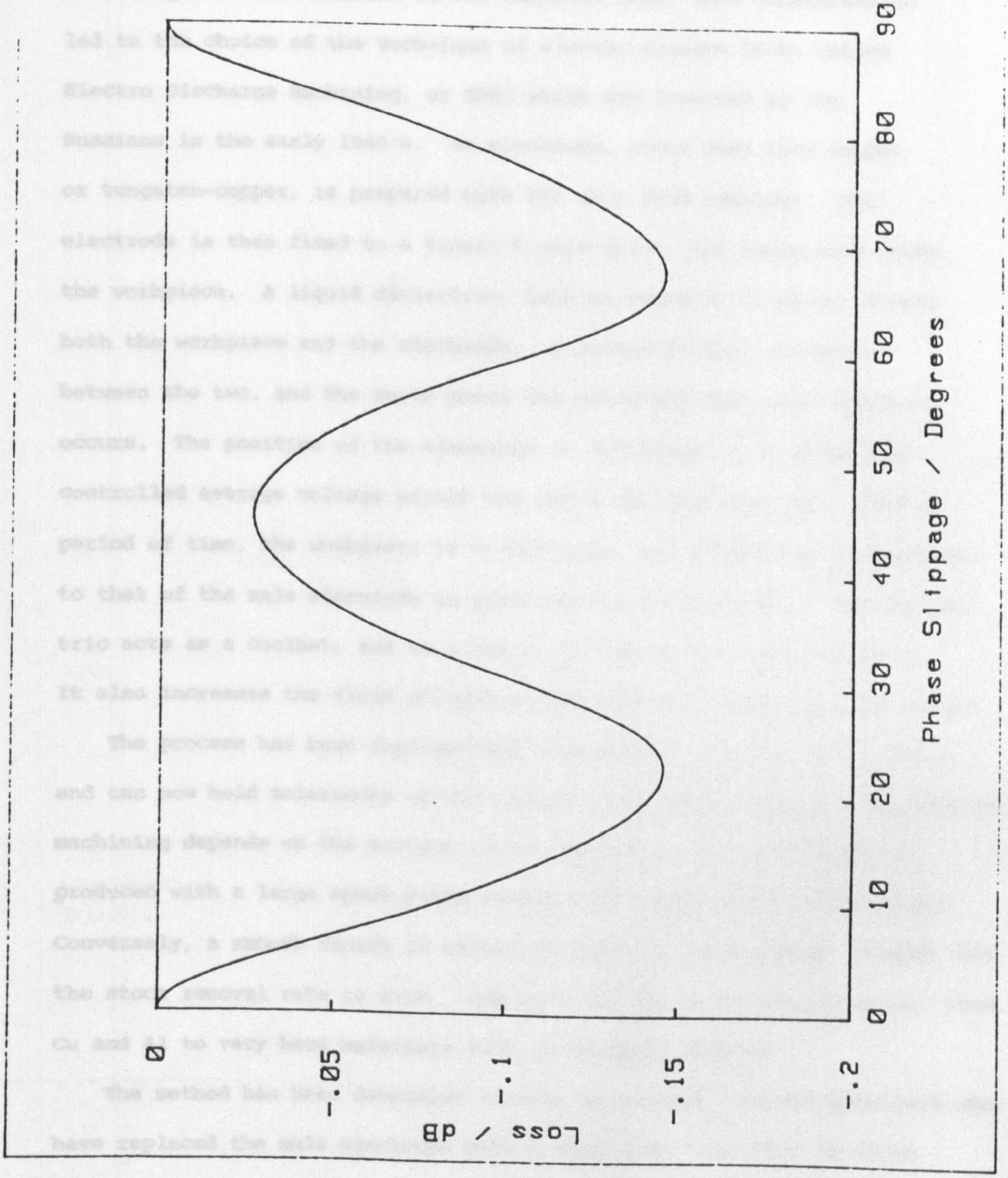
Loss / dB
0
-.05
-.1
-.15
-.2
Phase Slippage / Degrees
0
10
20
30
40
50
60
70
80
90

Fig. 21

connection it was clear to us that only machining methods that do not put mechanical stress on the workpiece could be used for the manufacture of corrugated horn mandrels of the required size. This consideration led to the choice of the technique of electro-erosion (also called Electro Discharge Machining, or EDM) which was invented by the Russians in the early 1940's. An electrode, often made from copper or tungsten-copper, is prepared with the male form required. The electrode is then fixed to a linear Z axis servo, and positioned above the workpiece. A liquid dielectric, such as paraffin or water, covers both the workpiece and the electrode. A pulsed voltage is applied between the two, and the servo moves the electrode down until sparking occurs. The position of the electrode is determined by a servo loop controlled average voltage across the spark gap (see Fig. 2m). Over a period of time, the workpiece is eroded away, and a female form opposite to that of the male electrode is generated in the workpiece. The dielectric acts as a coolant, and as a medium to remove the eroded material. It also increases the field allowed across the gap before sparking occurs.

The process has been improved and refined over the last forty years, and can now hold tolerances of five microns in complex shapes. The rate of machining depends on the surface finish required. A rough finish is produced with a large spark pulse energy, and a high stock removal rate. Conversely, a smooth finish is generated when low pulse energy is used, but the stock removal rate is slow. EDM will cut any conducting material, from Cu and Al to very hard materials such as Tungsten Carbide.

The method has been developed further by machine tool manufacturers who have replaced the male electrode with a thin wire. The wire is moved continuously in the Z axis and mechanical and electrical pulsed tension applied to it. Deionised water, acting as the dielectric is pumped over the wire. The wire passes through the workpiece which is moved in the X Y plane under numerical control with a resolution of 1 μ. The path that the

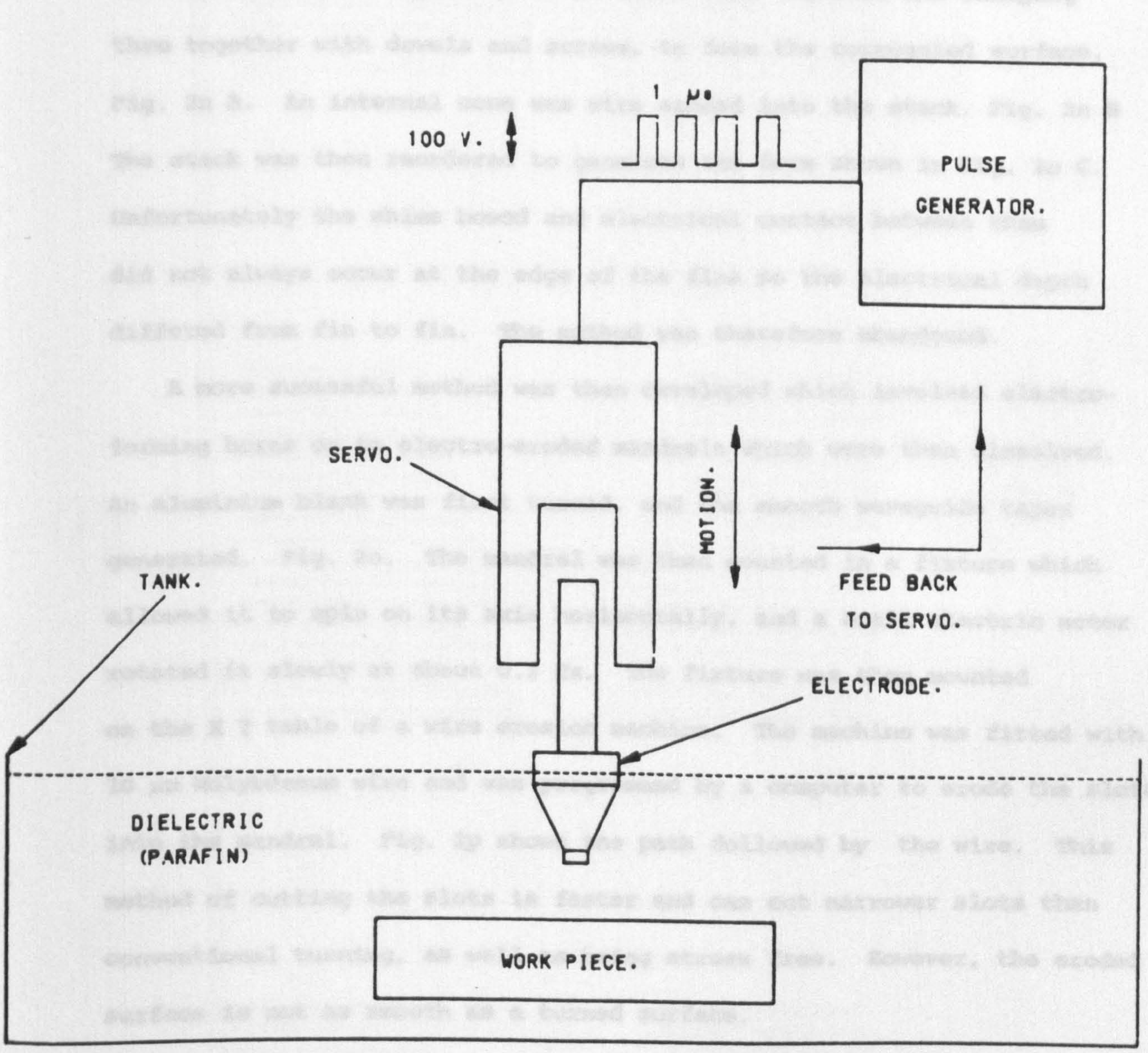

Fig. 2 m ELECTRO-EROSION

table follows is programmed by a computer and fed in via paper tape to the machine's Numerical Control Unit. The machine therefore acts as a computer-controlled metal-cutting fret saw.

Fortunately the EDM facilities at Thomas Keating Ltd. were available for trials. The first attempt to manufacture corrugated horns involved the sandwiching of layers of 25 μm steel shim together and clamping them together with dowels and screws, to form the corrugated surface. Fig. 2n A. An internal cone was wire eroded into the stack. Fig. 2n B The stack was then reordered to generate the form shown in Fig. 2n C. Unfortunately the shims bowed and electrical contact between them did not always occur at the edge of the fins so the electrical depth differed from fin to fin. The method was therefore abandoned.

A more sucessful method was then developed which involved electro-forming horns on to electro-eroded mandrels which were then dissolved. An aluminium blank was first turned, and the smooth waveguide taper generated. Fig. 2o. The mandrel was then mounted in a fixture which allowed it to spin on its axis horizontally, and a small electric motor rotated it slowly at about 0.3 Hz. The fixture was then mounted on the X Y table of a wire erosion machine. The machine was fitted with 10 μm Molybdenum wire and was programmed by a computer to erode the slots into the mandrel. Fig. 2p shows the path followed by the wire. This method of cutting the slots is faster and can cut narrower slots than conventional turning, as well as being stress free. However, the eroded surface is not as smooth as a turned surface.

Electroforming [2.7] involves the slow electrical deposition of a metal such as copper or nickel, on to a conducting mandrel held in a bath of electrolyte. If the form of the mandrel is not blind, as in the case of a smooth horn, the mandrel can be made of stainless steel and can be removed from the grown form by pulling. However, corrugated horn mandrels have blind forms. They must therefore be made of a material that can be

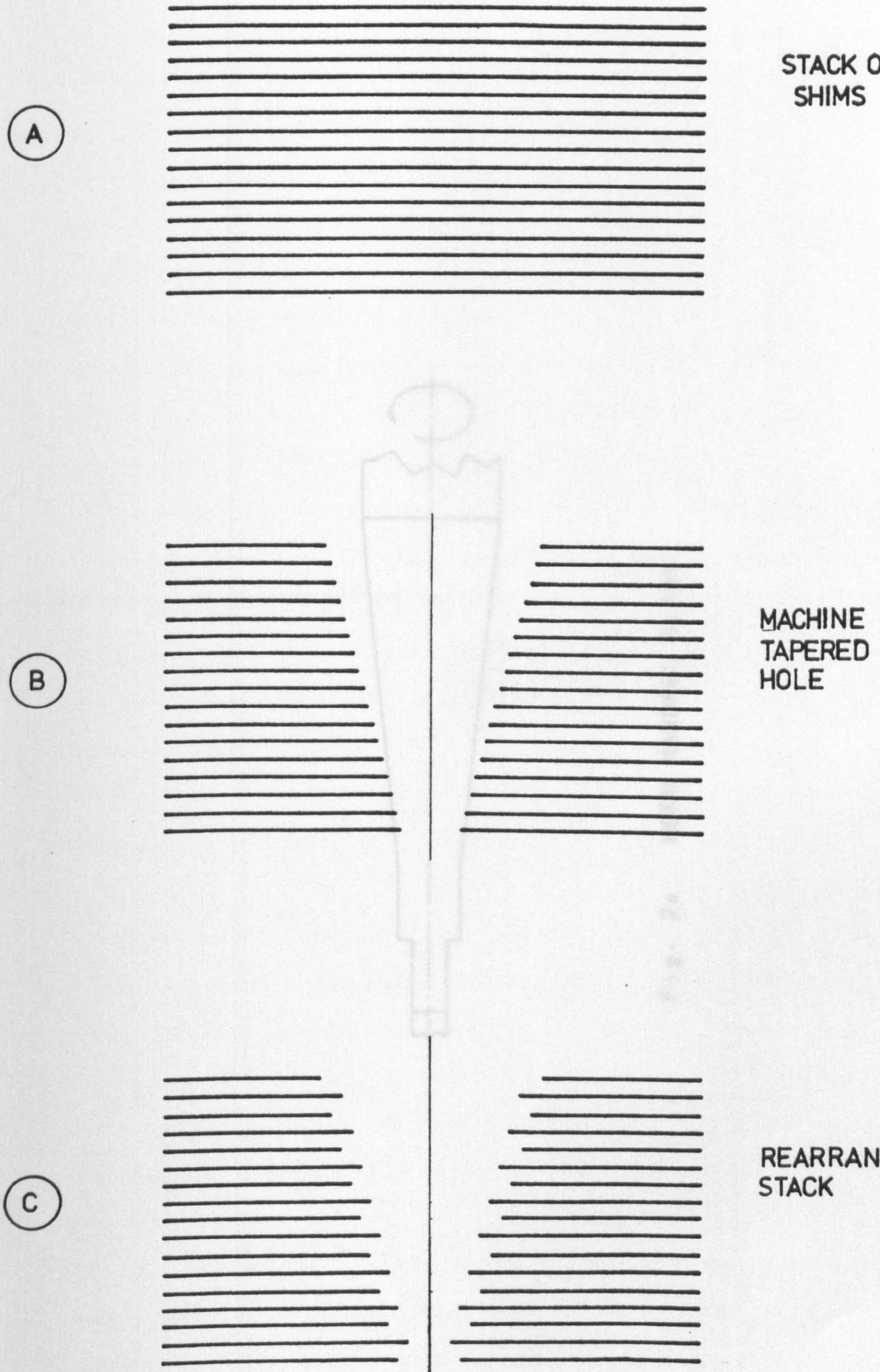

Fig. 2n

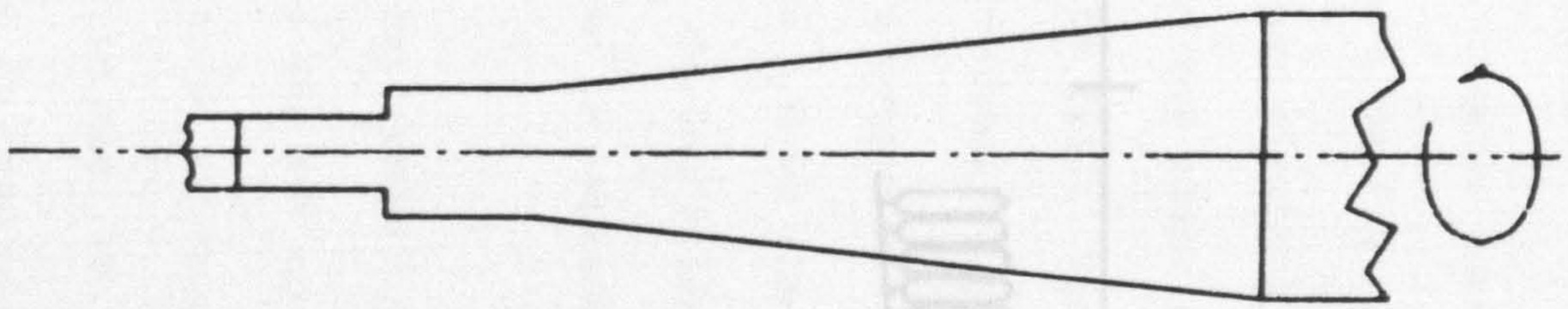

Fig. 2o HORN MANDREL BLANK

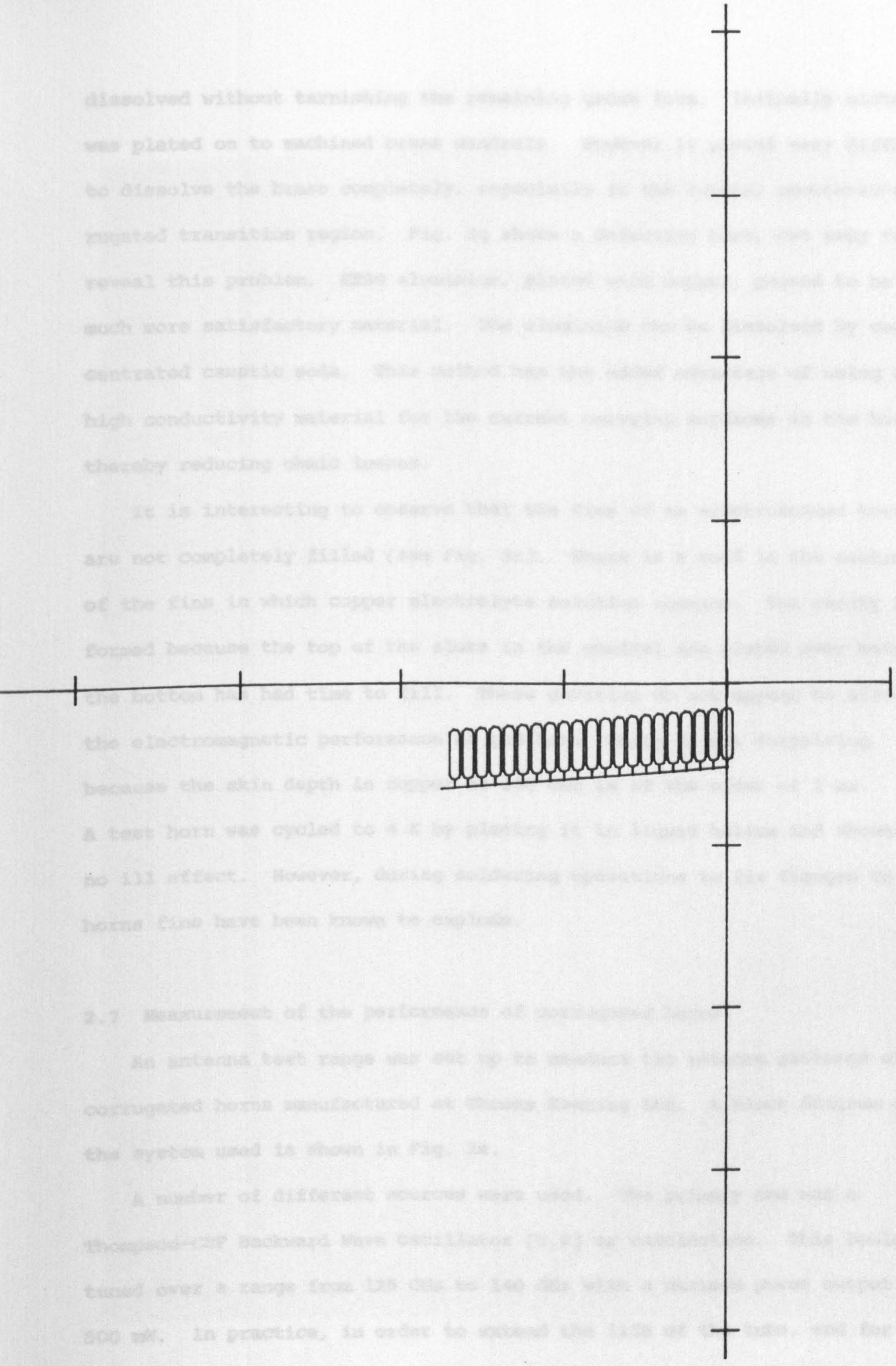

Fig. 2p

dissolved without tarnishing the remaining grown form. Initially nickel was plated on to machined brass mandrels. However it proved very difficult to dissolve the brass completely, especially in the crucial smooth-to-corrugated transition region. Fig. 2q shows a defective horn, cut away to reveal this problem. HE30 aluminium, plated with copper, proved to be a much more satisfactory material. The aluminium can be dissolved by concentrated caustic soda. This method has the added advantage of using a high conductivity material for the current carrying surfaces in the horn, thereby reducing ohmic losses.

It is interesting to observe that the fins of an electroformed horn are not completely filled (see Fig. 2r). There is a void in the centre of the fins in which copper electrolyte solution remains. The cavity is formed because the top of the slots in the mandrel are plated over before the bottom has had time to fill. These cavities do not appear to affect the electromagnetic performance of the horn, which is not surprising because the skin depth in copper at 100 GHz is of the order of 1 μm. A test horn was cycled to 4 K by placing it in liquid helium and showed no ill effect. However, during soldering operations to fix flanges to horns fins have been known to explode.

2.7 Measurement of the performance of corrugated horns

An antenna test range was set up to measure the antenna patterns of corrugated horns manufactured at Thomas Keating Ltd. A block diagram of the system used is shown in Fig. 2s.

A number of different sources were used. The primary one was a Thompson-CSF Backward Wave Oscillator [2.8] or carcinotron. This could be tuned over a range from 125 GHz to 140 GHz with a maximum power output of 500 mW. In practice, in order to extend the life of the tube, and for safety reasons, it was not run above 35 mW. It requires a bulky 5kV power supply, as well as water cooling. To measure patterns at other frequencies

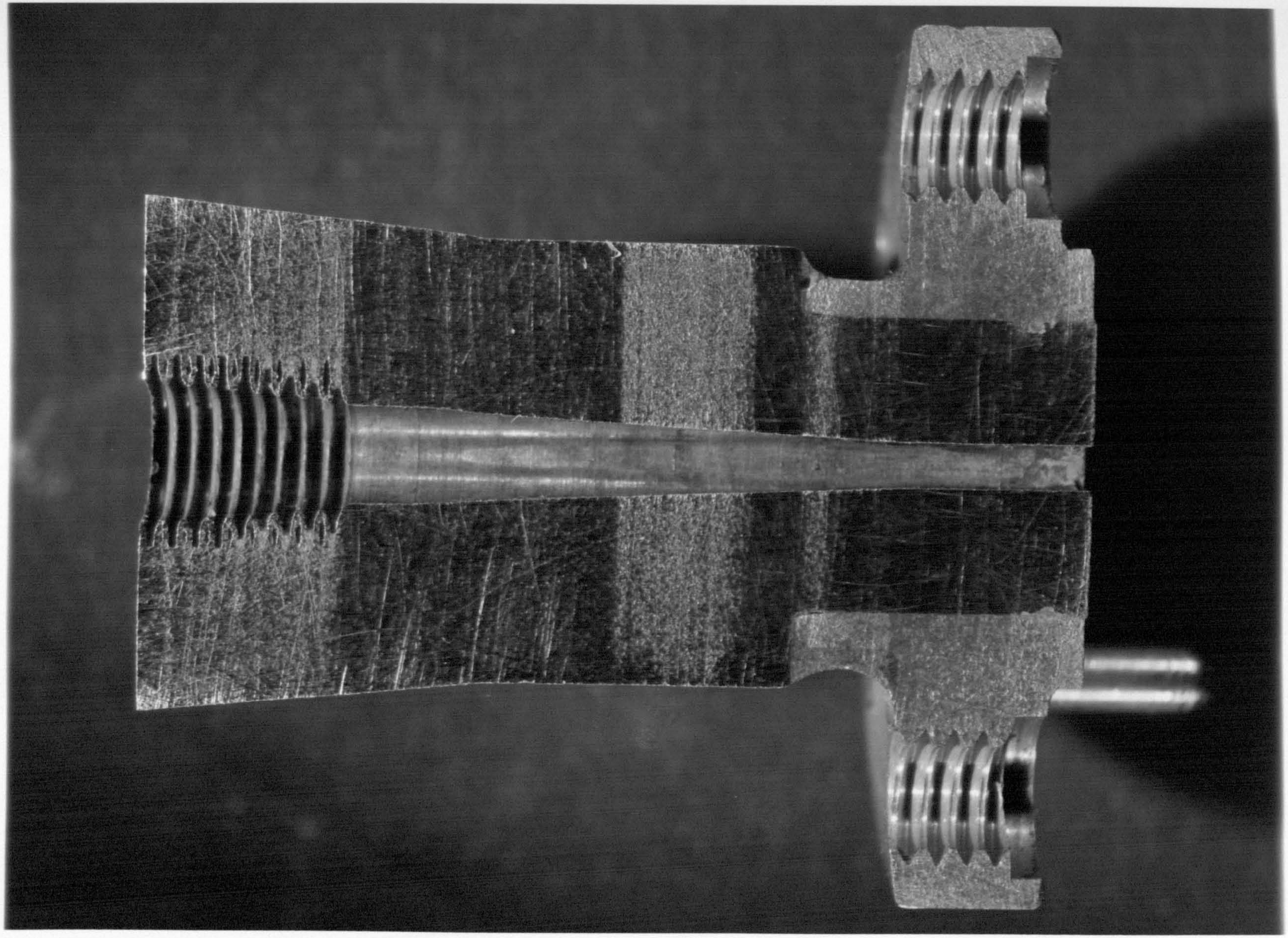

Fig. 2q

Fig. 2r

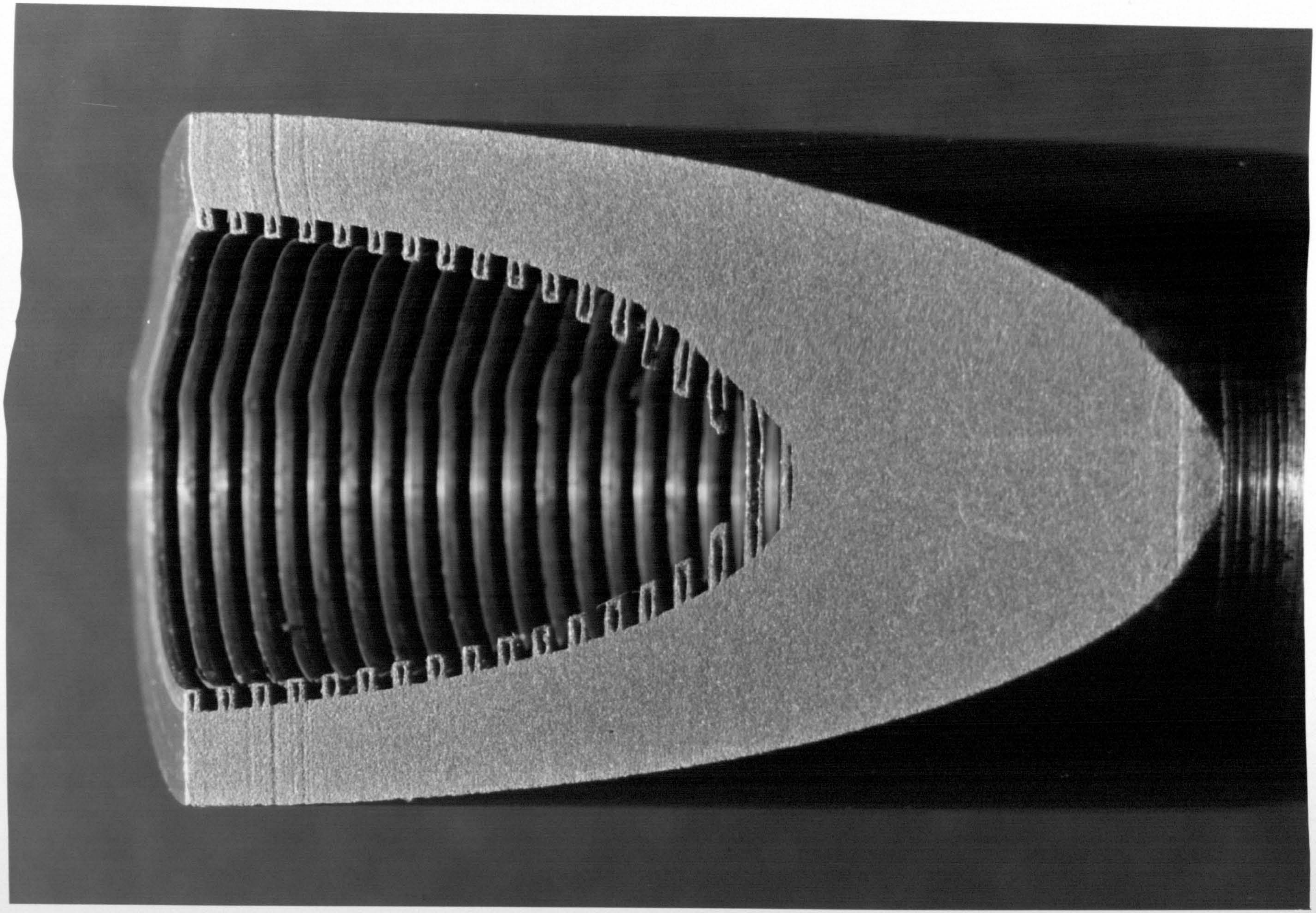

5

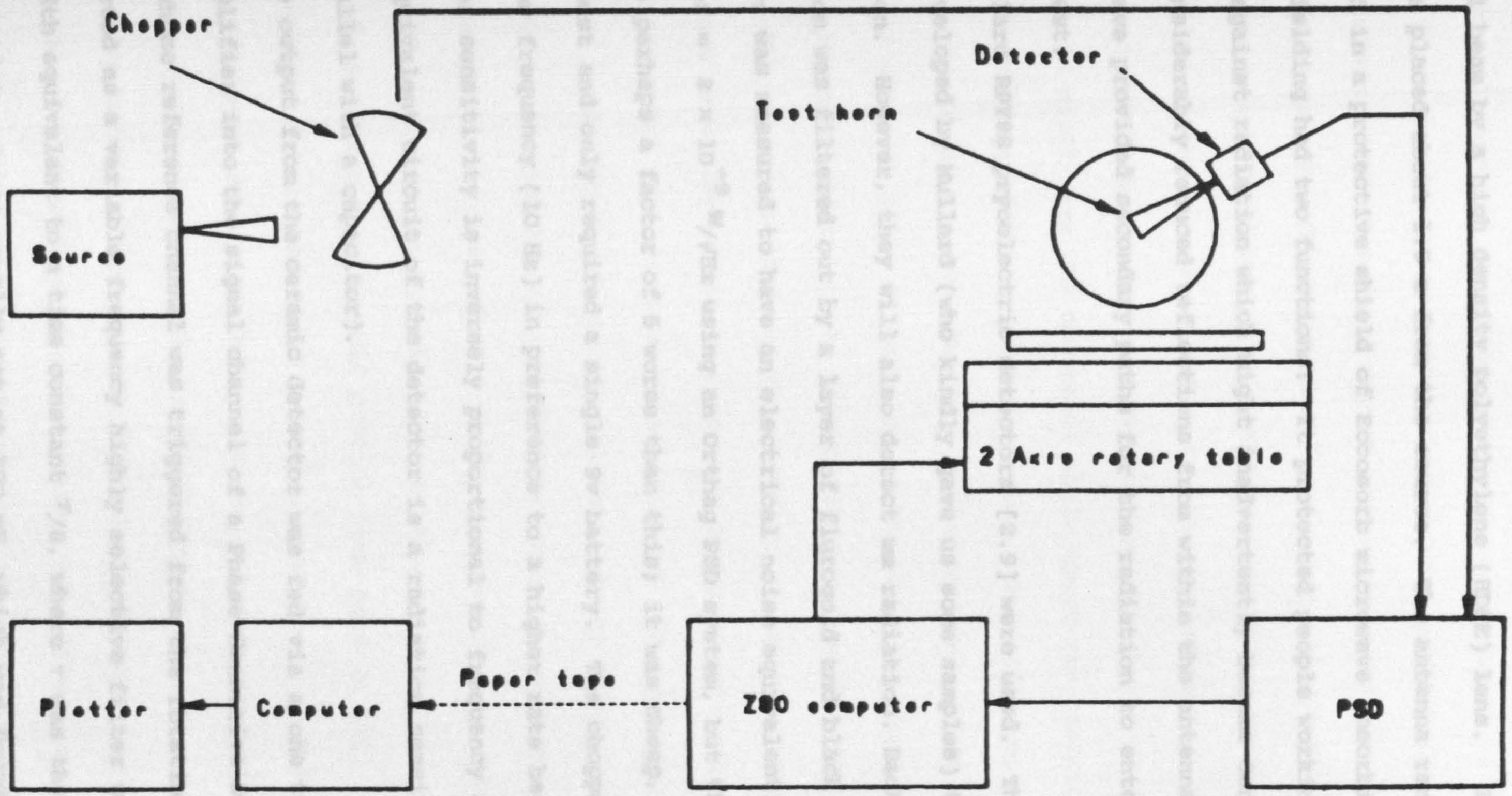

Fig. 2 : AUTOMATIC ANTENNA RANGE

Klystrons and IMPATTs were used. The beam was formed by a corrugated horn at the source and chopped at 10 Hz before being condensed into a quasi-parallel beam by a high density polyethylene (HDPE) lens. The horn under test was placed about 1.5 m from the source. The antenna range was enclosed in a protective shield of Eccosorb microwave absorbing material. This shielding had two functions: It protected people working close to the source against radiation which might inadvertently become concentrated. It also considerably reduced reflections from within the antenna range which might have provided secondary paths for the radiation to enter the horn under test.

Mullard RPY88 pryoelectric detectors [2.9] were used. These detectors were developed by Mullard (who kindly gave us some samples) to detect IR radiation. However, they will also detect mm radiation. Background IR radiation was filtered out by a layer of flurogold and black paper. The detector was measured to have an electrical noise equivalent power (NEP) of $\approx 3 \times 10^{-9}$ W/$\sqrt{Hz}$ using an Orthag PSD system, but the optical NEP was perhaps a factor of 5 worse than this; it was cheap, small and robust and only required a single 9v battery. The chopper operated at a low frequency (10 Hz) in preference to a higher rate because the detector sensitivity is inversely proportional to frequency above 10 Hz (the equivalent circuit of the detector is a radiation sensitive resistor in parallel with a capacitor).

The output from the ceramic detector was fed via a one transistor buffer amplifier into the signal channel of a Phase Sensitive Dectector (PSD) whose reference channel was triggered from the rotating chopper. The PSD acted as a variable frequency highly selective filter with a noise bandwidth equivalent to a time constant $\tau/8$, where τ was the smoothing time constant. τ was usually set at 300 mS, which was found to be sufficiently high to reduce noise caused mainly by current surges in in the stepping motor drives. This bandwidth allowed an independent

measurement to be taken approximately every 5 seconds. However, for low sidelobe measurements a 1 second time constant was often used.

The translation and recording equipment was designed to measure and plot two dimensional antenna patterns of mm wave horns automatically. A microprocessor provided a cheap way of controlling a digital voltmeter and two stepping motors. The two motors drove a two axis (ϕ,θ) table, each step of the motors producing a half degree angular movement. The mechanical construction of the coordinate table is illustrated in Fig. 2t. The position of the boom arm could be adjusted so that horns of differing length could still have the centre of their apertures positioned at the centre of rotation of the coordinate system. The software, written in Z80 machine code, moved the two axes in a raster motion. After each two degree step and a delay to allow integration of the detected signal to occur, the 8 bit analogue to digital (A to D) converter was read by the microprocessor. The value recorded was then printed out on paper tape. The program was generally set up to produce a 30 by 30 matrix of readings at 2 degree intervals. This involved the taking of 900 measurements, a task that would be difficult if not impossible to do by hand. A time constant of 300 mS on the phase sensitive detector required a delay of perhaps 5 seconds between readings. Thus a whole measurement took about an hour and a half. Because the dynamic range of the measurements required was more than the 8 bit A to D could provide (one part in 256), each measurement on a horn had to be repeated, with the A to D deliberately over loaded by a known amount on the second run. A dymamic range of 25 dB could thereby be achieved. The linearity of the A to D was checked and found to be limited by the one bit digital resolution.

The axes of the system provide a Ludwig type II antenna pattern measurement[2.10]. It is convenient to project the spherical geometry of the measurement coordinates on to a two dimensional Cartesian projection. However this results in distortion. This projection is similar to

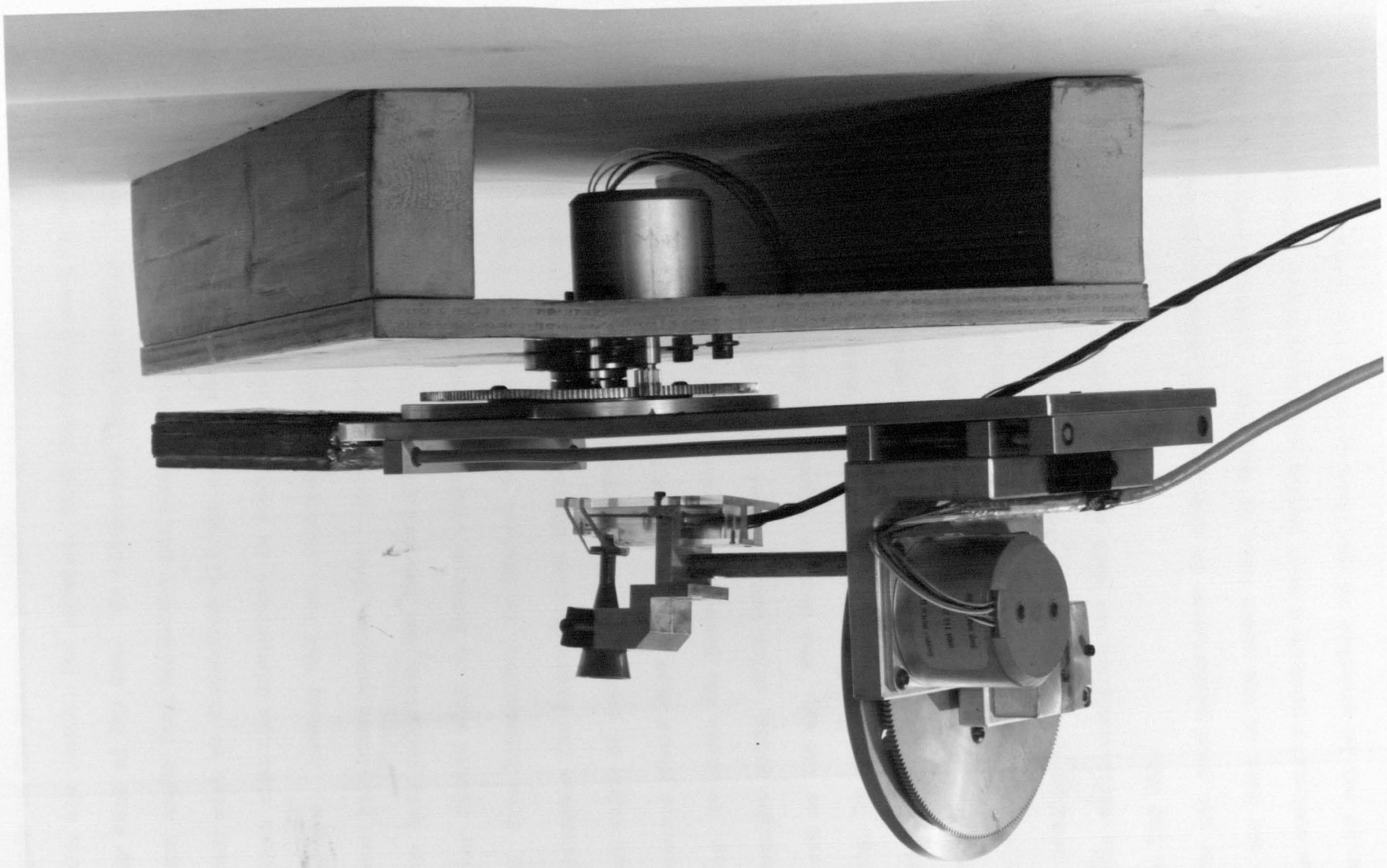

Fig. 2t

that made in the Mercator projection of the spherical Earth on to a flat map with the result, for example, that Iceland appears to have the same area as that of the USA. To illustrate this distortion, contours of constant angle from boresight are plotted in this projection in Fig. 2u. If there were no distortion all the curves would be circular. It can be seen that that the distortion is small for angles from boresight less than 45 degrees. Luckily the horn patterns measured on the antenna range did not have sidelobes greater than - 25 dB at angles greater than 45 degrees.

The data reduction and contour plotting software was run on a HP9835 computer fitted with an HP9872A graphics plotter. The data was first converted from hexadecimal to decimal and every second line of data reversed to unscramble the bidirectional raster motion of the (ϕ,θ) table. The maximum value of each set of measurements was used as the 0 dB reference. The contour plots were then generated with contour spacing in dB.

Fig. 2v shows the pattern of a smooth walled horn, fed from rectangular guide, which was designed by Dr. Nigel Cronin. It was measured at 126 GHz. The form is asymmetric and sidelobes exist at - 14 dB.

Fig. 2w shows the antenna pattern of a waveguide-fed corrugated horn having the dimensions shown in Fig. 2d, and measured at 130 GHz. It can be seen that the pattern is highly symmetric, and that no sidelobes exist above - 24 dB [2.11]. Although these results are expected from theory and from scaling from measurements taken at microwave frequencies, this plot was the first confirmation that corrugated horns could be made to work well above 100 GHz.

To get good performance in quasi-optical receivers it is important that the loss in the mixer horn is very low. Although corrugated feed horns obviously produce a much better antenna pattern than smooth horns, it would not be sensible to use them in receivers if their loss was significantly higher than smooth horns. There are two counterbalancing factors to consider. The $\underline{E}$ field in corrugated guide is less concentrated

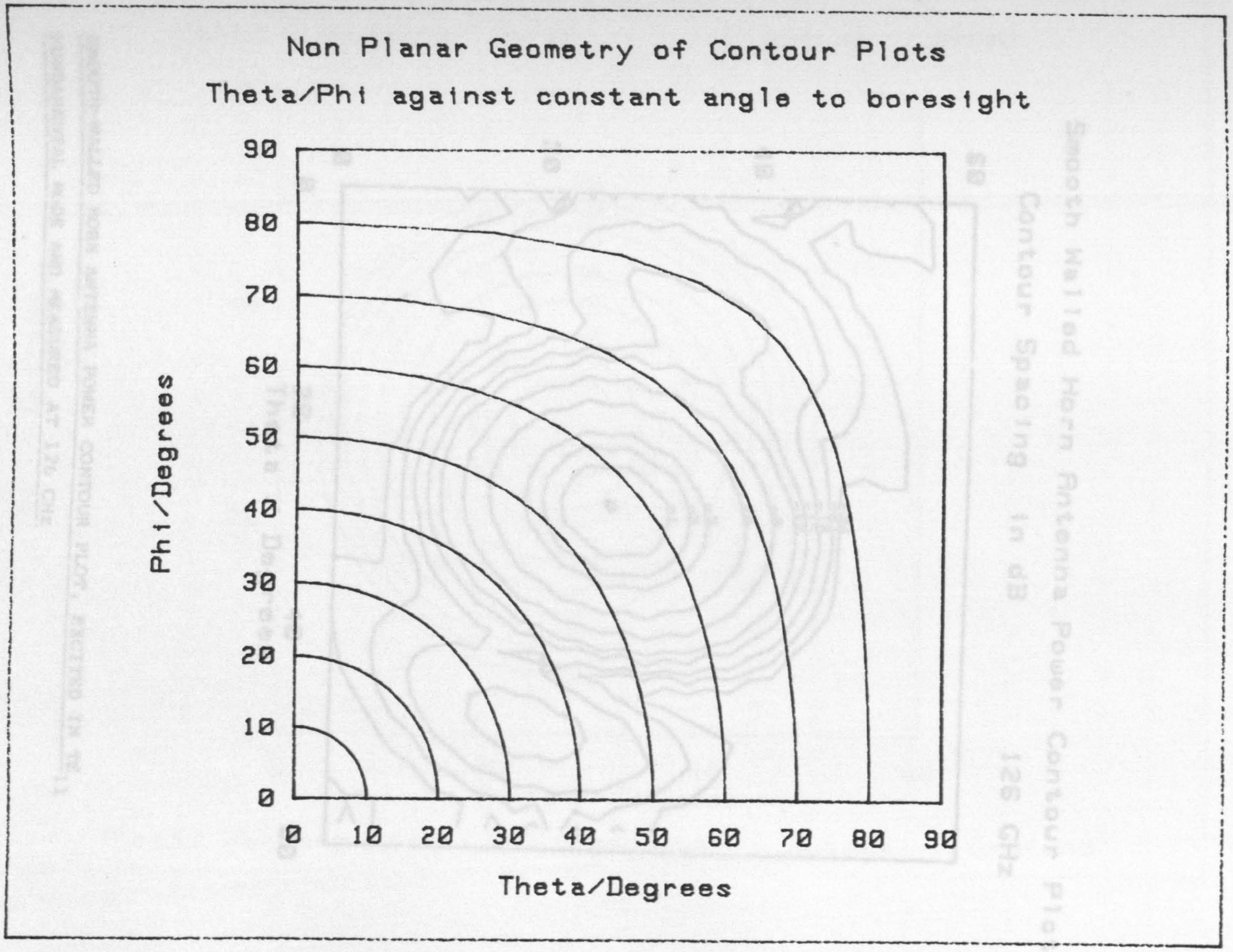
Non Planar Geometry of Contour Plots
Theta/Phi against constant angle to boresight
Phi/Degrees
90
80
70
60
50
40
30
20
10
0
0 10 20 30 40 50 60 70 80 90
Theta/Degrees

Fig. 2u

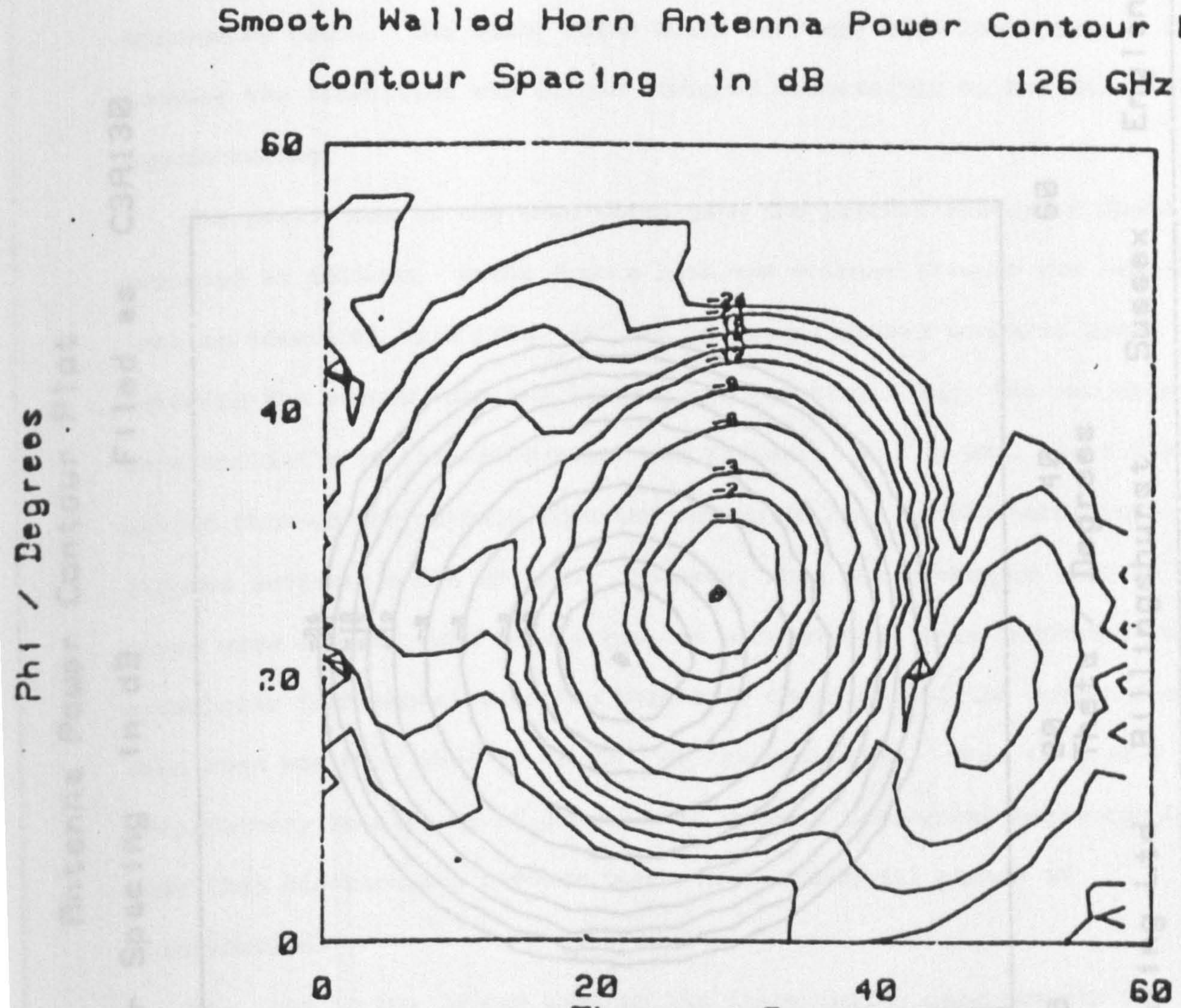

Fig. 2v

SMOOTH-WALLED HORN ANTENNA POWER CONTOUR PLOT, EXCITED IN TE_{11} FUNDAMENTAL MODE AND MEASURED AT 126 GHz

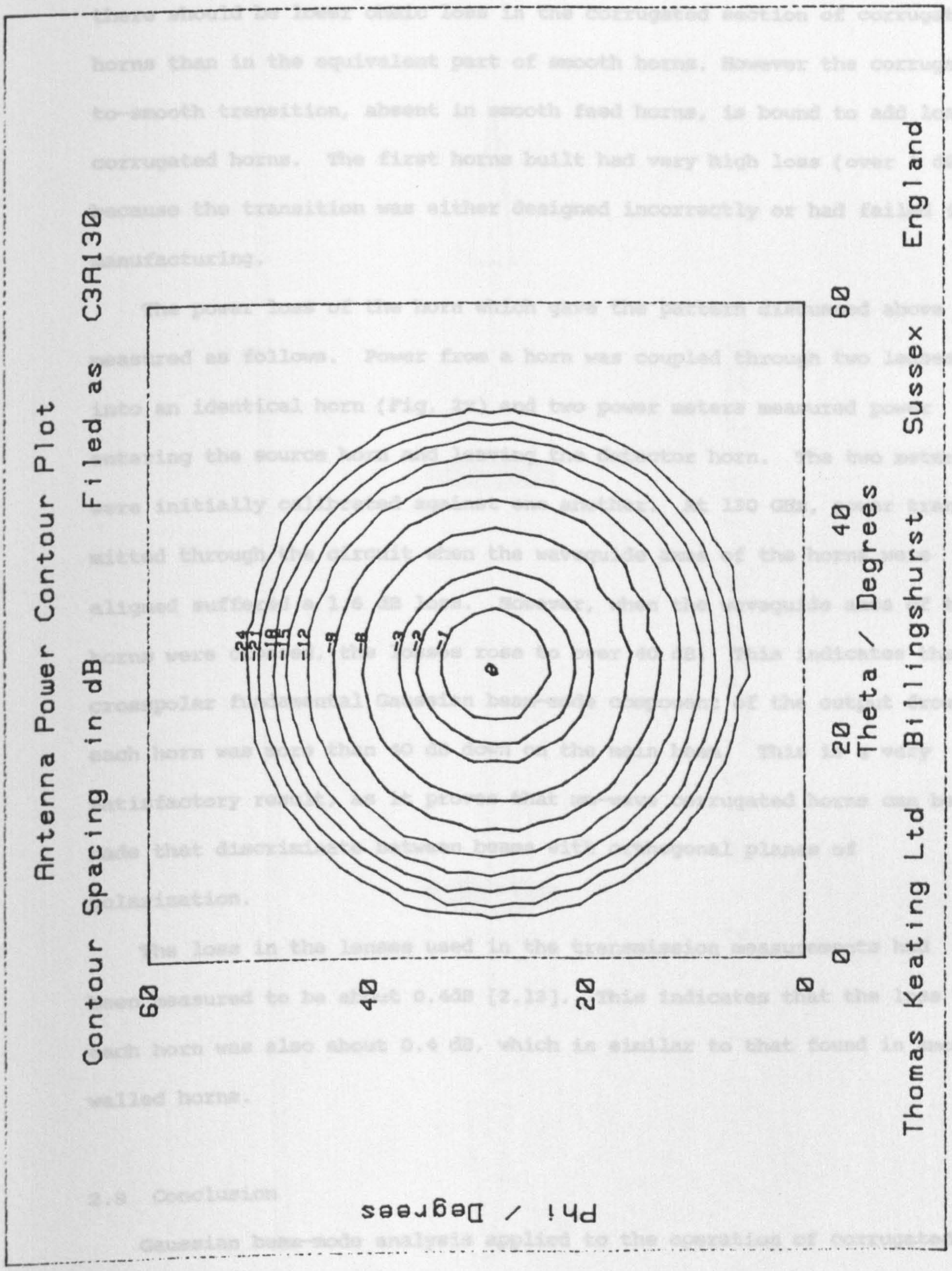
Antenna Power Contour Plot
Filed as C3A130
Contour Spacing in dB
-24
-21
-18
-15
-12
-9
-6
-3
-2
-1
0
60
40
20
0
0
20
40
60
Theta / Degrees
Phi / Degrees
Thomas Keating Ltd Billingshurst Sussex England

Fig. 2w

near the walls than in fundamental-moded smooth guide. This indicates that there should be lower ohmic loss in the corrugated section of corrugated horns than in the equivalent part of smooth horns. However the corrugated-to-smooth transition, absent in smooth feed horns, is bound to add loss to corrugated horns. The first horns built had very high loss (over 3 dB) because the transition was either designed incorrectly or had failed in manufacturing.

The power loss of the horn which gave the pattern discussed above was measured as follows. Power from a horn was coupled through two lenses into an identical horn (Fig. 2x) and two power meters measured power entering the source horn and leaving the detector horn. The two meters were initially calibrated against one another. At 130 GHz, power transmitted through the circuit when the waveguide axes of the horns were aligned suffered a 1.6 dB loss. However, when the waveguide axes of the horns were crossed, the losses rose to over 40 dB. This indicates that the crosspolar fundamental Gaussian beam-mode component of the output from each horn was more than 40 dB down on the main beam. This is a very satisfactory result, as it proves that mm-wave corrugated horns can be made that discriminate between beams with orthogonal planes of polarization.

The loss in the lenses used in the transmission measurements had been measured to be about 0.4dB [2.13]. This indicates that the loss in each horn was also about 0.4 dB, which is similar to that found in smooth-walled horns.

2.8 Conclusion

Gaussian beam-mode analysis applied to the operation of corrugated feed horns and indicates that they could be near ideal fundamental Gaussian beam-mode generators [2.13]. With proper attention to the internal form of of the horns, especially at the transition between

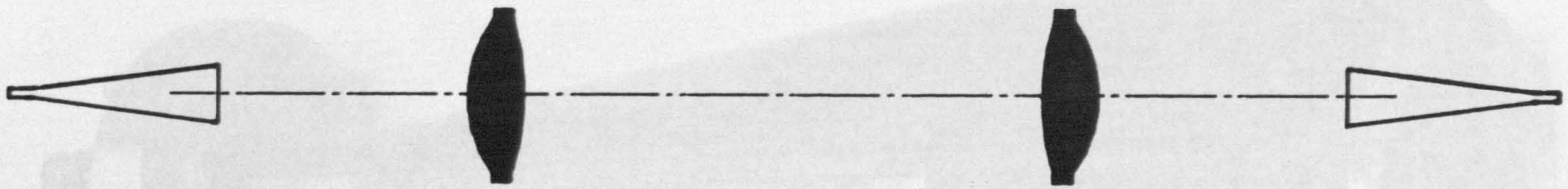

Fig. 2 x HORNS COUPLED BY TWO LENSES

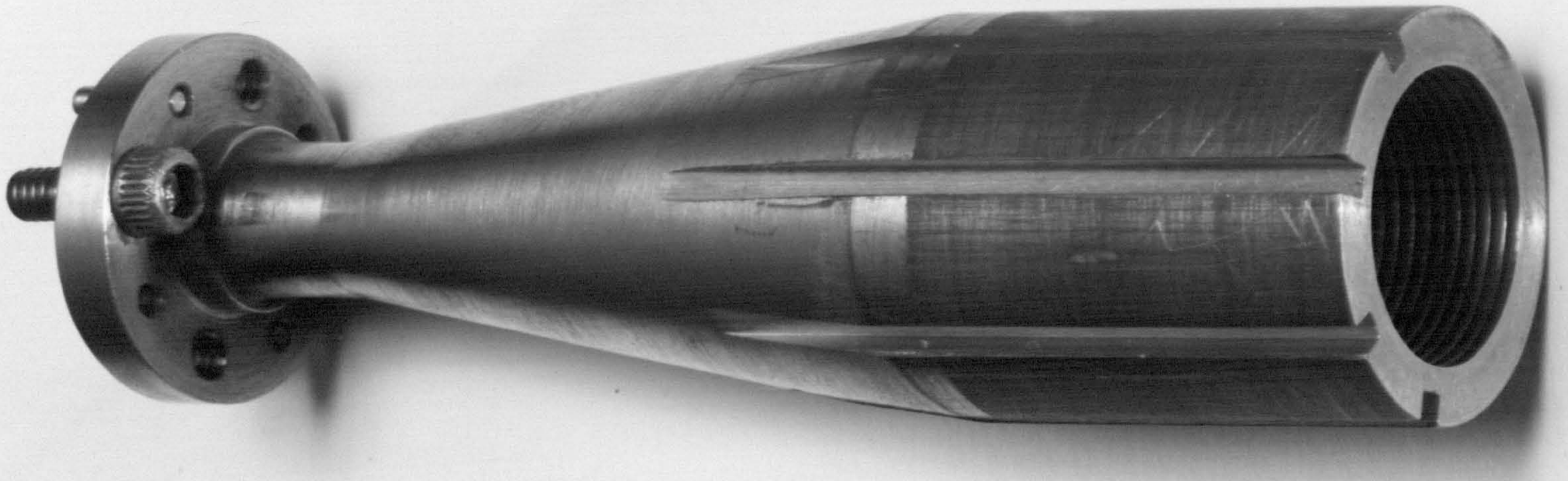

Fig. 2z

smooth and corrugated guide where the required HE_{11} mode is generated, advanced machining methods have manufactured corrugated horns that perform well at mm wavelengths (Fig. 2z). These have been shown to have low loss and to have low-sidelobe, axially symmetric, antenna patterns which show close agreement with theoretical predictions. As a result the coupling between corrugated horns in quasi-optical circuits is significantly better than that provided by smooth horns.

CHAPTER 3

POLARIZING DIRECTIONAL COUPLERS AND BEAM CONTROL LENSES

3.1 Introduction

The construction and use of wire polarizing grids which act as polarization-sensitive directional couplers are considered in the first part of this chapter. The second part is concerned with the use of lenses as beam re-forming components for Gaussian beam-modes.

3.2 Polarizing grids

Planar grids of parallel thin metallic wires with a spacing much smaller than the wavelength of the incident beam will split a Gaussian beam into two orthogonally polarized components, one component being transmitted through the grid without change of direction and the other being reflected as if the grid were a plane metallic reflector. The component of the incident beam which is transmitted is that with its E-field perpendicular to the wires, because the wires are simply polarized by the field. The orthogonally polarized component is reflected because its E-field induces currents to flow along the wires in the same way as would occur if the field was incident on a metallic reflector. Provided the wire spacing is about $\lambda/100$, and the grid is flat to $\lambda/100$, the efficiencies of a grid are very high both for transmission and reflection [3.1]. The resistivity of the metal of the wire, its thickness and the constancy of the wire spacing are not of critical importance.

In quasi-optical circuits, described in Chapter 5, each grid is set with its plane at 45^{o} to the direction of propagation of the incident beam, and is supported on a rectangular frame with the long side a factor of $\sqrt{2}$ larger than the the short side. It therefore presents a square cross-section to the beam. Grids can be wound vertically or horizontally. However to present a pass plane at 45^{o} to the vertical the wires should

be set at an angle of $\tan^{-1}1/2$ to the short side. This ensures that the wires lie at an angle of 45^{o} when viewed along a beam axis.

The grids are wound using a coil-winder, adapted to cope with lightly-tensioned tungsten wire. The wire is wound around a rectangular plate which is recessed to carry the stainless steel frame to which the wires are to be fixed; the recess is machined at the appropriate angle to the axis of rotation of the plate. When the winding is finished, the wires are glued to the grid-frame using cold-setting epoxy resin and a keeper-frame, aligned by dowels, is glued on top. The grid-frame and keeper frame have the same thickness and internal dimensions but the external dimensions of the keeper-frame are slightly smaller than those of the grid-frame to allow the secure mounting and location of the grid in its half cube holder (see Chapter 5).

3.3 Lens design

Lenses are required in quasi-optical systems to refocus the beams as they propagate through the circuit. In Chapter 5 it will be shown that the diameter of the lenses and the separation between them in compact quasi-optical circuits are large enough compared with the wavelength for the radii of curvature of the phase-fronts at lenses, and of the lens surfaces, to be much larger than λ. Snell's law (or more conveniently Fermat's principle) can therefore be used locally to design the surface profile of lenses [1.6] as follows.

Each lens can be thought of as being made up of two plano-convex lenses with a plane disk between them to provide a mounting flange. The profile of the lens surface is calculated to refract an incident Gaussian beam-mode of beamwaist W_o into a plane phase front of width W_1 at the central plane of the lens. Fermat's principle indicates that the phase change of a ray moving from the beamwaist to the centre of the lens should

not change as the point at which the ray enters the lens is varied. So, referring to Fig. 3a,

$$\frac{\partial}{\partial r}\left[-k_o z_q - \frac{\pi r^2}{\lambda R_q} + \tan^{-1} \frac{z_q}{z_q} - k_o \mu (z_1 - z_q) \right] = 0 . \qquad (3.1)$$

The values of W_o, λ, μ, z_1 and the lens radius are given; and from (1.7) and (1.4)

$$\frac{z}{z} = \frac{\lambda (z - z_o)}{\pi^2 W_o} , \qquad (3.2)$$

and $$R_1 = (z_1 - z_o)\left[1 + \frac{1}{\frac{z_1}{z_1}^2} \right] . \qquad (3.3)$$

A program to solve equation (3.1) for z_1 was written to provide dimensions of lens profiles converting one Gaussian beam-mode into another, given the parameters of the mode.

3.4 Lens materials

Lenses for mm wave systems must be made from materials of suitable refrative index (RI) and low loss. Traditional materials are shown in Table 3b taken from [1.6].

The major problem associated with lenses in mm wave systems is that of reflections from lens surfaces back into the fundamental Gaussian beam-mode interfering with one another to generate standing waves. The direct loss of signal is often unimportant compared with resonance effects. One obvious precaution is to ensure that no lens surface should coincide with a signal beam phase front so that reflected beams can not interfere fully with the signal beam. However, there will be some coupling and this has been estimated by Martin [1.6], drawing on work by Kogelnik [3.2]. Martin

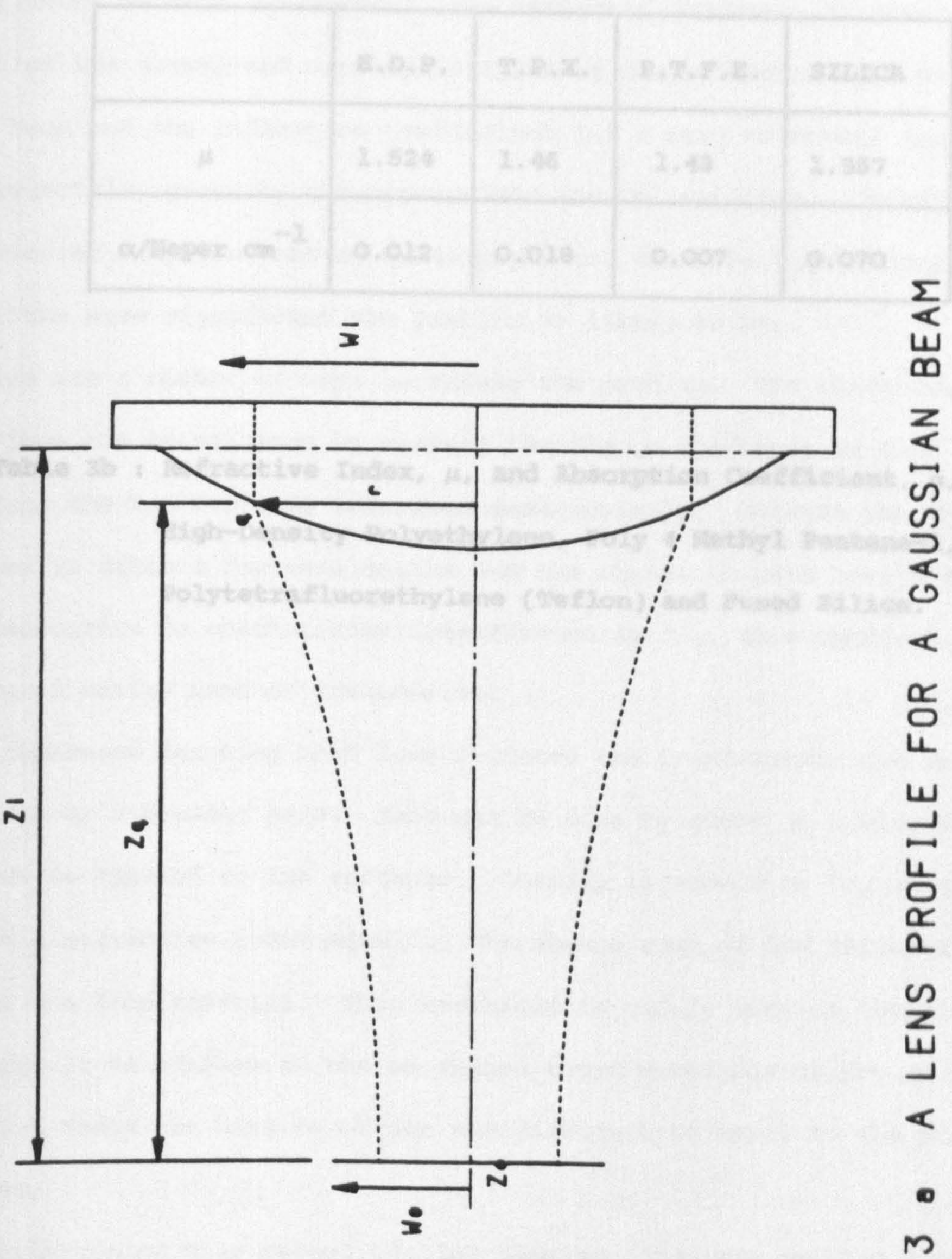

Fig 3 a A LENS PROFILE FOR A GAUSSIAN BEAM

	H.D.P.	T.P.X.	P.T.F.E.	SILICA
μ	1.524	1.46	1.43	1.957
α/Neper cm^{-1}	0.012	0.018	0.007	0.070

Table 3b : Refractive Index, μ, and Absorption Coefficient, α, for High-Density Polyethylene, Poly 4 Methyl Pentene-1, Polytetrafluorethylene (Teflon) and Fused Silica.

represented the reflected beam as a superposition of a fundamental mode having the same beamwaist as the fundamental signal beam, and higher order modes. The fundamental beam will propagate through the system, as would a time reversed version of the signal beam, and will cause standing waves. The higher modes will eventually leak from the system and can be ignored. The amplitude of this fundamental beam reflected component is given by the product of the normalised overlap integral of the reflected beam with the signal beam and the reflection coefficient for a wave at normal incidence on a dielectric, given by the appropriate Fresnel equation. Unfortunately the reflected component can be quite high, and the more highly coupled the circuit the more significant the problem is likely to be.

There are a number of ways to reduce the problem. The thickness of the lens can be adjusted by varying the flange thickness so that reflections from the two surfaces interfere destructively. Because the thickness of lenses is often a few wavelengths and the change in path length to move from destructive to constructive interference is $\lambda/4$, this approach works only over a narrow band of frequencies.

By impedence matching both lens surfaces the transmission can be improved over a broader band. This can be done by means of a blooming layer can be applied to the surfaces. Ideally it should be $\lambda/4$ thick and have a refractive index equal to the square root of the refractive index of the lens material. This technique is widely used in the visible, but difficult to achieve in the mm region where materials of the correct refractive index are hard to obtain and difficult to apply to the surface of lenses.

A variation of this method, called blazing, involves cutting grooves in the surface of the lens to a depth of $\lambda/4$. The aim is to remove enough material to give an average density which again has the refractive index of the square root of the refractive index of the main lens material. Blazed

high density polyethylene (HDPE) lenses were made for the 115 GHz receiver described in Chapter 8. Smooth lens blanks were turned with the aid of a template designed with the aid of the program outlined above. Grooves 0.5 mm wide and 0.6 mm deep, with a mark-space ratio of 1, were then cut in annular rings out from the centre of both lens surfaces. Radiometric tests on these lenses indicated that impedence matching was improved and that transmission losses were reduced by 0.2 dB compared with similar unblazed lenses.

The three techniques can reduce reflections, but only over a narrow frequency band because their operation depends on the reduced distance between reflecting surfaces. All of these problems could be avoided by making lenses from a material with a sufficiently low RI that reflections would be small enough to be acceptable. However, the thickness of a lens of a given power obviously increases as the RI of the material is reduced. Too great a thickness can cause problems because the lens will act on different parts of the beam at different distances along the propagation This is undesirable because mode mixing will occur between the Gaussian beam-modes.

A search was made for a material with a RI between 1.25 and 1.35 and low loss at mm wavelengths. A refractive index around 1.3 would keep reflections to an acceptable limit without generating mode mixing. It was thought that a foamed material, such as polypropylene and polyethylene, might be suitable. Foamed polyurethane and polystyrene, used at microwave frequencies to make lenses, are unsuitable because they have too high a loss tangent at mm frequencies. As a first order approximation, the bulk permitivity of foamed material should reduce with the density. The RI should therefore reduce as the square root of the density. High density polyethylene (HDPE) has a density of about 950 Kg m^{-3}. Thus to achieve a RI of 1.3 would require a density of $(0.3/0.52)^2 * 950$ Kg $m^{-3} \approx 300$ Kg m^{-3}.

Foamed polyethylene and polypropylene are used in the packaging industry and can easily be obtained at densities up to 100 Kg m^{-3}. ICI manufacture polypropylene for the furniture industry down to a density of 700 Kg m^{-3} [3.3]. This is made by injection moulding with a gassing agent. Unfortunately the cell size is about 1 mm and samples proved to have a high loss at mm wavelenths through scattering. It proved impossible to obtain samples of either material between densities of 100 and 780 Kg m^{-3}.

The highest density of polyethylene found had a density of 200 Kg m^{-3}. Called Alveolite, it has a closed cell structure linked by irradiation. Unfortunately the maximum thickness made by the manufacturer (Sekisui UK Ltd.) was 3 mm [3.4]. The cell size was less than 0.1 mm, too small to cause scattering to mm waves, and samples proved highly transmitting. The RI of the material was measured to be 1.13 at 130 GHz by inserting a sample into the signal channel of a null reflectometer (see Chapter 6) and readjusting the position of the variable reflector in the reference channel to restore the initial conditions. It was decided to laminate and compress the material to generate samples of higher density and thick enough to be used for lenses. This work was undertaken by Dr. J. Card. The 3 mm thick Alveolite sheets were cleaned with Xylene and then stacked 10 sheets high. These were then placed in a temperature controlled oven and the temperature slowly raised to 140°C - close to the plastic temperature. The samples were then compressed with a weight to half the original thickness. The samples were allowed to cool slowly, and were found to be permanently bonded together. Their RI was measured using the null reflectometer and found to be 1.275 - an acceptable value. This value of the RI was then used to calculate the lens profiles for the 115 GHz (see Chapter 8) receiver by equation (3.1) and brass templates were then prepared on an NC milling machine.

The lens material was quite difficult to machine. It was not possible to turn the material as it had a tendency to tear. After some experimentation, it proved possible to grind it: the profile of the lens was transferred from the brass template to a grit grinding wheel using a Diaform on a standard surface grinder (J&S 540), and the lens blank was slowly rotated under the grinding wheel until the correct profile was formed.

The 115 GHz receiver's foamed lenses proved slightly disappointing. Although reflections were low, their internal losses proved to be quite high. This was thought to be caused by scattering at junctions between layers of the foam.

The performance of lenses remains the major limiting factor on the performance of quasi-optical circuits and work to develop better lenses is continuing.

CHAPTER 4

QUASI-OPTICAL ISOLATORS

4.1 Introduction

This chapter traces the development of a working quasi-optical isolator designed to operate just above 100 GHz. Isolators are one of a class of non-reciprocal devices which improve the performance of EM systems by reducing or suppressing unwanted reflections. An investigation of the mm wave Faraday rotation properties of some ferrite materials, extending that made by S.S.D.V. Rughooputh [4.1] as a third year undergraduate in the Physics Department in QMC, is described. The need for blooming the highly refractive ferrite material is discussed, and computer calculations on the effect of blooming on the bandwidth and performance are outlined. Measurements showing that an isolator with an acceptable level of performance has been made are given.

Isolators transmit wave energy in one direction, but attenuate it highly in the other. They are generally used to improve the stability of EM power sources by stopping reflected power from re-entering the source. For example, IMPATTs are very susceptible to what is known as "pulling". Their output power and frequency alter if the impedence of the device they are matched to changes, as occurs when a wave is reflected back into the device. The two figures of merit for an isolator are the insertion loss in the transmission path, which should be as low as possible, and the return loss or attenuation in the reverse path, which should be as high as possible. Typical performance for waveguide isolators just below 100 GHz is 1 dB insertion loss and a return loss, or isolation, of 15 to 20 dB.

4.2 The operation of a Faraday isolator

The isolator described in this chapter makes use of the Faraday

rotation effect. The plane of polarization of a wave propagating along the magnetic axis of a suitable ferrite suffers rotation. A reflected wave, travelling in the opposite direction also suffers rotation, but in the same sense as the forward wave. In a working isolator the thickness of the ferrite is adjusted to generate a 45 degree rotation in the forward path. Thus a wave passing first through the isolator and then back after reflection undergoes a rotation of 90 degrees. This reflected wave, being orthogonally polarized to the initial wave, is easy to remove, using a polarizing filter such as a wire grid. Fig. 4a illustrates this.

A characteristic property of a ferrite in a magnetic field is that, although it has a scalar relative permittivity, it has a tensor relative permeability at microwave and millimetre wave frequencies. This tensor permeability gives rise to a number of important non-reciprocal effects, of which the Faraday effect is one.

Consider an elementary magnetic dipole of moment μ placed in a magnetic field $\underline{H}_o$, assumed to be in the z axis [4.2]. Under equilibrium conditions the dipole moment vector will line up with the magnetic field. However, if it is disturbed from its position, the torque experienced by the dipole will be

$$\underline{T} = \underline{\mu} \times \mu_o \underline{H}_o \quad , \tag{4.1}$$

where μ_o is the free space permeability (see Fig. 4b).

Also associated with a dipole is an angular momentum $\underline{J}$. For an unpaired electron it is given by:

$$\underline{\mu} = -\gamma \underline{J} \tag{4.2}$$

where γ is the gyromagnetic ratio of the electron. Since the rate of change of angular momentum is given by the applied torque we have:

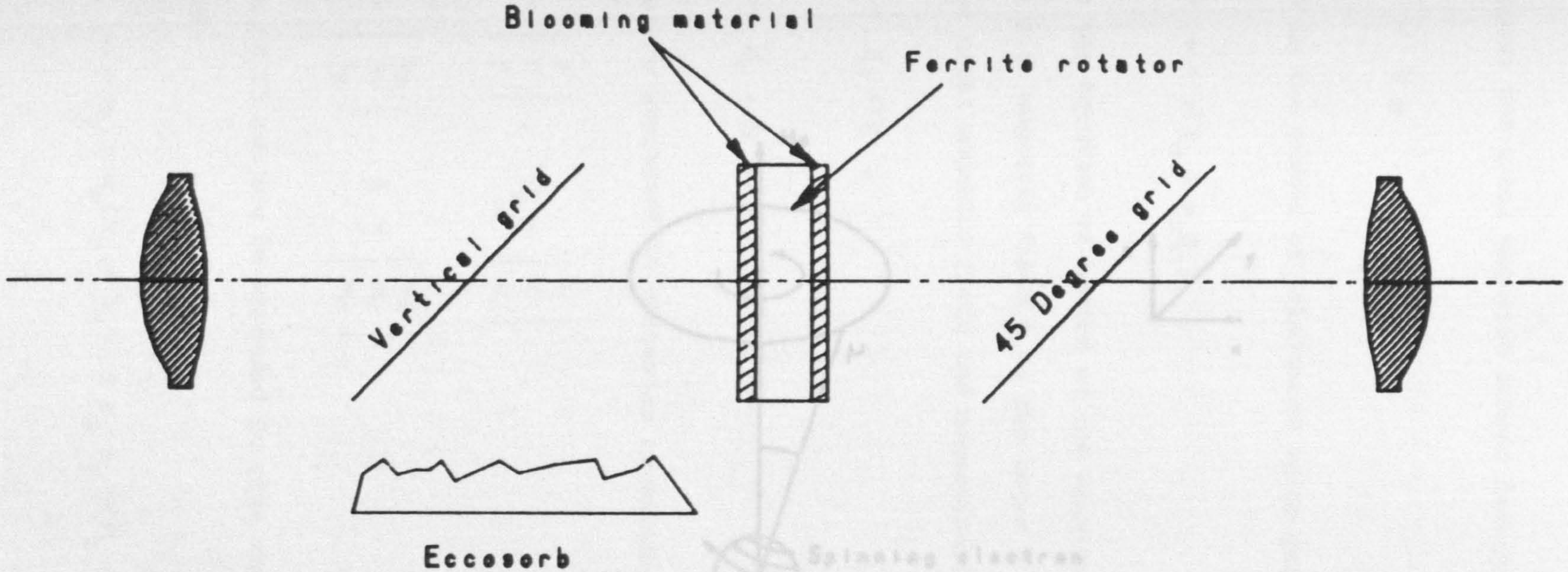

Fig. 4 a QUASI-OPTICAL ISOLATOR

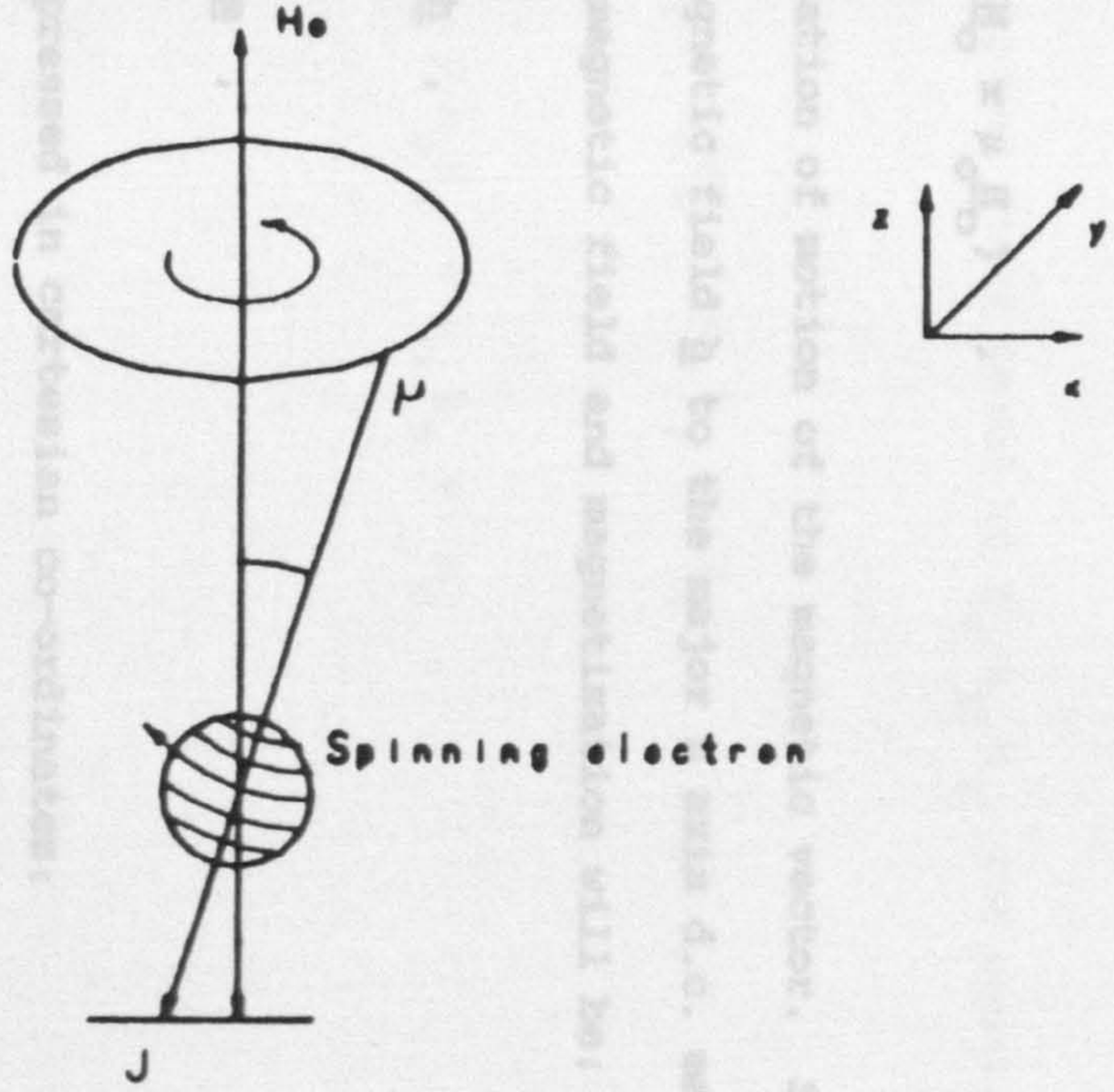

Fig. 4 b MAGNETIC MOMENT PRECESSION

$$\frac{d\underline{\mu}}{dt} = -\gamma(\underline{\mu} \times \mu_o \underline{H}_o) \quad . \tag{4.3}$$

Now suppose the total magnetic moment density is given by

$$\underline{M}_o = N\underline{\mu} \quad , \tag{4.4}$$

where N is the number of unbalanced spins per unit volume. Then

$$\frac{d\underline{M}_o}{dt} = -\gamma(\underline{M}_o \times \mu_o \underline{H}_o) \quad , \tag{4.5}$$

This is the equation of motion of the magnetic vector. Suppose now we add a small r.f. magnetic field $\underline{h}$ to the major z axis d.c. magnetic component. Then the total magnetic field and magnetisation will be:

$$\underline{H} = \underline{H}_o + \underline{h} \quad , \tag{4.6}$$

$$\underline{M} = \underline{M}_o + \underline{m} \quad , \tag{4.7}$$

which can be expressed in cartesian co-ordinates:

$$\underline{H}_o = \begin{bmatrix} 0 \\ 0 \\ H \end{bmatrix} \quad , \quad \underline{M}_o = \begin{bmatrix} 0 \\ 0 \\ M \end{bmatrix} \quad , \tag{4.8),(4.9}$$

$$\underline{h} = \begin{bmatrix} h_x \\ h_y \\ h_z \end{bmatrix} \quad , \quad \underline{m} = \begin{bmatrix} m_x \\ m_y \\ m_z \end{bmatrix} \quad . \tag{4.10),(4.11}$$

Equation (4.5) can now be expanded to give three simultaneous differential equations:

$$\frac{dm_x}{dt} = -m_y \gamma \mu_o(H_o + h_z) + \mu_o h_y \gamma(M_o + m_z) \quad , \tag{4.12a}$$

$$\frac{dm_y}{dt} = -m_x \gamma \mu_o(H_o + h_z) + \mu_o h_x \gamma(M_o + m_z) \quad , \tag{4.12b}$$

and

$$\frac{dm_z}{dt} = - m_x \gamma \mu_o h_y + m_y \gamma \mu_o h_x . \qquad (4.12c)$$

Assuming that the r.f field is small compared to the d.c. field,

ie $h_{x,y,z} << H_o$,

then, ignoring second order terms in h_x, h_y, h_z, the equations of motion reduce to:

$$\frac{dm_x}{dt} = - m_y \gamma \mu_o H_o + \mu_o h_y \gamma M_o , \qquad (4.13a)$$

$$\frac{dm_y}{dt} = - m_x \gamma \mu_o H_o + \mu_o h_x \gamma M_o , \qquad (4.13b)$$

and

$$\frac{dm_z}{dt} \approx 0 . \qquad (4.13c)$$

Putting

$$\omega_m = \mu_o \gamma M_o \quad \text{and} \quad \omega_o = \mu_o \gamma H_o$$

we have by substitution:

$$\frac{d^2 m_x}{dt^2} + \omega_o^2 m_x = \omega_m \omega_o h_x + \omega_m \frac{dh_y}{dt} , \qquad (4.14a)$$

$$\frac{d^2 m_y}{dt^2} + \omega_o^2 m_y = \omega_m \omega_o h_y - \omega_m \frac{dh_x}{dt} , \qquad (4.14b)$$

and

$$m_z \approx 0 \quad . \tag{4.14c}$$

Suppose the r.f. quantities have the form $e^{i\omega t}$, where ω is the frequency of the incident field. Then equation [4.14] can be solved to give a tensor value of the susceptibility,

$$\underline{m} = [\,X\,]\,\underline{h} \quad , \tag{4.15}$$

$$\text{where} \quad [X] = \begin{bmatrix} X_{xx} & X_{xy} & 0 \\ X_{yx} & X_{yy} & 0 \\ 0 & 0 & 0 \end{bmatrix} \quad ,$$

$$X_{xx} = X_{yy} = \frac{\omega_m \omega_o}{-\omega^2 + \omega_o^2} \quad ,$$

$$\text{and} \quad -X_{yx} = X_{xy} = \frac{i\,\omega\,\omega_m}{-\omega^2 + \omega_o^2} \quad .$$

It is possible to diagonalise the matrix [X] and derive a scalar susceptibility provided that the applied field $\underline{h}$ is adjusted to be one of the eigenvectors of the eigenequation:

$$\chi\,\underline{h} = [X]\,\underline{h} \quad . \tag{4.16}$$

It can be shown that this occurs for

$$\underline{h} = \frac{1}{\sqrt{2}} \begin{bmatrix} h_o \\ i\,h_o \\ 0 \end{bmatrix} \tag{4.17a}$$

or

$$\underline{h} = \frac{1}{\sqrt{2}} \begin{bmatrix} h_o \\ -i\, h_o \\ 0 \end{bmatrix} \quad . \tag{4.17b}$$

As one might expect, these two vectors correspond to clockwise and anticlockwise circularly polarized fields. The scalar susceptibility is

$$\chi = \frac{\omega_m}{\omega_o \mp \omega} \quad , \tag{4.18}$$

and the refractive index, N, is given by

$$N = \left[\epsilon_r \left[1 + \frac{\omega_m}{\omega_o \mp \omega} \right] \right]^{1/2} \quad , \tag{4.19}$$

where ϵ_r is the relative permittivity.

Assuming that the susceptibility is small, the difference δ in the two refractive indices is given by ($\omega_o \ll \omega_m, \omega$):

$$\delta = \left[\frac{1}{2} \epsilon_r \left[\frac{\omega_m}{\omega_o + \omega} - \frac{\omega_m}{\omega_o - \omega} \right] \right]^{1/2} \quad . \tag{4.20}$$

It is instructive to consider the relative values of ω and ω_o. The gyromagnetic ratio γ of the electron has a value of $1.76 \times 10^{11}\ s^{-1}T^{1}$ and $\mu_o = 4\pi \times 10^{-7}\ T\ m\ A^{-1}$ by definition. A typical ferrite, such as used in the isolator presented below, might have a magnetic field of 2.5×10^{5} A/M. Thus ω_m is of the order of 5×10^{10} rad sec^{-1}, and lies in the microwave region of the EM spectrum. At 100 GHz, $\omega = 2\pi \times 10^{11}$ rad sec^{-1}. Therefore, in the mm region $\omega > \omega_o$, equation (4.20) can be simplified so that δ, the difference between the two refractive indices, becomes:

$$\delta = \epsilon_r^{1/2} \frac{\omega_m}{\omega} . \qquad (4.22)$$

The difference in the refractive indices of clockwise (CW) and counter-clockwise (CCW) polarized radiation causes the plane of polarization of a linearly polarized wave to rotate when it passes along the magnetic axis of a suitable ferrite: an arbitrary wave can be described either as a combination of two orthogonal linearly polarized waves or as the combination of two contra-rotating circularly polarized beams. The two representations are isomorphic. The conversion matrices between the two are

$$\begin{bmatrix} E_{CW} \\ E_{CCW} \end{bmatrix} = \frac{1}{\sqrt{2}} \begin{bmatrix} 1 & i \\ 1 & -i \end{bmatrix} \begin{bmatrix} E_x \\ E_y \end{bmatrix} , \qquad (4.23)$$

and

$$\begin{bmatrix} E_x \\ E_{y0} \end{bmatrix} = \frac{1}{\sqrt{2}} \begin{bmatrix} 1 & 1 \\ -i & i \end{bmatrix} \begin{bmatrix} E_{CW} \\ E_{CCW} \end{bmatrix} . \qquad (4.24)$$

Consider a linearly polarized wave entering a sample of ferrite, of thickness d, whose refractive indices differ by δ, so that

$$N_{CCW} = N_{CW} + \delta. \qquad (4.25)$$

Then the field when the wave leaves the ferrite will be

$$\begin{bmatrix} Ex \\ Ey \end{bmatrix}_{OUT} = \frac{1}{2} \begin{bmatrix} 1 & 1 \\ -i & +i \end{bmatrix} \begin{bmatrix} e^{ik_o N_{CW} d} & 0 \\ 0 & e^{ik_o (N_{CW}+\delta) d} \end{bmatrix} \begin{bmatrix} 1 & +i \\ 1 & -i \end{bmatrix} \begin{bmatrix} E_x \\ E_y \end{bmatrix}_{IN} \qquad (4.26)$$

Suppose the input is a wave polarized in the X direction. Then the output, ignoring a common factor $E_{xin}\, e^{ik_o N_{CW} d}$, will be

$$E_{xout} = {}^{1}/_{2}\,(1 + e^{ik_o \delta d}) \qquad (4.27a)$$

and

$$E_{yout} = {}^{1}/_{2}\,(-i + i\,e^{ik_o \delta d}) \quad . \qquad (4.27b)$$

Equations [4.27] can be reduced to an amplitude and phase term:

$$E_{xout} = \mathrm{Cos}\,(k_o \delta d/2)\; e^{ik_o \delta d/2} \qquad (4.28a)$$

and

$$E_{yout} = \mathrm{Sin}\,(k_o \delta d/2)\; e^{ik_o \delta d/2} \quad . \qquad (4.28b)$$

By inspection, this is a plane polarized wave with the same amplitude as the initial wave but rotated through an angle

$$\theta = k_o \delta d/2 \quad . \qquad (4.29)$$

Thus by (4.22) the rotation is

$$\delta = \frac{\omega}{2c}\, d\, \epsilon_r^{1/2}\, \frac{\omega_m}{\omega} \qquad (4.30)$$

$$= \frac{d\, \epsilon_r^{1/2}\, \omega_m}{2c} \qquad (4.31)$$

and is independent of frequency. This lack of dependence of rotational angle on frequency is very useful in designing mm wave broadband isolators.

4.3 Previous measurements on Ferrite materials

Rughooputh [4.1] investigated the rotation properties of four ferrite materials. They were of two types: soft ferrite, which requires an

external magnetic field to produce any Faraday rotation, and hard ferrite, which is permanantly magnetised and therefore does not require a driving field. Because of the need to make a compact isolator which could easily fit into a split cube holder (see Chapter 5) the work on hard ferrites was of more interest. Rughooputh tried two such hard ferrites. The first, Feroba 1, was found to be too absorbing at 100 GHz to be of any practical use. The second, Magnadur [4.3], was more interesting. Magnadur is a sintered strontium ferrite having the general formula $SrFe_{13}O_{10}$.

Rughooputh, using small samples of Magnadur (10 mm by 13 mm), showed that Faraday rotation was occuring without major attenuation. However, there was a considerable level of depolarization. (Depolarization is here defined as the ratio of the minimum to maximum power detected as the plane of polarization in which power is measured is rotated.) Also, for unbloomed samples there was a considerable variation in the transmitted power and rotation angle with varying thickness. This indicated that the samples were acting as Fabry-Perot resonators. The resonance was useful in one respect: it was possible for Rughooputh to infer a value for the refractive index of the Magnadur from the periodic behaviour of the transmission when the thickness of the sample was varied. He deduced that the refractive index was equal to 3.88 ± 0.03 at 115 GHz. This value must be taken as an average of CW and CCW wave refractive indices. Indeed, the Faraday rotation effect is due to the fact that they are different, and the difference can be quite significant. In Magnadur at mm wavelengths equation (4.31) indicates that the difference between the two indices is of the order of 0.4 because the measured Faraday rotation is 20 degrees mm^{-1}.

4.4 The design of a small quasi-optical isolator

It was concluded that a working isolator requiring no external magnetic field might be possible using Magnadur ferrite, but to achieve

performance for quasi-optical isolators similar to that obtained by waveguide isolators some form of impedence matching is essential. Depolarization, rather than absorption, is then the major constraint on the performance of the isolator.

Some samples of a Mullard ferrite, Ferroxdure 330 were obtained. This is a strontium ferrite, very similar in composition to Magnadur, and it was possible to obtain 30 mm diameter discs, a surface area some five times that available to Rughooputh. Samples varying in thickness between 2 and 3 mm were bloomed using a loaded-polymer called Flurosint [4.4], which has a refractive index of 1.8. A layer optimised for a wavelength of 2.3 mm (130 GHz) was applied, for which the thickness was $2.3/(4 \times 1.8) = 0.32$ mm. With these the Faraday rotation constant of the permanently magnetised Ferroxdure was measured to be 21 degrees per mm. The methods used to do this were similar to those described in Section 4.5 below for testing the isolators.

The effect of blooming with non-ideal refractive indices and thicknesses was then considered. As an initial step, the reflection and transmission of a plane parallel wave incident normally from air upon an unbloomed layer of refractive index was considered, and the Fresnel relations were used to calculate the reflected and transmitted power, assuming a permeability of unity*. The results are shown in Figs. 4c and 4d, plotted against the beam's single passage phase change. This phase change is given by $2\pi N d/\lambda$ where N is the refractive index and d is the thickness of the sample. It can be seen that the minimum transmission is less that one quarter of the incident power. Although the maximum transmission is unity, this high value occurs only for a narrow band of single passage phase

---

*This assumption is, of course, not strictly true for ferrite materials: indeed their rotation properties are based on the fact that the CW and CCW permeabilities are different. However, at mm wavelengths where $\omega \gg \omega_m$ it is safe to assume that the mean permeability is close to unity.

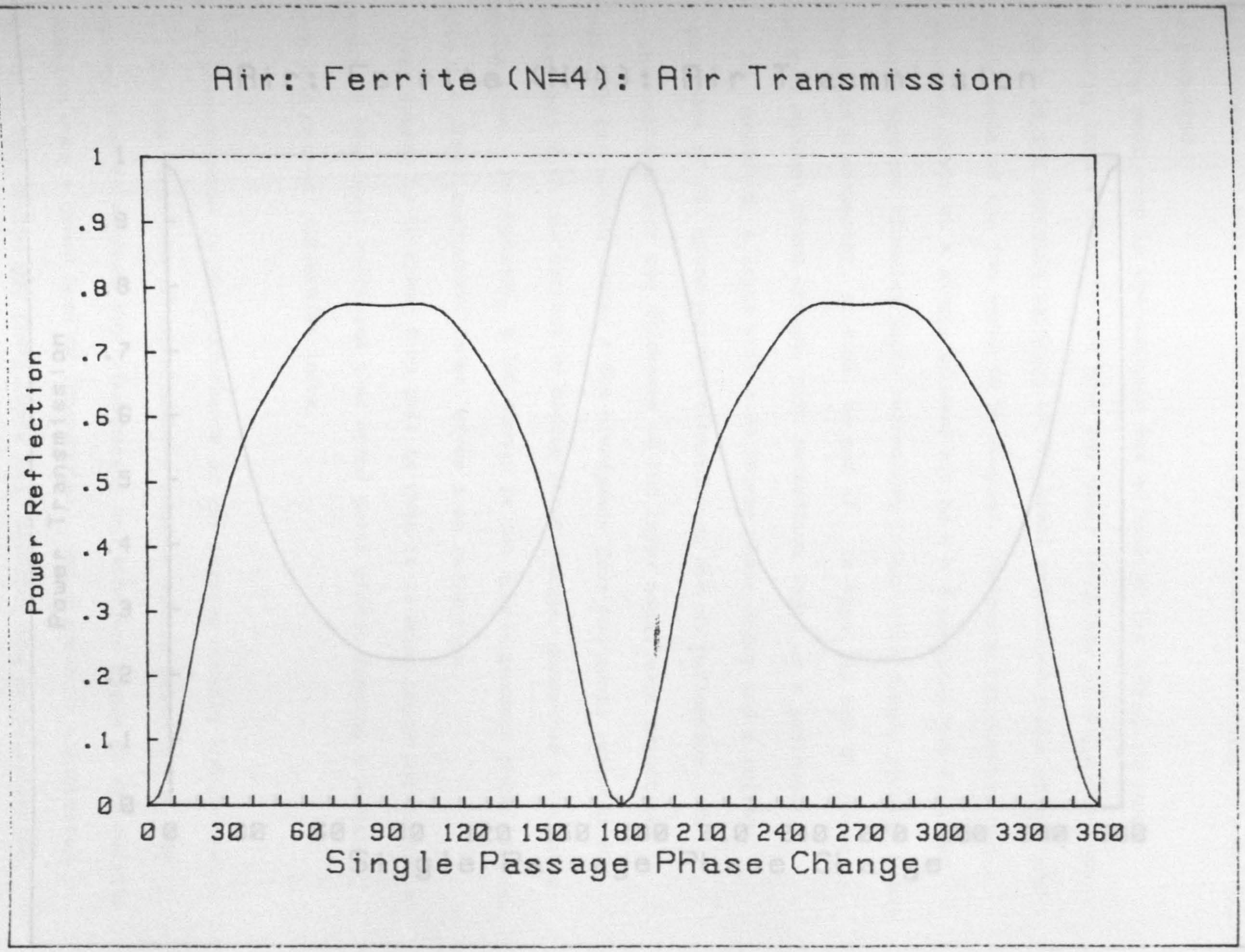
Air: Ferrite (N=4): Air Transmission
Power Reflection
1
.9
.8
.7
.6
.5
.4
.3
.2
.1
0
0
30
60
90
120
150
180
210
240
270
300
330
360
Single Passage Phase Change

Fig. 4c

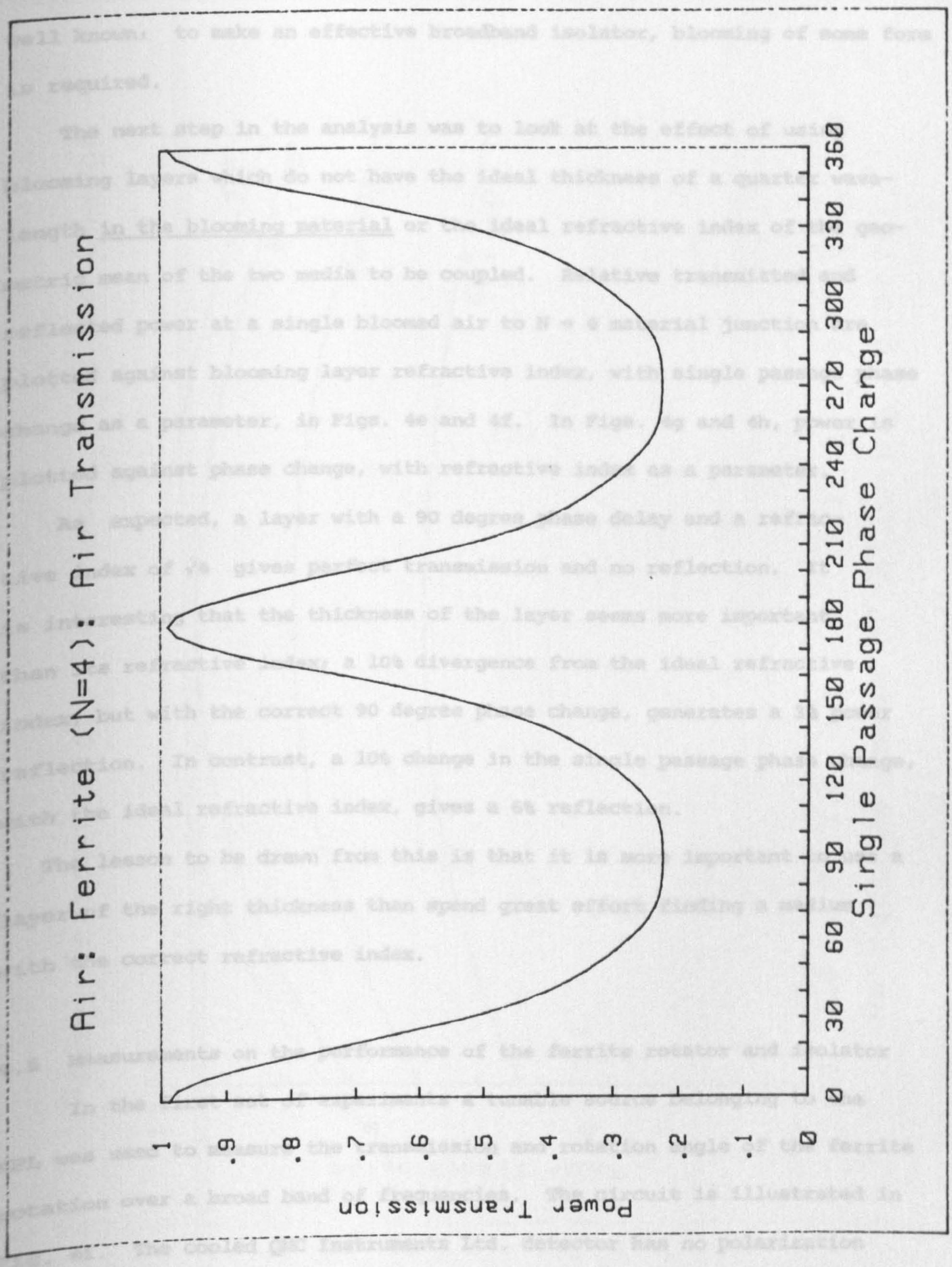
Air Transmission
Air: Ferrite (N=4):
Power Transmission
1
.9
.8
.7
.6
.5
.4
.3
.2
.1
0
0 30 60 90 120 150 180 210 240 270 300 330 360
Single Passage Phase Change

Fig. 4d

changes, which means that there is acceptable transmission only over a very narrow band of frequencies. This simple theoretical study confirms what is well known: to make an effective broadband isolator, blooming of some form is required.

The next step in the analysis was to look at the effect of using blooming layers which do not have the ideal thickness of a quarter wave-length in the blooming material or the ideal refractive index of the geometric mean of the two media to be coupled. Relative transmitted and reflected power at a single bloomed air to N = 4 material junction are plotted against blooming layer refractive index, with single passage phase change as a parameter, in Figs. 4e and 4f. In Figs. 4g and 4h, power is plotted against phase change, with refractive index as a parameter.

As expected, a layer with a 90 degree phase delay and a refractive index of $\sqrt{4}$ gives perfect transmission and no reflection. It is interesting that the thickness of the layer seems more important than its refractive index; a 10% divergence from the ideal refractive index, but with the correct 90 degree phase change, generates a 3% power reflection. In contrast, a 10% change in the single passage phase change, with the ideal refractive index, gives a 6% reflection.

The lesson to be drawn from this is that it is more important to use a layer of the right thickness than spend great effort finding a medium with the correct refractive index.

4.5 Measurements on the performance of the ferrite rotator and isolator

In the first set of experiments a tunable source belonging to the NPL was used to measure the transmission and rotation angle of the ferrite rotation over a broad band of frequencies. The circuit is illustrated in Fig. 4i. The cooled QMC Instruments Ltd. detector has no polarization sensitivity. After initial tests, Eccosorb was added in the positions indicated to reduce standing wave reflections. Unfortunately the 20 dB

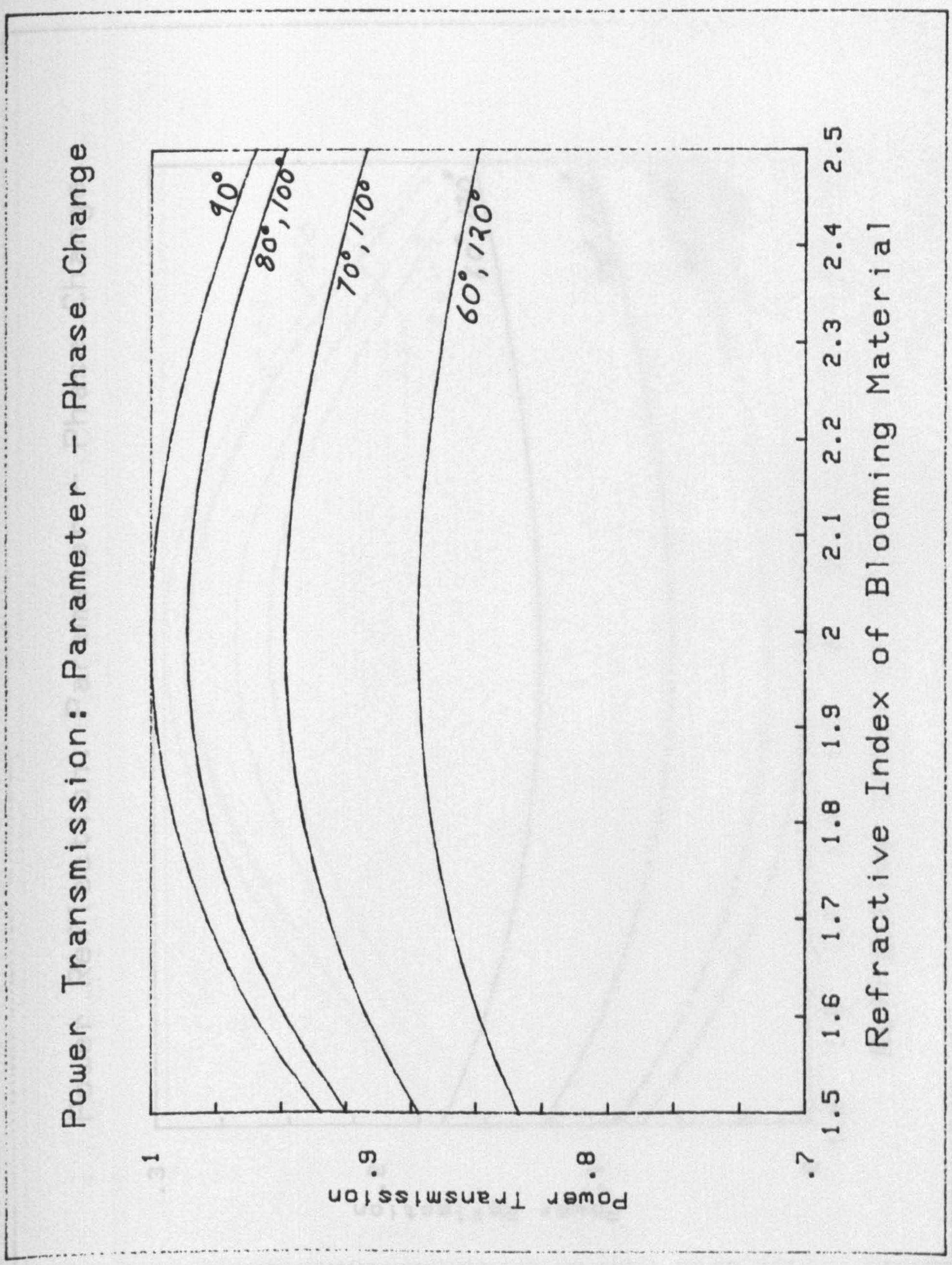
Power Transmission: Parameter - Phase Change
90°
80°, 100°
70°, 110°
60°, 120°
Power Transmission
1
.9
.8
.7
1.5
1.6
1.7
1.8
1.9
2
Refractive Index of Blooming Material
2.1
2.2
2.3
2.4
2.5

Fig. 4e

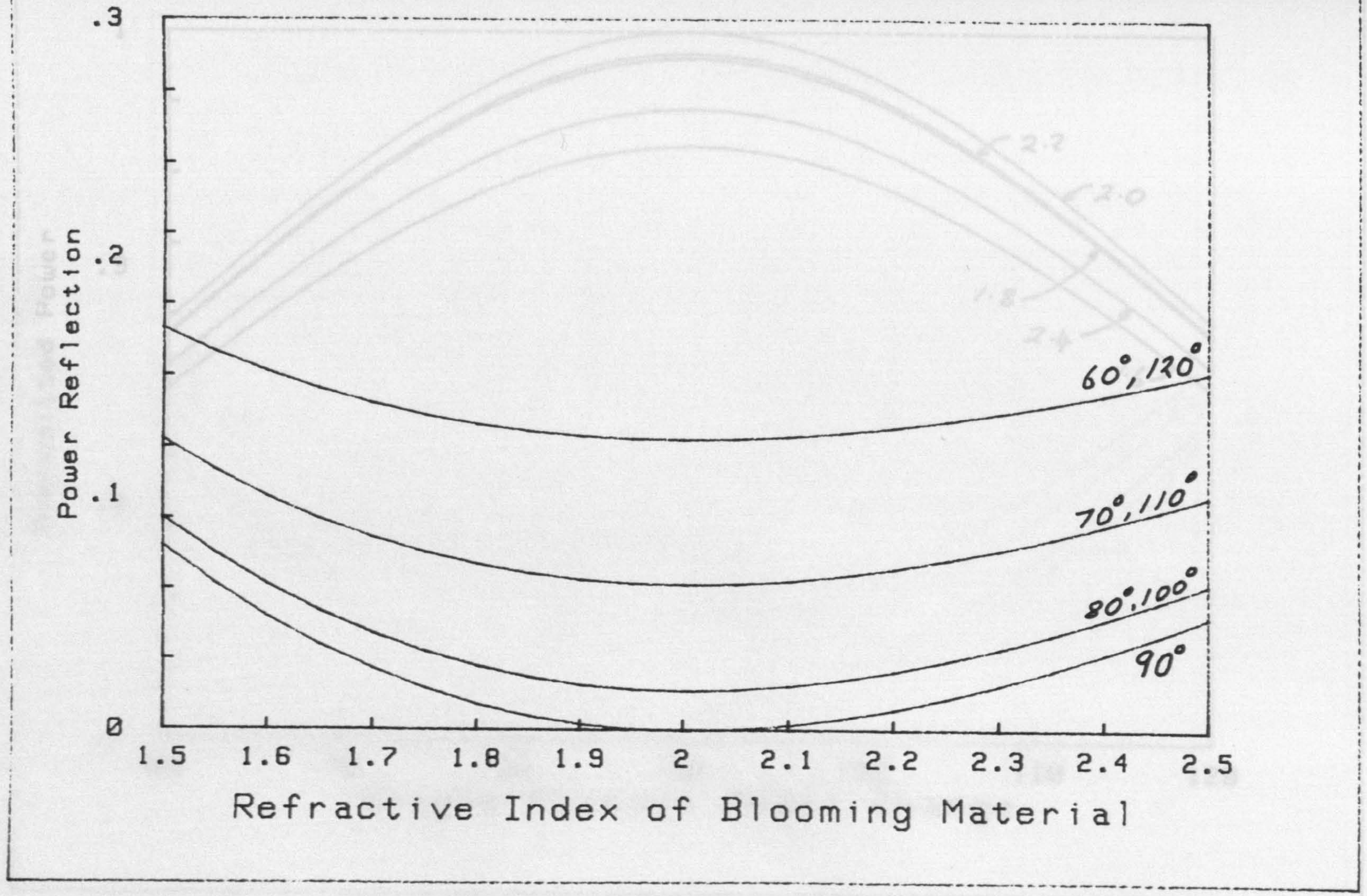
Power Reflection: Parameter - Phase Change
Power Reflection
.3
.2
.1
0
1.5
1.6
1.7
1.8
1.9
2
2.1
2.2
2.3
2.4
2.5
Refractive Index of Blooming Material
60°,120°
70°,110°
80°,100°
90°

Fig. 4f

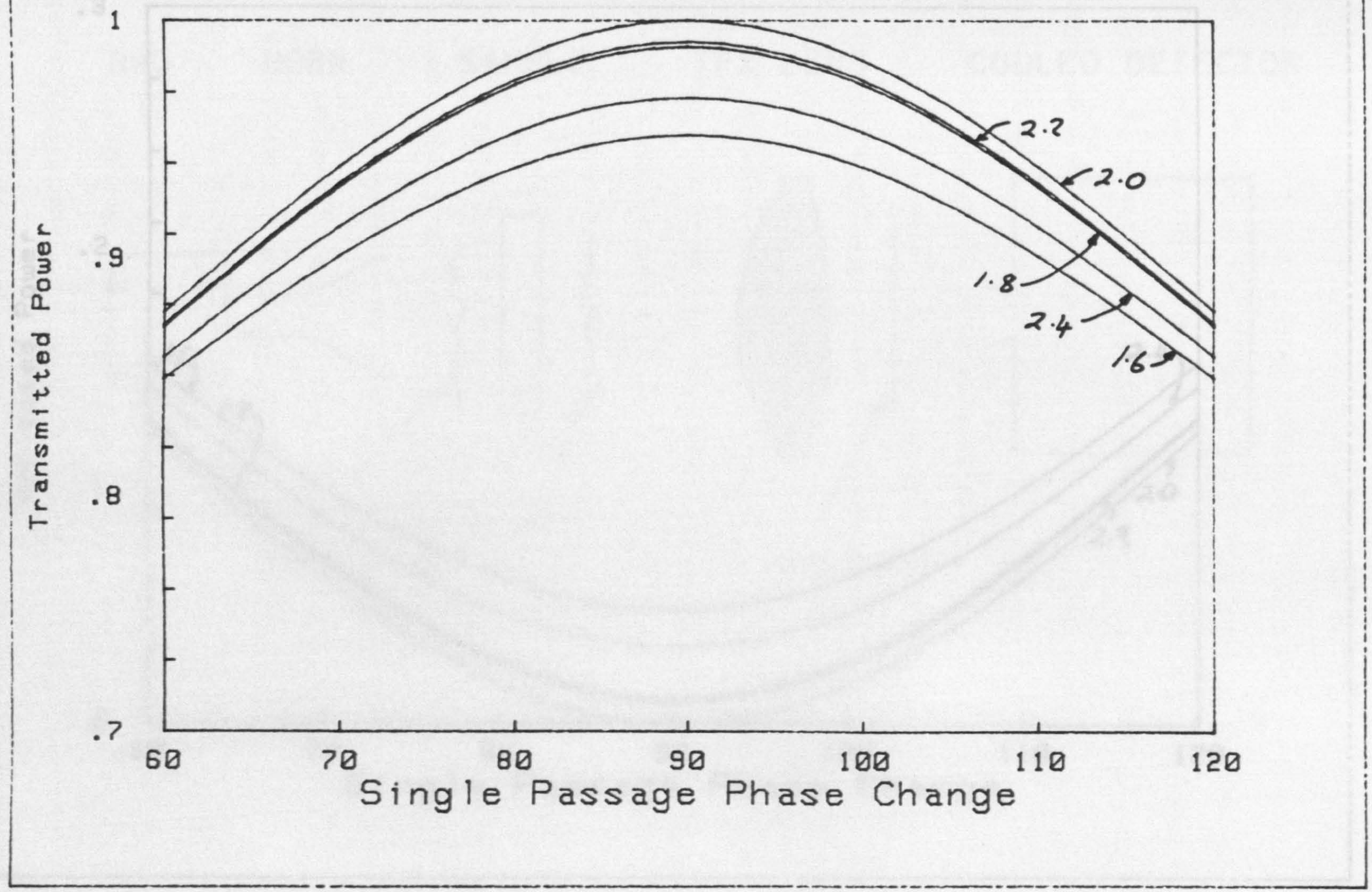
Power Transmission: Parameter - Refractive Index
Transmitted Power
1
.9
.8
.7
2.2
2.0
1.8
2.4
1.6
60
70
80
90
100
110
120
Single Passage Phase Change

Fig. 4g

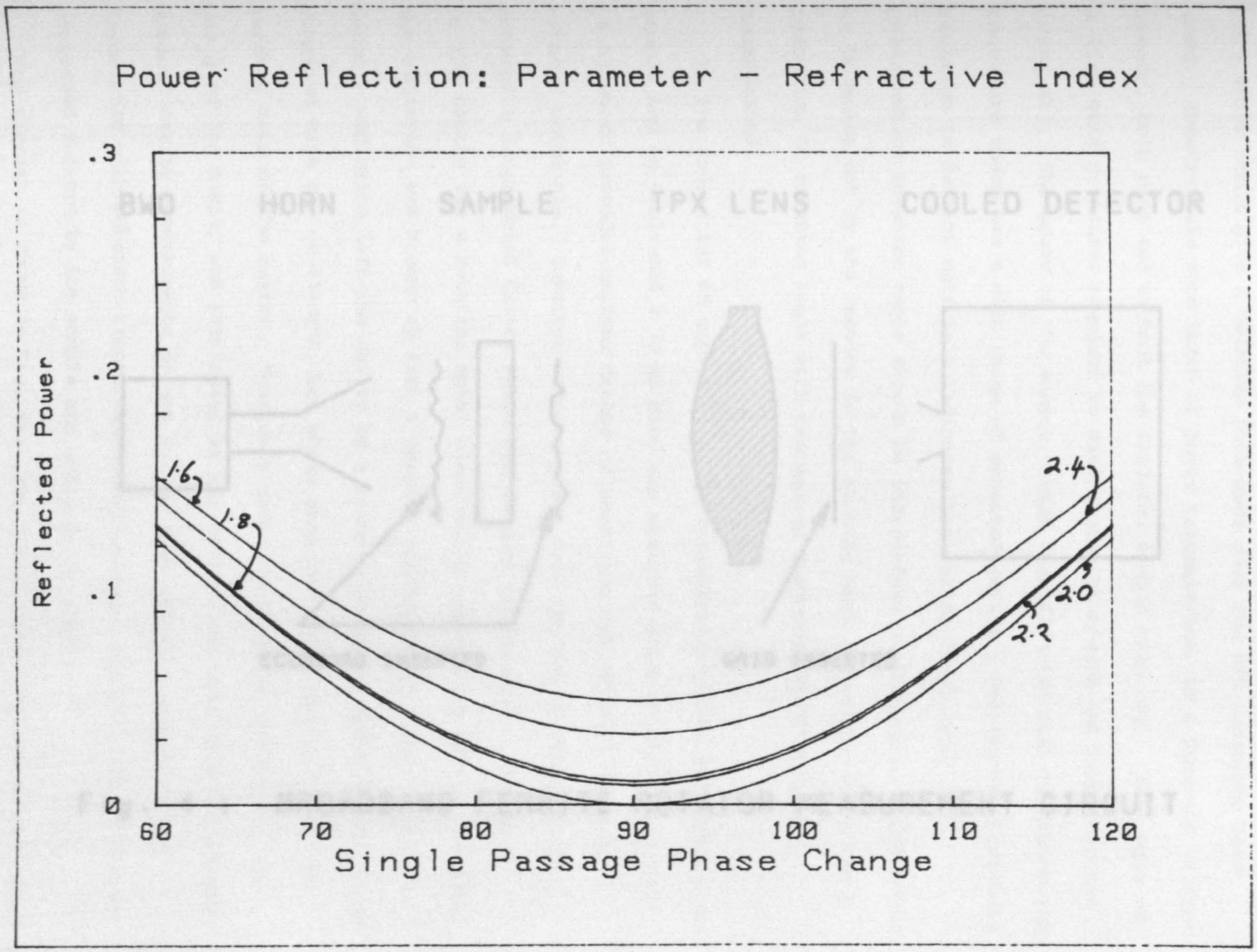
Power Reflection: Parameter - Refractive Index
Reflected Power
.3
.2
.1
0
1.6
1.8
2.4
2.0
2.2
60
70
80
90
100
110
120
Single Passage Phase Change

Fig. 4h

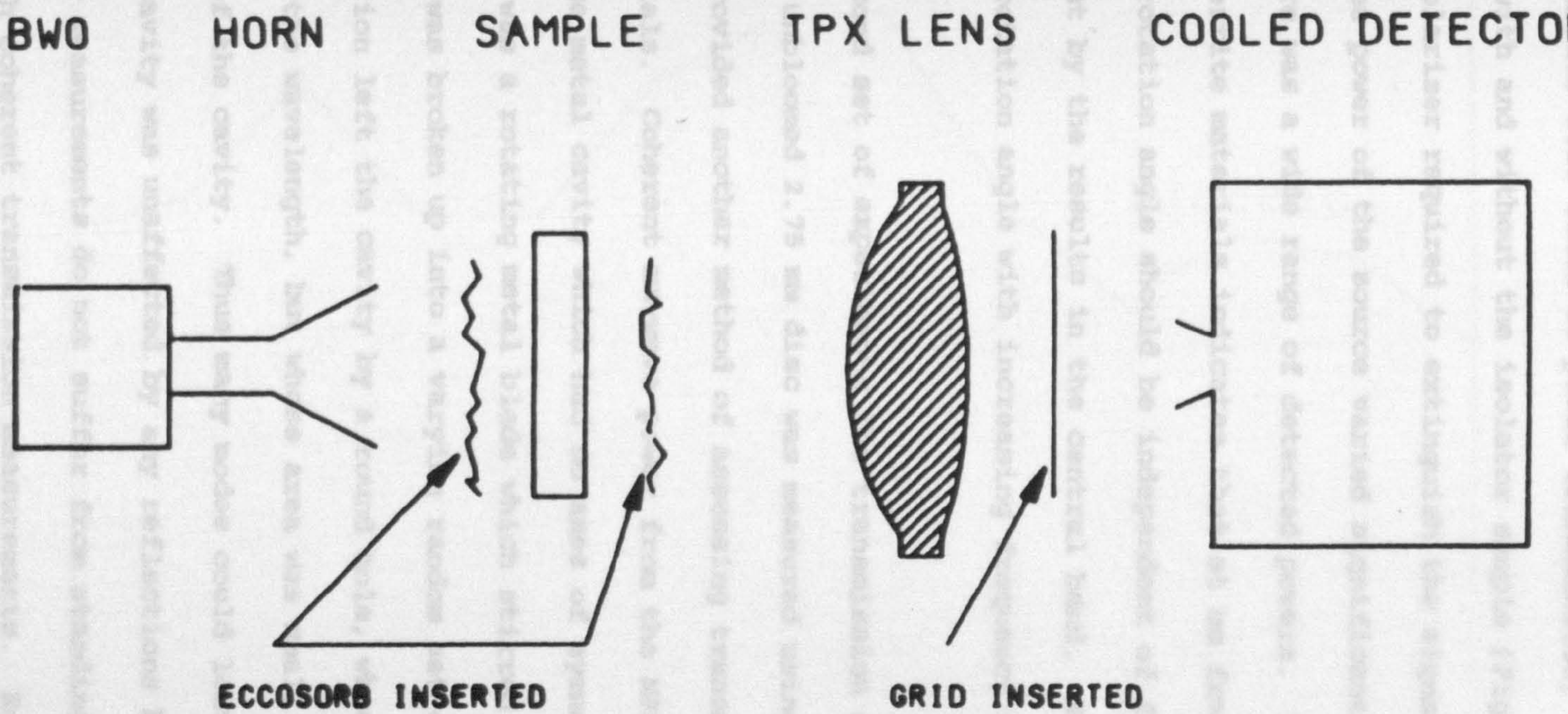

Fig. 4 | BROADBAND FERRITE ROTATOR MEASUREMENT CIRCUIT

gain rectangular feed horn did not produce a fundamental Gaussian beam-mode; it would be very difficult (if not impossible) to design a corrugated horn which would give a Gaussian beam-mode over the 65% frequency band used. Measurements were taken of power transmission, as a function of frequency, both with and without the isolator sample (Fig. 4j). The angle of a wire grid polarizer required to extinguish the signal was also recorded (Fig. 4k). The power of the source varied significantly with frequency and therefore there was a wide range of detected powers. The theory of Faraday rotation in ferrite materials indicates that at mm frequencies the polarization rotation angle should be independent of frequency. This seems to be borne out by the results in the central band. However, there was a reduction in rotation angle with increasing frequency which remains unexplained.

In the second set of experiments the transmission of the bloomed 2.1 mm sample and an unbloomed 2.75 mm disc was measured using an untuned cavity [4.5] which provided another method of assessing transmission through rotator materials. Coherent mm-wave power from the NPL tunable source entered a large metal cavity which had no axes of symmetry. Enclosed in the cavity was a rotating metal blade which stirred the cavity, so that the radiation was broken up into a varying random set of higher order modes. Radiation left the cavity by a round hole, whose diameter was large compared with the wavelength, but whose area was small compared with the surface area of the cavity. Thus many modes could leave the cavity, but the Q of the cavity was unaffected by any reflections back into the cavity. Untuned cavity measurements do not suffer from standing wave problems associated with coherent transmission measurements. However, power can be scattered forward by the sample and still be detected.

The circuit is shown in Fig. 4l. The source feed horn was positioned inside the cavity, and the QMC Instruments Ltd. detector placed about 50 mm from the circular cavity output aperture. Measurements were taken by

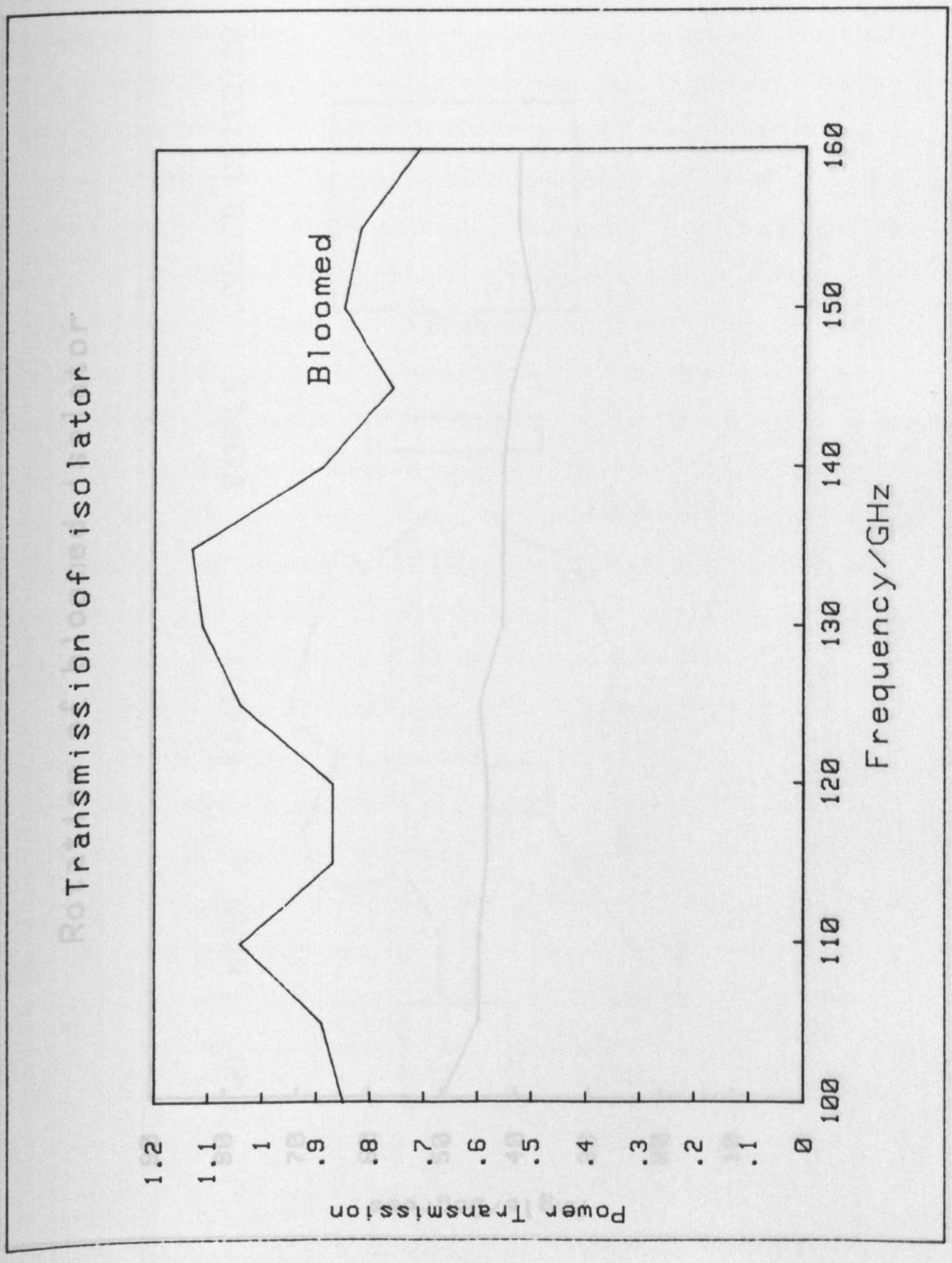
Transmission of isolator
Bloomed
Power Transmission
1.2
1.1
1
.9
.8
.7
.6
.5
.4
.3
.2
.1
0
100
110
120
130
140
150
160
Frequency/GHz

Fig. 4j

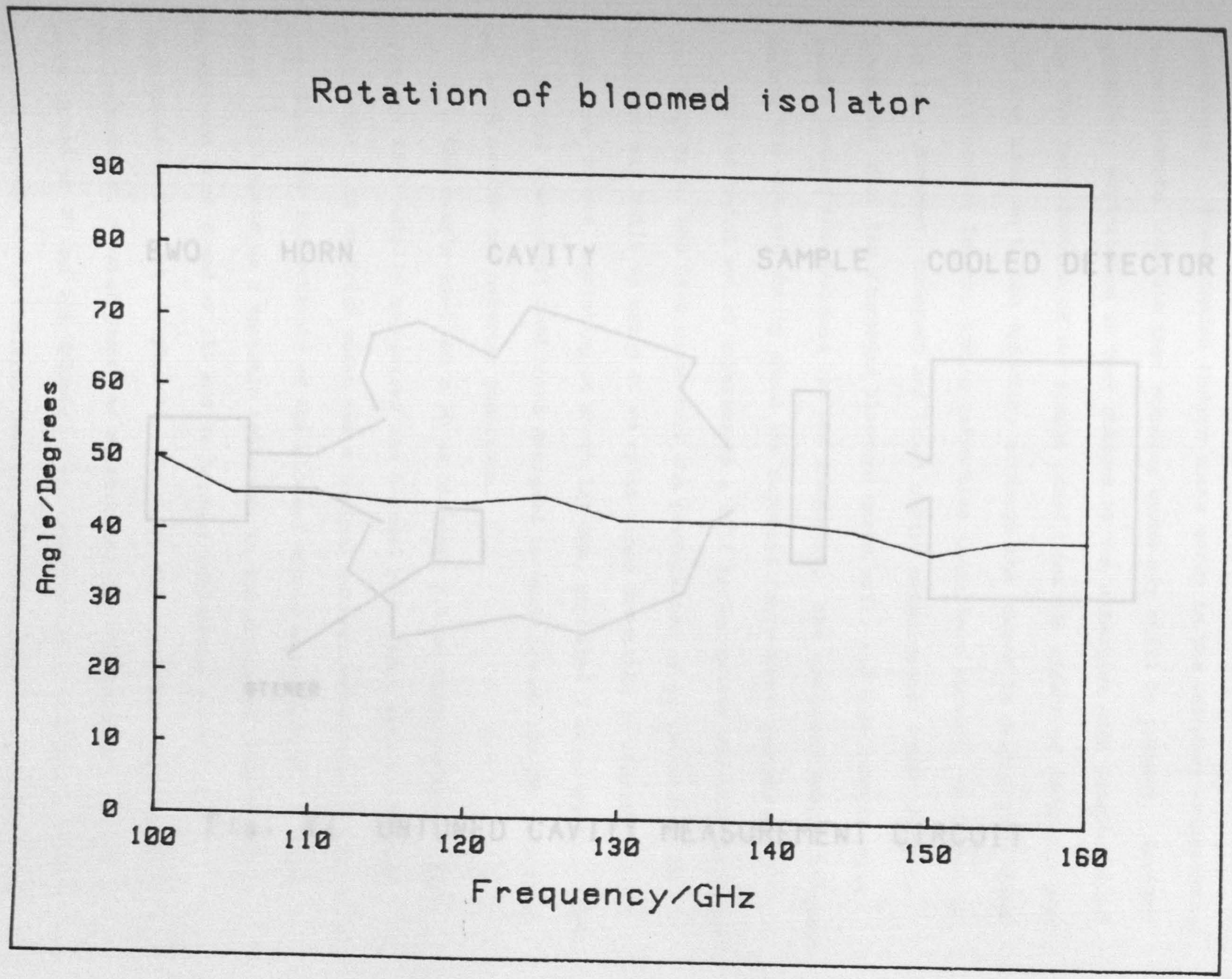
Rotation of bloomed isolator
90
80
70
60
50
40
30
20
10
0
Angle/Degrees
100
110
120
130
140
150
160
Frequency/GHz

Fig. 4k

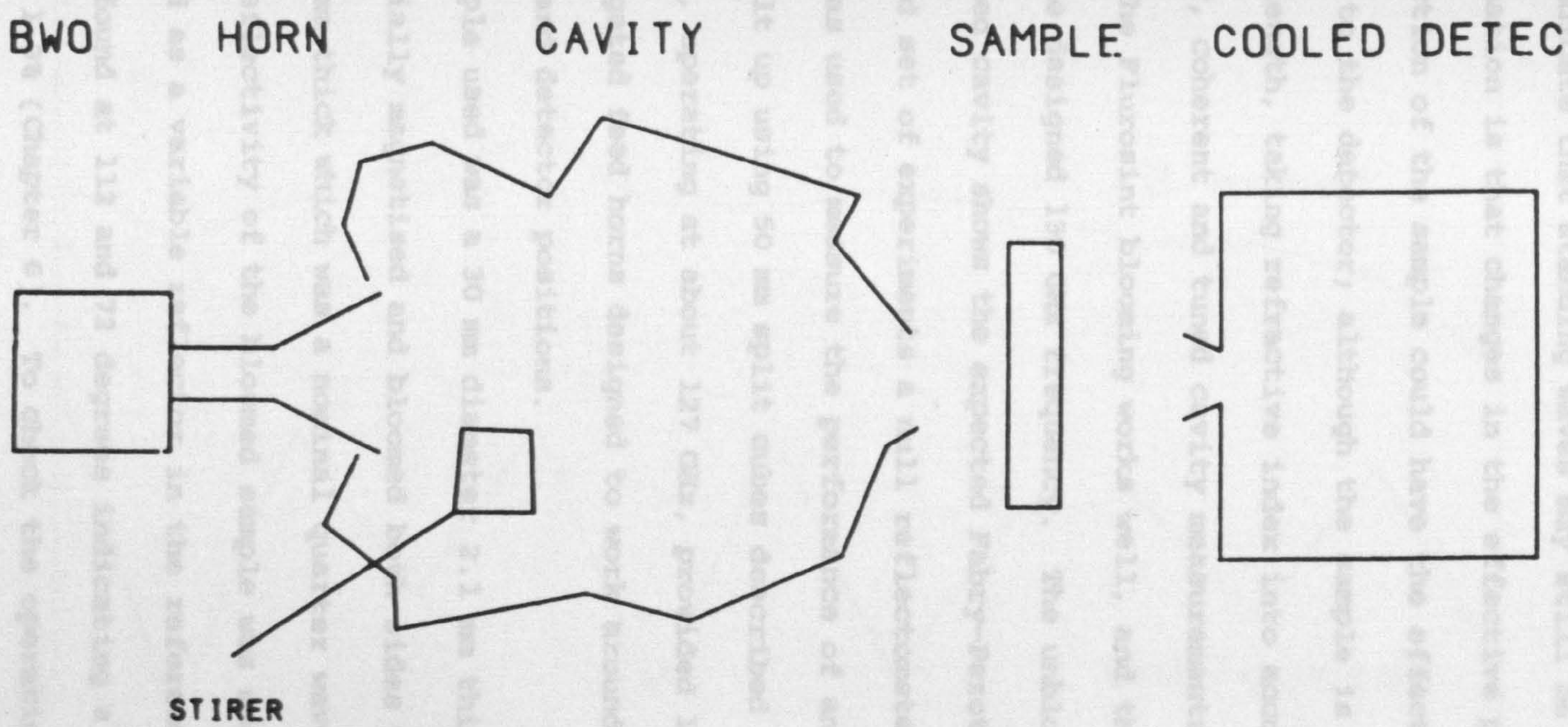

Fig. 41 UNTUNED CAVITY MEASUREMENT CIRCUIT

inserting the samples between the cavity aperture and detector, close to the cavity wall, and are plotted in Fig. 4m. The samples covered the aperture. Transmission factors above unity in the coherent transmission measurements indicate that standing waves may still be present. Another possible explanation is that changes in the effective path length caused by the introduction of the sample could have the effect of focussing more of the beam on to the detector; although the sample is only 2.1 mm thick its effective length, taking refractive index into account, is closer to 10 mm. However, coherent and tuned cavity measurements taken together indicate that the Flurosint blooming works well, and that transmission peaks around the designed 130 GHz frequency. The unbloomed sample measured using the untuned cavity shows the expected Fabry-Perot resonance.

In the third set of experiments a null reflectometer circuit, described in Chapter 6, was used to measure the performance of an isolator. The circuit was built up using 50 mm split cubes described in Chapter 5. A klystron source, operating at about 127 GHz, provided 1 mW of power. Waveguide-fed corrugated feed horns designed to work around 130 GHz were used at both source and detector positions.

The sample used was a 30 mm diameter 2.1 mm thick sample of Ferroxdure 330, axially magnetised and bloomed both sides with a layer of Flurosint 0.32 mm thick which was a nominal quarter wavelength thickness at 130 GHz. The reflectivity of the bloomed sample was measured. A rotating wire grid acted as a variable reflector in the reference channel. Null positions were found at 112 and 72 degrees indicating a power reflectivity of 1.3% (Chapter 6). To check the operation of the null reflectometer, a metal plate was substituted for the isolator. Nulls were found at 20 and 208 degrees. This converts to a reflection coefficient of 99%, which confirms that the reflectometer was operating satisfactorily.

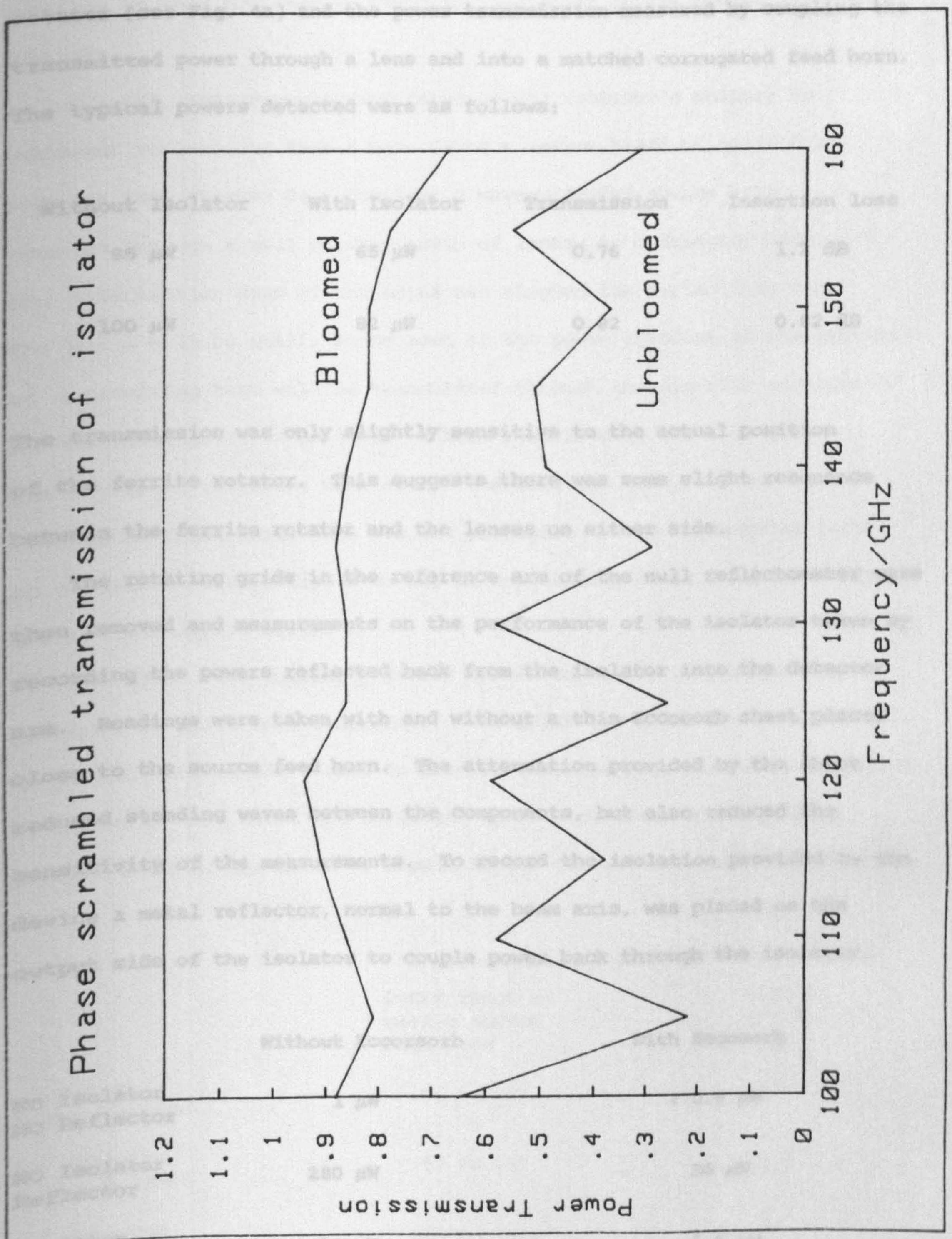
Phase scrambled transmission of isolator
Bloomed
Unbloomed
160
150
140
130
120
110
100
Frequency/GHz
1.2
1.1
1
.9
.8
.7
.6
.5
.4
.3
.2
.1
0
Power Transmission

Fig. 4m

Correctly angled grids were then added on both sides of the ferrite rotator (see Fig. 4a) and the power transmission measured by coupling the transmitted power through a lens and into a matched corrugated feed horn. The typical powers detected were as follows:

Without Isolator	With Isolator	Transmission	Insertion loss
85 μW	65 μW	0.76	1.2 dB
100 μW	82 μW	0.82	0.82 dB

The transmission was only slightly sensitive to the actual position of the ferrite rotator. This suggests there was some slight resonance between the ferrite rotator and the lenses on either side.

The rotating grids in the reference arm of the null reflectometer were then removed and measurements on the performance of the isolator taken by recording the powers reflected back from the isolator into the detector arm. Readings were taken with and without a thin Eccosorb sheet placed close to the source feed horn. The attenuation provided by the sheet reduced standing waves between the components, but also reduced the sensitivity of the measurements. To record the isolation provided by the device a metal reflector, normal to the beam axis, was placed on the output side of the isolator to couple power back through the isolator.

	Without Eccorsorb	With Eccosorb
NO Isolator NO Reflector	1 μW	< 0.5 μW
NO Isolator Reflector	280 μW	30 μW
Isolator NO Reflector	10 μW	1.5 μW
Isolator Reflector	15 μW	2 μW
Isolation	17.5 dB	About 17 dB

This performance, an insertion loss of 1 dB and isolation of 17 dB, is similar to that achieved in waveguide isolators in the region just below 100 GHz.

Finally, measurements were taken of the isolator's ability to suppress reflections from a horn using a system based on split-cube modules (see Chapter 5). Consider a waveguide-fed source horn coupled through a well matched train of lenses to a detector horn. If the polarization axes of the horns are aligned the reflections from the horns will be small, since most of the power incident at the aperture of a receiving horn will be transmitted through the circular corrugated/ smooth rectangular transition. A beam polarized in the orthogonal plane will be reflected back out of the detector horn, because the orthogonal fundamental mode can not propagate in the rectangular guide. An experiment was performed to see if an isolator could reduce the ripple between misaligned horns.

Two horns were coupled together by two correctly positioned lenses, using 50 mm split cube components. Two grids and a ferrite rotator could be placed between the lenses to form an isolator [see Fig. 4n]. One horn could be rotated about its boresight axis to generate misalignment. Measurements of the level of ripple in the circuit were made at 127 GHz:

Ripple measurements at 127 GHz

	Power range on moving source horn / mW	Ripple +/- %
Isolator Horns Aligned	.91 to .97	1.5
NO Isolator Horns Aligned	.82 to .87	2.5
NO isolator Horns misaligned	.010 to .028	50
Isolator Horns misaligned	.225 to .275	10

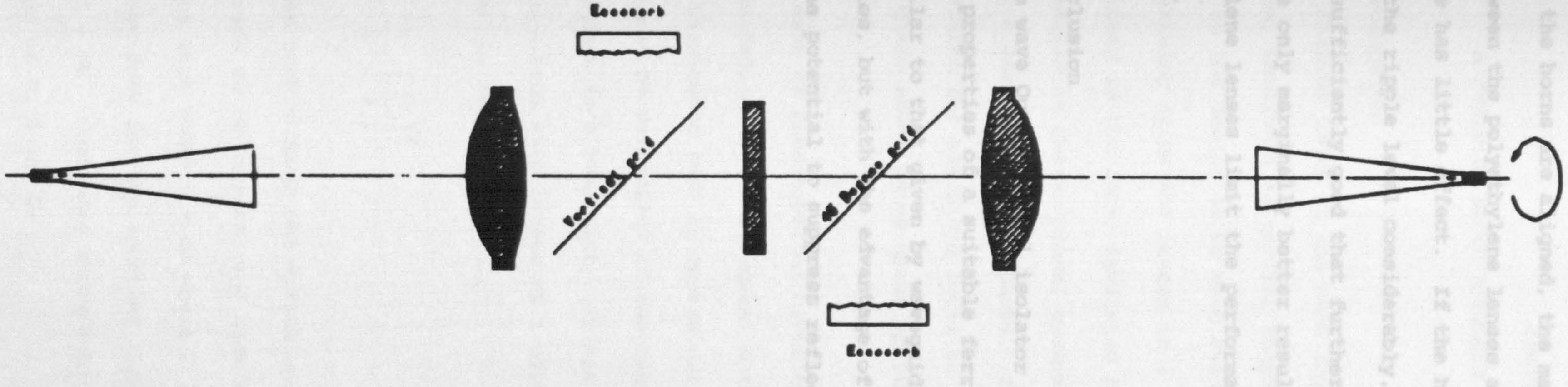

Fig. 4 ת ISOLATOR TEST CIRCUIT

When the horns are aligned, the main cause of standing waves is reflection between the polyethylene lenses and the horns. The isolator therefore has little effect. If the horns are misaligned, the isolator reduces the ripple level considerably. The quasi-optical isolator is already sufficiently good that further improvements in its performance will give only marginally better results, because the reflections from polyethylene lenses limit the performance of systems incorporating an isolator.

4.6 Conclusion

A mm wave Quasi-optical isolator was constructed using the Faraday rotation properties of a suitable ferrite. This proved to have a performance similar to that given by waveguide isolators working at lower frequencies, but with the advantage of operating over a wider bandwidth and having the potential to suppress reflections between misaligned feed horns.

CHAPTER 5

A BUILDING BLOCK APPROACH TO QUASI-OPTICAL CIRCUITS

5.1 Introduction

This chapter looks at the need for a building block that would realise the notion, mentioned in earlier chapters, of a quasi-optical circuit approach to the design of mm wave systems. The need to accurately position wire polarizing grids and lenses in a correct orientation is discussed. Also reviewed is the idea, developed by Martin [1.6], that the spacing between lenses in quasi-optical systems should be at a Gaussian mode-beam's maximum throw distance. This approach gives the most compact size of system for any given level of performance. A breadboard that realises these needs using brass split half cubes is outlined.

5.2 The size of quasi-optical circuits

It is desirable to make quasi-optical circuits as compact as possible. Gaussian beam-modes tend to spread out as they propagate, but this spreading can be controlled if the beams are picked up by lenses and refocused down to a beamwaist. It has been shown in Chapter 1 (1.12) that to contain a beam with lenses of a diameter D, the maximum distance between the lenses, L, is given by

$$L = \frac{\pi}{\lambda}\left[\frac{D}{3}\right]^2 . \qquad (5.1)$$

Now a given path through the system must accommodate a certain number, N say, of grids or reflectors, and each of these can be seen to take up a cubic space with sides U = CD where C is a constant greater than unity which allows room for the mounting frame. Thus the path length L is also given by L = NU. Combining these equations we get at minimum system size the values of U, D and L:

$$\frac{U_{min}}{\lambda} = \left[\frac{9\,C^2}{\pi}\right] N \quad . \tag{5.2}$$

$$\frac{L_{min}}{\lambda} = \left[\frac{9\,C^2}{\pi}\right] N^2 \quad , \tag{5.3}$$

and

$$\frac{D_{min}}{\lambda} = \left[\frac{9\,C}{\pi}\right] N \quad . \tag{5.4}$$

The 115 GHz receiver described in Chapter 8 was made using this maximum throw approach. To use common input and output lenses in the diplexers requires that N=4. Thus, taking C = $^3/2$, we have $U_{min}/\lambda \simeq 25.8$, so that at the LO frequency (110 GHz) U_{min} = 70.3 mm. A 70 mm cube size was therefore adopted.

5.3 The design of Split cubes

The quasi-optical components describe in the previous chapters must be held accurately in their correct positions to generate a working system, but should be easily movable to other suitable positions. The maxiumum throw approach suggests a configuration of cubic modules with grids or reflectors set in diagonal faces, lenses in cube faces, and isolators and feed horns along cube axes. A convenient modular approach to holding all of the components is based on a split cube mounted on a base plate. The half cubes are constructed by bisecting a solid cube along a diagonal and boring out a hole perpendicular to the centres of the two square faces. As seen from the square faces, the resulting cylindrical holes have circular cross sections equal to a lens diameter, while in the diagonal face they coincide in an elliptical aperture. Lenses are set in the cube face by counterboring a recess to a depth of half the thickness of the mounting flange of the lens, and a lens retaining

ring is then screwed to the cube to hold the lens in place. A rectangular recess around the elliptical aperture in the diagonal face is machined to hold wire grid frames. Four small clamps hold a grid or a reflector in place (Fig. 5a).

Ferrite isolators, held in thin walled brass tube and retained on both sides by retaining rings, are positioned in the cylinderical holes along which the beams pass.

The machining of the external faces and recesses of the half-cubes should be to a 10 μm tolerance. (For a discussion of the effects of misalignment in quasi-optical systems see [1.6].) Fixing and dowel holes are jig-bored into the top and bottom triangular faces of each half cube to correspond to those in an element of the matrix in the base-plate (Fig. 5b).

Waveguide-fed horns are mounted in special rectangular cubes with the standard pattern of fixing and dowel holes in their bottom faces. The upper half of the special cubes is lifted to allow the cylindrical outside form of the feed horn to be inserted, and then screwed down to secure the horn. A small dowel pin protruding from the cube inserts into channels running along the axis of the feed horn at specific angles to the waveguide in the horn. This allows the horn to be orientated at the correct angle to insure that the required polarized Gaussian beam-mode is generated by the horn.

The baseplate is made from 20 mm thick Dural, which is rigid, stable and easy to machine. A matrix of fixing and dowel holes is drilled into it to retain the half cubes. The matrix is designed to ensure that lenses are positioned at the correct maximum throw distances.

DO NOT SCALE

4 HOLES (2 IN EACH FACE)
TAP M2.5 x 6.0/.236" DEEP.

4 HOLES (2 IN EACH END)
5.000/.1969" ϕ ('S' FIT FOR DOWELS) x 7.5/.295" DEEP.
NOTE: DO NOT BREAK THRU'.

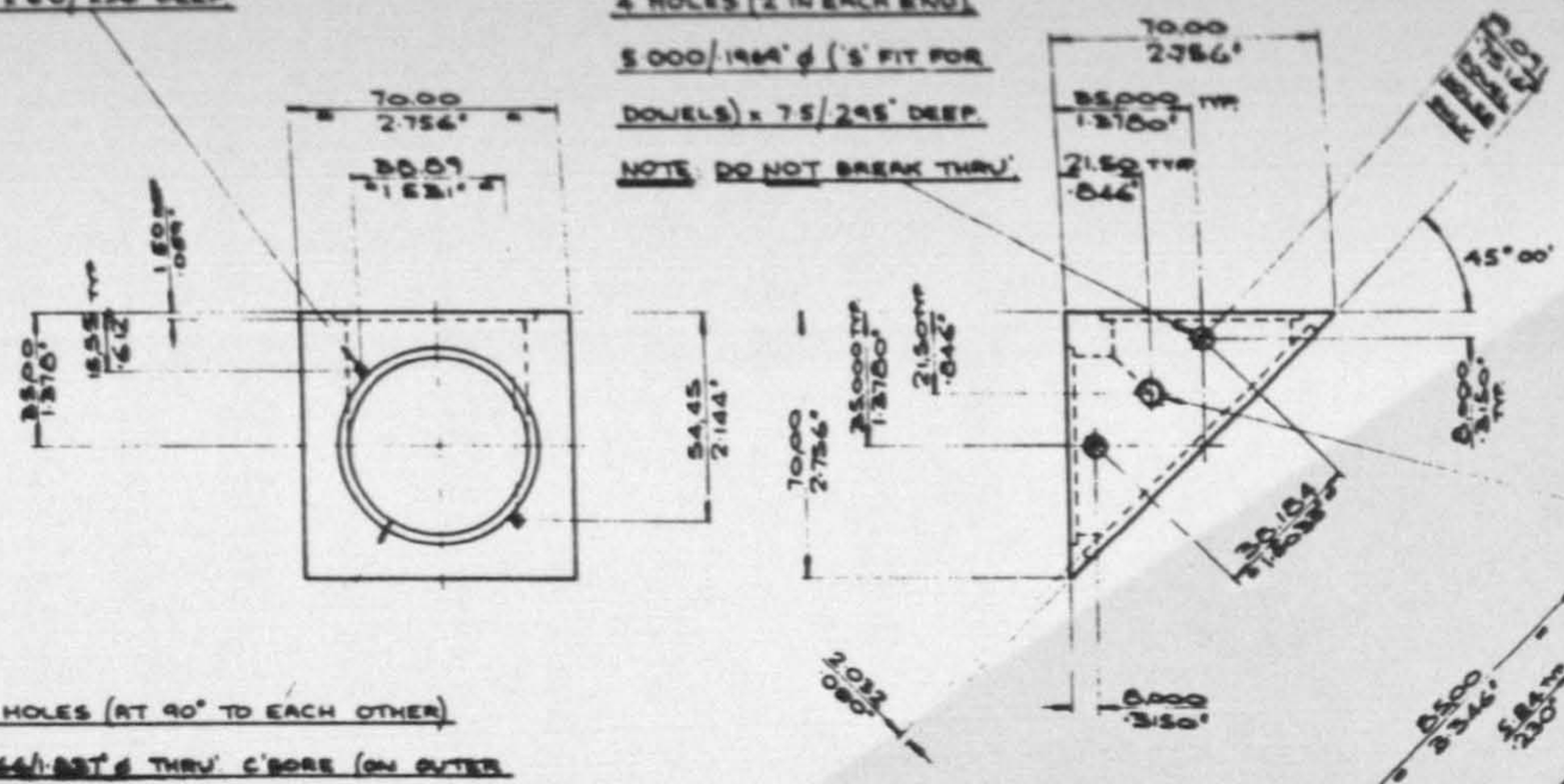

2 HOLES (AT 90° TO EACH OTHER)
4.646/1.887" ϕ THRU' C'BORE (ON OUTER FACES) 5.000/1.969" ϕ (DEP) x 1.50/.059" DEEP.

2 HOLES (1 IN EACH END)
TAP M6 x 9.0/.354" DEEP.
NOTE: DO NOT BREAK THRU'.

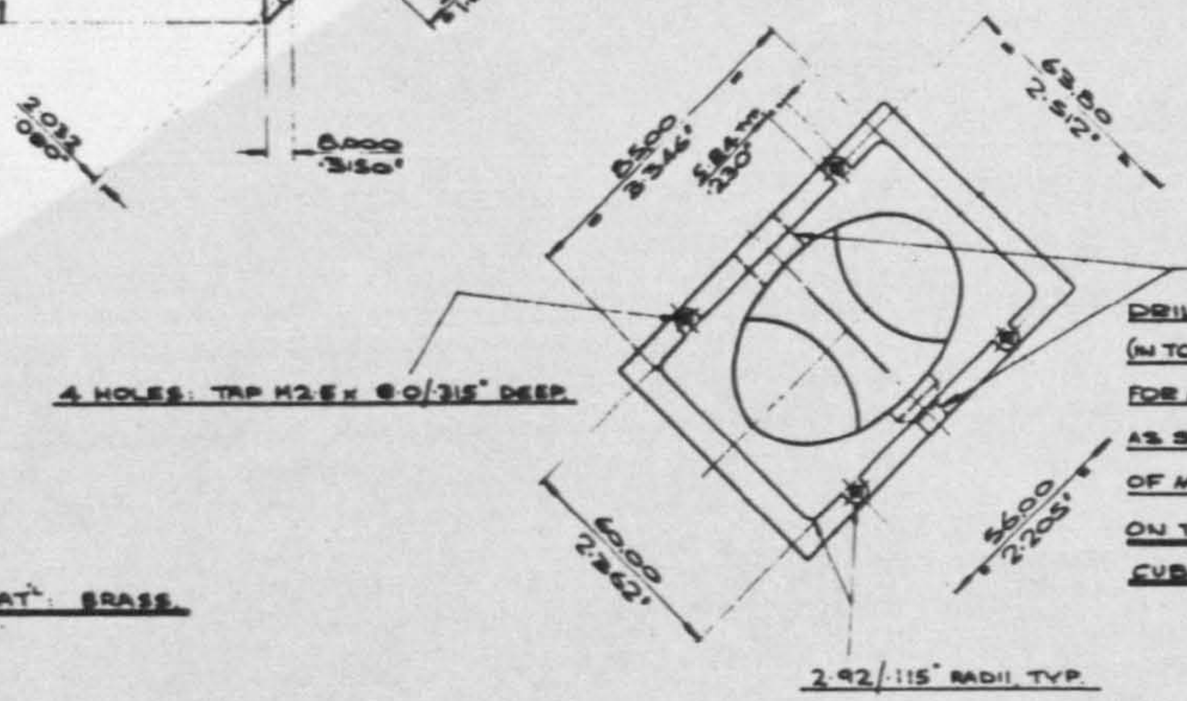

4 HOLES: TAP M2.5 x 8.0/.315" DEEP.

* NOTE!
DRILL 1 HOLE 1.35 DIA (IN TOP) & DRILL & C'SK FOR M6 SCREW (BTM) AS SHOWN IN PLACE OF M6 TAPPED HOLE ON TOP MOUNTING CUBES ONLY.

2.92/.115" RADII TYP.

(1) 70% HALF CUBE LENS AND GRID HOLDER. MAT'L: BRASS.

2 HOLES: 2.000/.0787" ϕ THRU'. FIT 2 HRD STL. PINS. PUSH FIT. 3.7/.146" LONG (MAX).

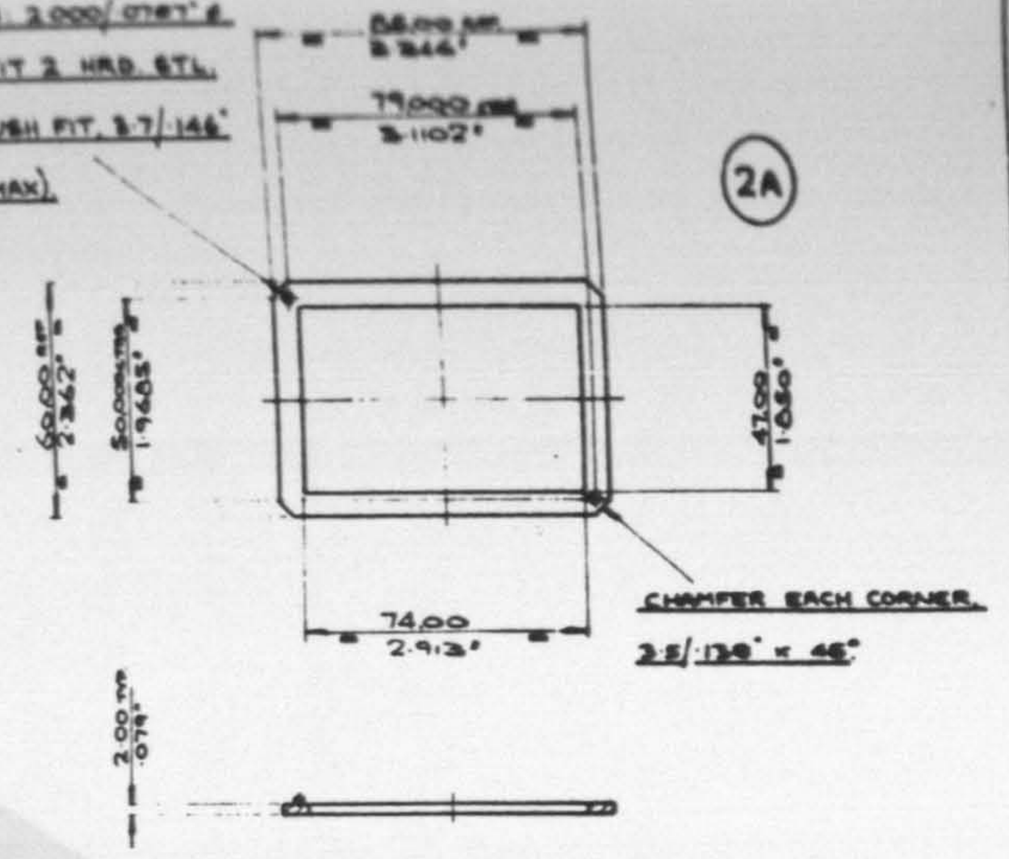

(2A)

CHAMFER EACH CORNER.
2.5/.138" x 45°

2 HOLES: 2.000/.0787" ϕ THRU'. SLIDE FIT.

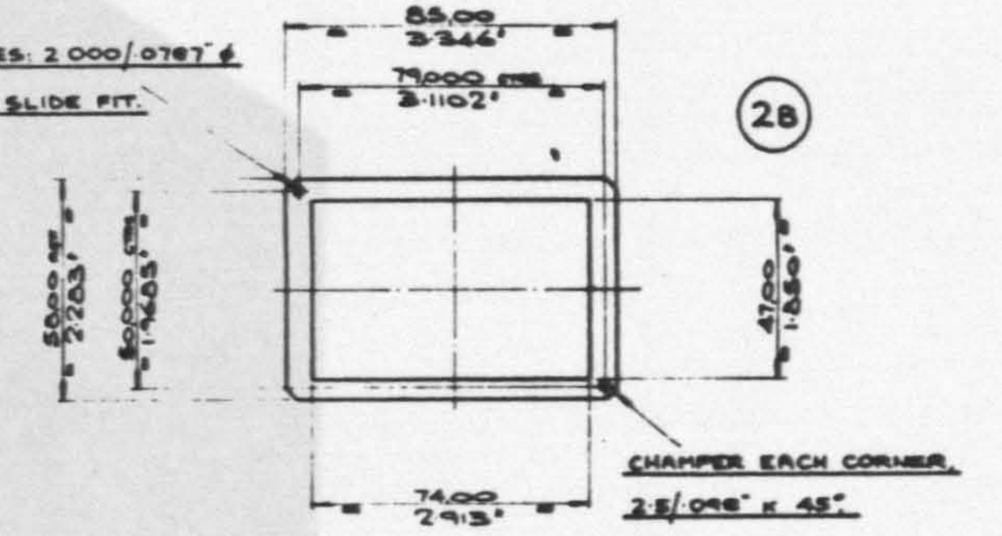

(2B)

CHAMFER EACH CORNER.
2.5/.098" x 45°

(2A) (2B) 'GRID FRAMES' 1 OFF OF EACH PER GRID.
MAT'L: STAINLESS STEEL.

2 HOLES: 2.7/.106" ϕ THRU' C'SK TO SUIT M2.5 C'SK HD SOCKET SCREWS.

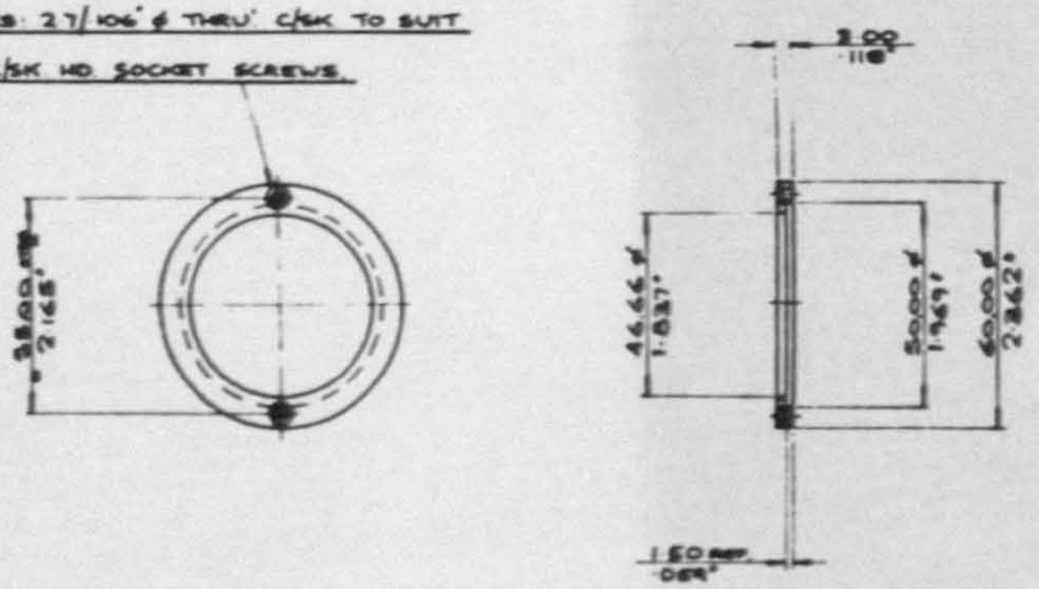

(3) 'LENS RETAINING RING' MAT'L: BRASS. 2 REQ'D FOR EACH HALF CUBE.

C'SK TO SUIT M2.5 C'SK. HD. SOCKET SCREWS

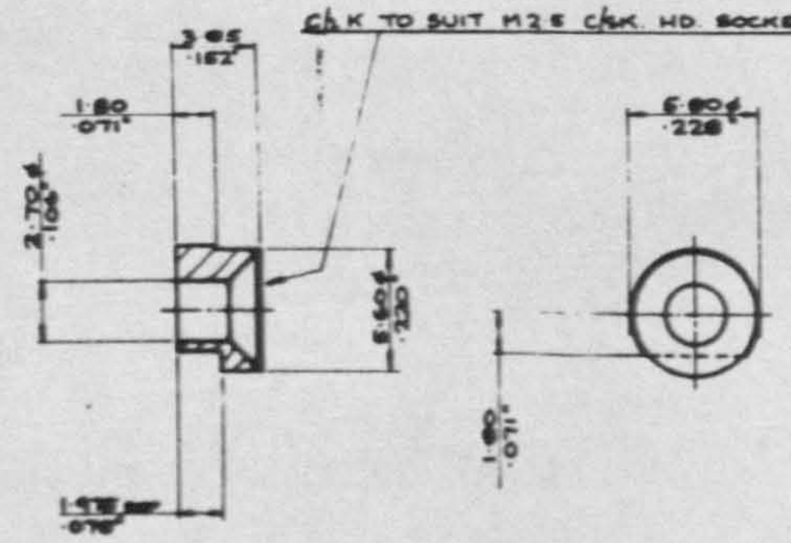

SCALE: 5 TO 1.

(4) 'GRID CLAMP' MAT'L: BRASS. 4 REQ'D FOR EACH HALF CUBE.

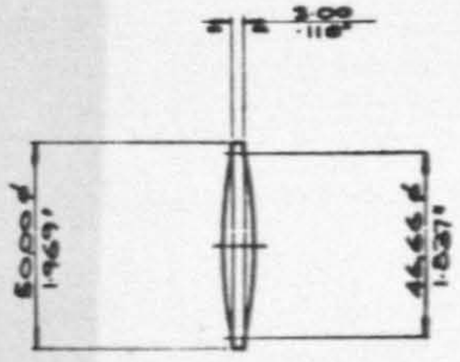

(5) 'LENS'.
TO BE SUPPLIED.

CUSTOMER: Q.M.C.	
TITLE: 11.5 GHz RECEIVER 70% SPLIT CUBE ASSY.	1/1

Fig. 5a

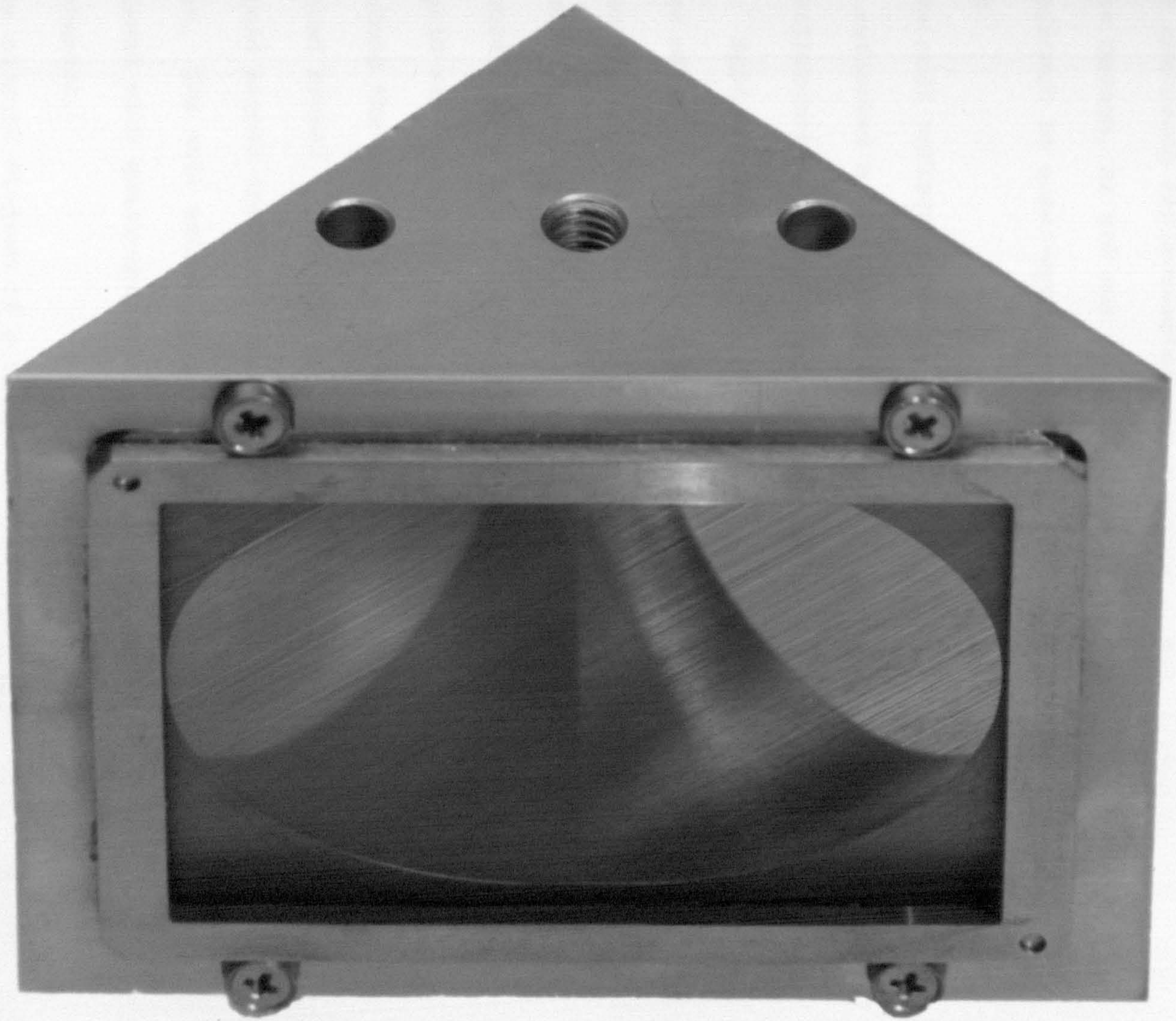

Fig. 5b

CHAPTER 6

A QUASI-OPTICAL NULL REFLECTOMETER

6.1 The null reflectometer

A precision reflectometer was required in the course of this work, and its design, as set out in this chapter, serves to illuminate well the approach to quasi-optical measurement systems developed in this thesis.

The null reflectometer is an instrument which measures the fractional power reflected by an object when a quasi-optical beam is incident upon it. The reflectometer is the quasi-optical analogue of the microwave VSWR meter. Applications include the characterisation of the refractive indices of mm wave materials and the quality of impedence matching achieved in quasi-optical components. It works by matching a fundamental Gaussian beam-mode reflected from the object under test against a similar beam reflected from a known reference. The reference reflector is a polarizing wire grid set normally to the reference beam axis. The position of the grid along the beam axis can be adjusted to alter the phase of the reflected signal. The grid can be rotated to alter the proportion of the polarized signal incident upon it reflected back in the same polarization. The *null* method avoids standing wave problems, which are often associated with quasi-optical systems because of reflections from source and detector.

The circuit diagram of a reflectometer built using split cubes is shown in Fig. 6a and a photograph is given in Fig. 6b. Lenses are placed in appropriate positions in the circuit to control the diffractive spreading of the beams, and both the object under test and the reference reflector are positioned at beamwaists. A horizontally polarized fundamental Gaussian beam-mode is generated at the source by a corrugated horn. This beam passes unaffected through a vertical analysing grid.

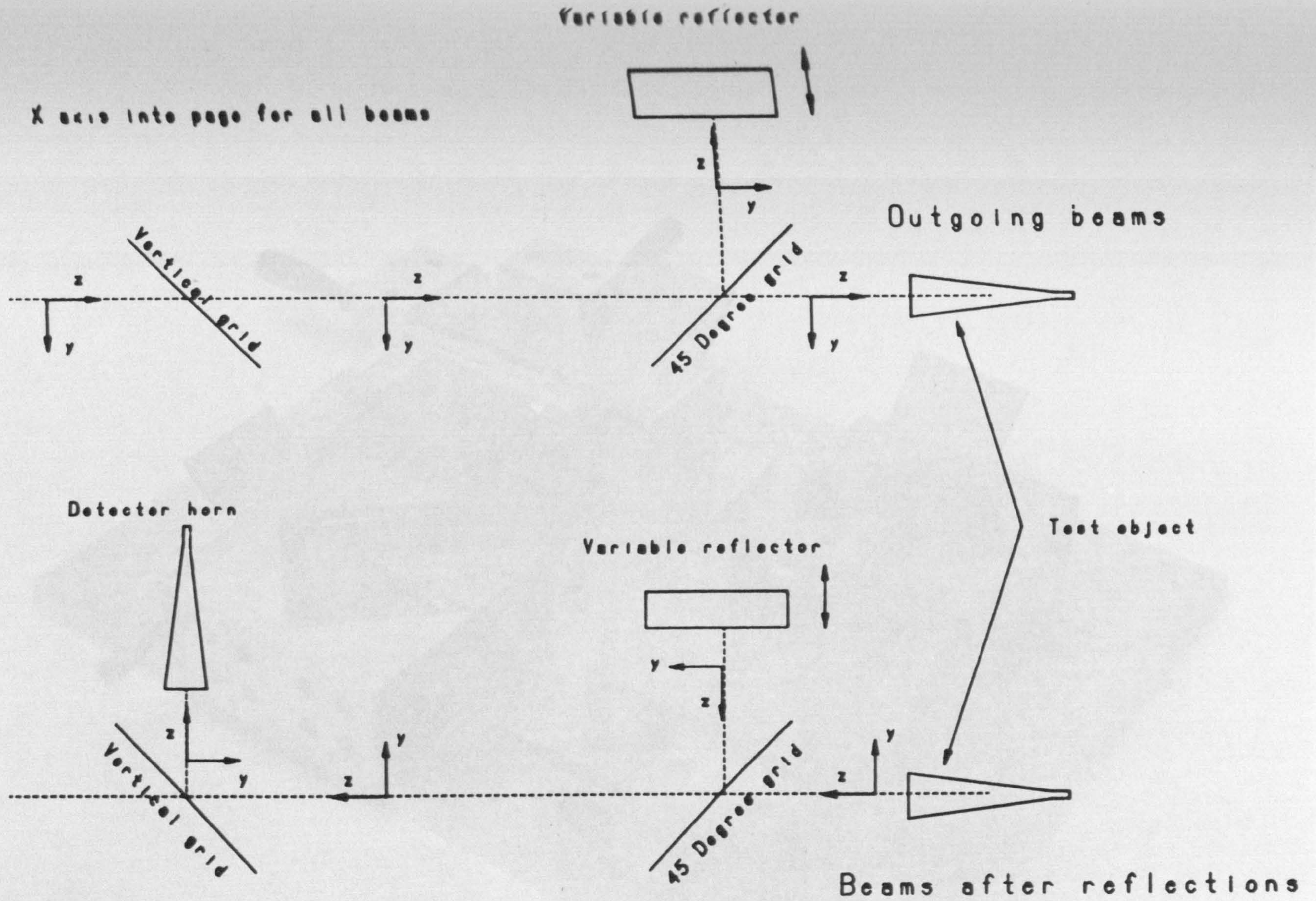

Fig. 6 a AXES DEFINITION FOR REFLECTOMETER

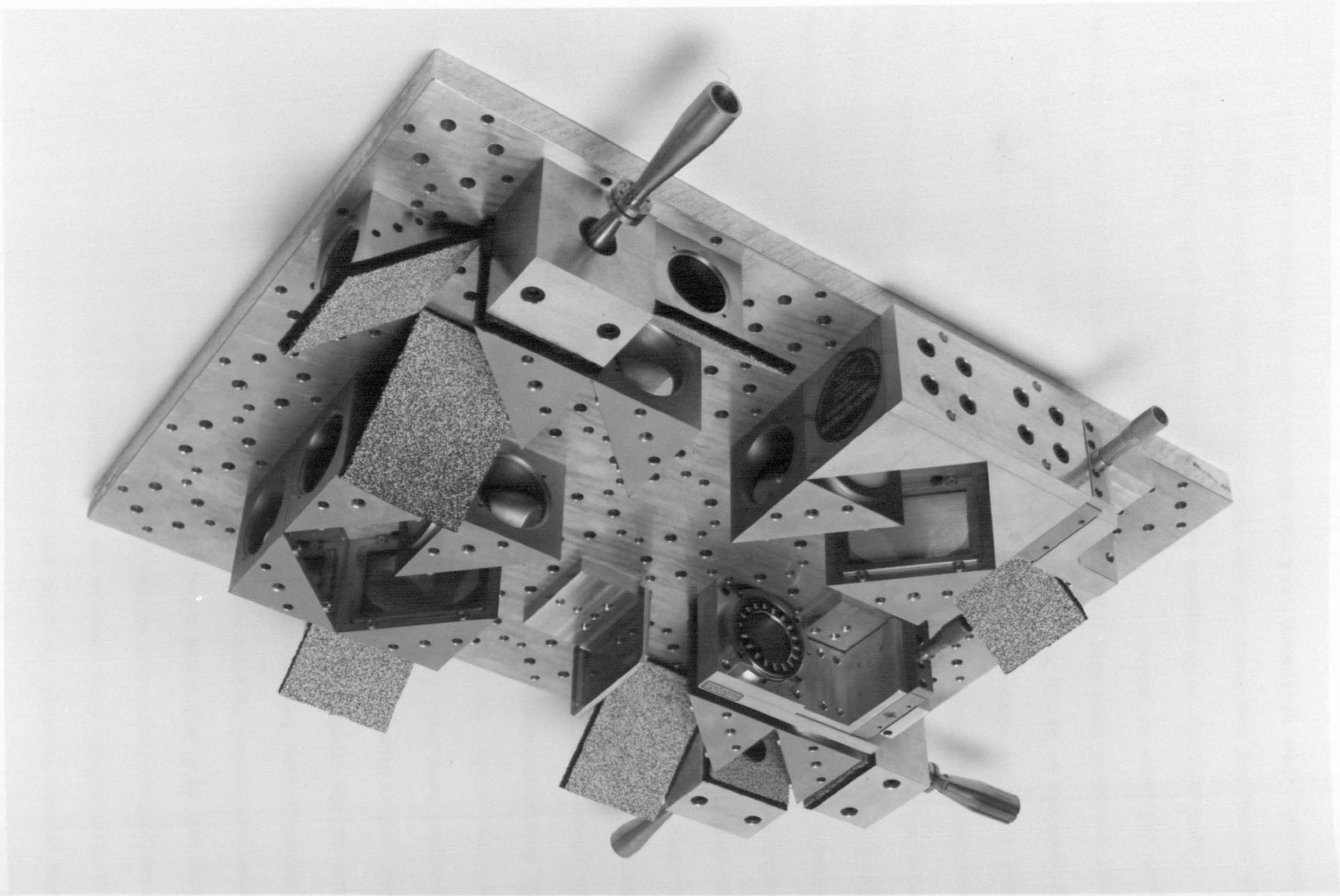

Fig. 6b

It then split into two equal amplitude beams by a diagonal grid. One beam passes through the grid and forms a beamwaist in the test arm at the test object (for example, a feed horn or lens). The other beam, polarized orthogonally to the beam in the test arm, is reflected by the diagonal grid and forms a beamwaist at the reference reflector. The beams reflected by both test object and reference pass back along their outward paths, are recombined at the diagonal grid and then travel back to the vertical grid. If the *copolarized* reflected beams from the test and reference arm are equal, both in amplitude and phase, then the returned beam will be horizontally polarized, and will pass through the vertical grid. No component will be reflected by the vertical grid into the detector feed horn. Otherwise the beam reaching the analysing grid will have a vertical component. This will be reflected by the grid and received by the detector feed horn. The reflections compared are, of course, only reflections into the set of Gaussian beam-modes received by the detector horn. Reflections into other modes are not detected. The instrument does not measure the fraction of power scattered out of the circuit by an object under test. However, scattering loss in quasi-optical circuits is often much less important than reflections back into the modes detected by horns which cause unwanted and troublesome standing waves. The section that follows shows that the amplitude reflectivity of the rotating grid into the diagonal polarization that will match the test sample's reflection is given by $\rho = \sin^2\delta$ where δ is the angle of the rotating grid measured from the diagonal setting - the angle at which the reference grid reflects no power.

Reflectivity measurements are most conveniently made by adjusting the phase and amplitude of the reference reflector until a null is acheived. The reference grid can then be rotated through the $\delta = 0$ position to find a second null angle at $-\delta$. The angle that the grid has rotated through is then 2δ. This method avoids the problem of determining

the exact grid position at which $\delta = 0$. Because the amplitude reflectivity of the reference grid is proportional to $\sin^2\delta$, the instrument is especially sensitive at low test object reflectivities and can measure down to power reflectivities of less than 0.1 %. This is equivalent, in microwave terms, to a VSWR of 1.05. Reflectometers of the form shown in Fig. 6b have proved to be very simple instruments to use, and they can help in the optimisation of mm wave component performance. For instance, Martin [1.7] has used a reflectometer and a variable frequency source to 'tune' the thickness of symmetrical lenses working around 94 GHz to reduce reflection losses. The next chapter outlines an important use of a reflectometer in measuring reflections from a 'back-to'back' corrugated horn used in a cosmic background measuring system.

6.2 A Jones matrix analysis of the reflectometer

We use a right handed orthogonal set of axes and take the positive Z direction as being the direction of propagation. The X axis lies perpendicular to the plane in which all the grids are fixed and is the same for all beams. The Y axis is as shown in Fig. 6a. Under this regime, the Jones matrices [6.1] for polarizing grids are

$$\begin{vmatrix} E_{xout} \\ E_{yout} \end{vmatrix} = \begin{vmatrix} -S^2 & SC \\ -SC & C^2 \end{vmatrix} \begin{vmatrix} E_{xin} \\ E_{yin} \end{vmatrix} \qquad (6.1)$$

in reflection, and

$$\begin{vmatrix} E_{xout} \\ E_{yout} \end{vmatrix} = \begin{vmatrix} C^2 & SC \\ SC & S^2 \end{vmatrix} \begin{vmatrix} E_{xin} \\ E_{yin} \end{vmatrix} \qquad (6.2)$$

in transmission, where $C \equiv \cos\phi$, $S \equiv \sin\phi$ and ϕ is the angle between the grid pass plane and the X axis.

Consider the elements in the circuit. An input beam $\begin{vmatrix} E_{xin} \\ E_{yin} \end{vmatrix}$ passes

through a vertical grid ($\phi = 0$). The transmission matrix is $\begin{vmatrix} 1 & 0 \\ 0 & 0 \end{vmatrix}$. It then passes to a grid with a pass plane set at 45° to the X axis, where the beam is split. The transmission matrix* is $\begin{vmatrix} 1/2 & 1/2 \\ 1/2 & 1/2 \end{vmatrix}$, and the reflection matrix* is $\begin{vmatrix} -1/2 & 1/2 \\ -1/2 & 1/2 \end{vmatrix}$. The two beams are then reflected back to the second grid. The reflection matrix for the object is

$\begin{vmatrix} -\rho & 0 \\ 0 & -\rho \end{vmatrix}$, where ρ is the amplitude reflectivity of the object under test into the fundamental mode. It is assumed that *no* crosspolarization occurs. It would not be difficult to analyse the effect of crosspolarization by adding cross terms into the Jones reflection matrix.

The variable reflector generates a beam given by the reflection matrix $\begin{vmatrix} -S^2 & SC \\ -SC & C^2 \end{vmatrix}$, and the first grid reflects a component $\begin{vmatrix} 0 & 0 \\ 0 & 1 \end{vmatrix}$ into the detector horn. It is this horn, of course, that defines the nature of the beam detected by the system. Combining all of these components one can calculate a transmission matrix for the whole system. Thus

$$\begin{vmatrix} E_{xout} \\ E_{yout} \end{vmatrix} = \underline{M} \begin{vmatrix} E_{xin} \\ E_{yin} \end{vmatrix}, \qquad (6.3)$$

Detector Source

$\underline{M} =$

$$\begin{vmatrix} 0 & 0 \\ 0 & 1 \end{vmatrix} \begin{vmatrix} 1/2 & 1/2 \\ 1/2 & 1/2 \end{vmatrix} \begin{vmatrix} -\rho & 0 \\ 0 & -\rho \end{vmatrix} \begin{vmatrix} 1 & 0 \\ 0 & 1 \end{vmatrix} \begin{vmatrix} 1/2 & 1/2 \\ 1/2 & 1/2 \end{vmatrix} \begin{vmatrix} 1 & 0 \\ 0 & 0 \end{vmatrix} \begin{vmatrix} -1/2 & 1/2 \\ -1/2 & 1/2 \end{vmatrix} \begin{vmatrix} -S^2 & SC \\ -SC & C^2 \end{vmatrix} \begin{vmatrix} e^{i\psi} & 0 \\ 0 & e^{i\psi} \end{vmatrix} \begin{vmatrix} -1/2 & 1/2 \\ -1/2 & 1/2 \end{vmatrix}.$$

(6.4)

*Ignoring a phase term which does not affect these calculations.

Contracting the matrix gives $\underline{M}$ =

$$\begin{vmatrix} 0 & 0 \\ 0 & 1 \end{vmatrix} \begin{vmatrix} -\rho/2 & -\rho/2 \\ \rho/2 & \rho/2 \end{vmatrix} \begin{vmatrix} 1 & 0 \\ 0 & 0 \end{vmatrix} \cdot \begin{vmatrix} -1/2 & 1/2 \\ -1/2 & 1/2 \end{vmatrix} \begin{vmatrix} -S^2e^{i\psi} & SCe^{i\psi} \\ -SCe^{i\psi} & C^2e^{i\psi} \end{vmatrix} \begin{vmatrix} -1/2 & 1/2 \\ -1/2 & 1/2 \end{vmatrix} \tag{6.5}$$

But

$$\begin{vmatrix} -Se^{i\psi} & SCe^{i\psi} \\ -SCe^{i\psi} & C^2e^{i\psi} \end{vmatrix} \begin{vmatrix} -1/2 & 1/2 \\ -1/2 & 1/2 \end{vmatrix} = \frac{1}{2} \begin{vmatrix} (S^2-SC)e^{i\psi} & (-S^2+SC)e^{i\psi} \\ (-C+SC)e^{i\psi} & (-SC+C^2)e^{i\psi} \end{vmatrix} ; \tag{6.6}$$

hence $\underline{M}$ =

$$\begin{vmatrix} 0 & 0 \\ 0 & 1 \end{vmatrix} \begin{vmatrix} -\rho/2 & 0 \\ \rho/2 & 0 \end{vmatrix} \begin{vmatrix} -(1-2SC)e^{i\psi} & 0 \\ -(1-2SC)e^{i\psi} & 0 \end{vmatrix}$$

$$= - \begin{vmatrix} 0 & 0 \\ 0 & +\rho/2 \; -1/2(1-2SC)e^{i\psi} \end{vmatrix} . \tag{6.7}$$

Thus the null occurs when $\psi = 0$ and

$$\rho = 1/2(1 - 2\,\mathrm{Sin}\phi\,\mathrm{Cos}\phi) = 1/2(1 - \mathrm{Sin}2\phi). \tag{6.8}$$

Putting $\phi = \pi/4 + \delta$

$$\rho = 1/2(1 - \mathrm{Cos}2\delta) = \mathrm{Sin}^2\delta, \tag{6.9}$$

and the power reflectivity $R = \mathrm{Sin}^4\delta$.

Thus the amplitude reflectivity of the sample in the mode received by the detector feed horn is given by the square of the sine of the angle between the zero reflection position and the null position of the reference grid.

6.3 Effect of instrument error on the measured reflection coefficient

Measurements of the reflectivity at 130 GHz of a back-to-back corrugated horn used in a cosmic background experiment are outlined in the next chapter. In such a measurement, where low reflectivity is desired, it is important to ensure that any systematic errors overestimate the reflection coefficient. The instrument can then be adjusted in the knowledge that the minimum reflection value observed is an upper limit.

Consider first errors caused by the diagonal beam splitter wires not being set at the correct 45° angle to the angle of the analysing grid. Let the error be $\delta\theta$ and consider the test sample arm first. The amplitude of the beam falling onto the test object is proportional to $\sin(45^{\circ} + \delta\theta)$ but the amplitude the beam passing back to the analysing grid after the beam has been reflected and recombined at the diagonal grid is proportional to $\sin(45^{\circ} + \delta\theta)\ \sin(45^{\circ} - \delta\theta)$. Similarly, the reference component returned to the analysing grid is proportional to $\sin(45^{\circ} - \delta\theta)\ \sin(45^{\circ} + \delta\theta)$. Thus the angle of the beamsplitter wires does not alter the null position of the reference reflector. However the sensitivity of the reflectometer is maximised with $\delta\theta = 0$.

Secondly, suppose the beam splitting grid is not set at the correct position to reflect a beam from the main optical axis into the reference arm. The test arm is unaffected because it receives power by transmission. However, the beam returned by the reflector will be reduced by any error in the position of the beam splitting grid. The reflection coefficient will therefore be overestimated, as required.

Thirdly, errors could be caused by reflections at lenses. Only the two lenses that directly form the beamwaists at the test and reference reflector positions can have any effect. Differences in the amplitude and phase of reflections from these lenses into the fundamental beam-mode could cause errors which might underestimate reflectivity of the test object. To guard against this the lenses can be interchanged to check

that there is no significant difference between their reflections.

Finally, any errors in the position, angle or reflectivity of the reference reflector will reduce the power coupled back into the fundamental beam-mode again so the reflection coefficient will be overestimated.

6.4 Measurements with the reflectometer

The null reflectometer, built using split cubes, has proved to be a sensitive and versatile instrument for the measurement of low level reflections. Richard Martin [6.2] has made extensive measurements here of the reflections from dielectric slabs and horns. Fig. 6c shows the reflection from two slabs of HDPE over a band of frequencies. It clearly shows that phase cancellation of reflections from back and front surfaces occurs at 94 GHz for the slab 8.42 mm thick while for a slab $\lambda/4$ thicker at the same frequency, phase addition occurs. Fig. 6d shows reflections from the aperture of a corrugated horn designed to operate at 94 GHz. Reflections are, at worst, just over 1% and are below .2% over a 2 GHz band, indicating that the corrugated/smooth waveguide transition at the throat of the horn (see Section 2.3) is functioning correctly.

— HDP disc thickness 8.42 mm., —.— HDP disc thickness 7.84 mm..

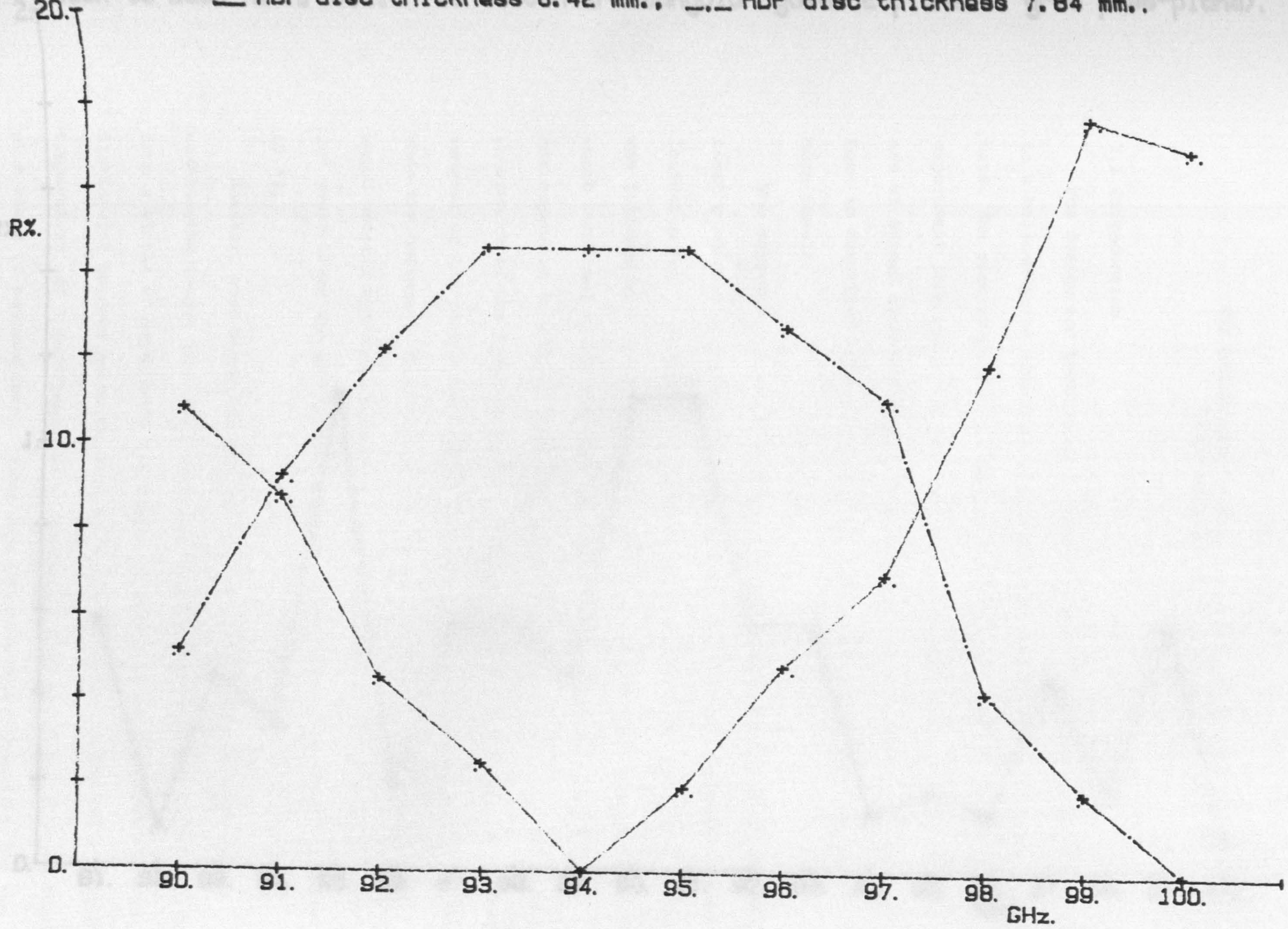

Fig. 6c

Back-to-back horn, scalar to smooth (rectangular-guide E-plane 11 grid pass-plane).

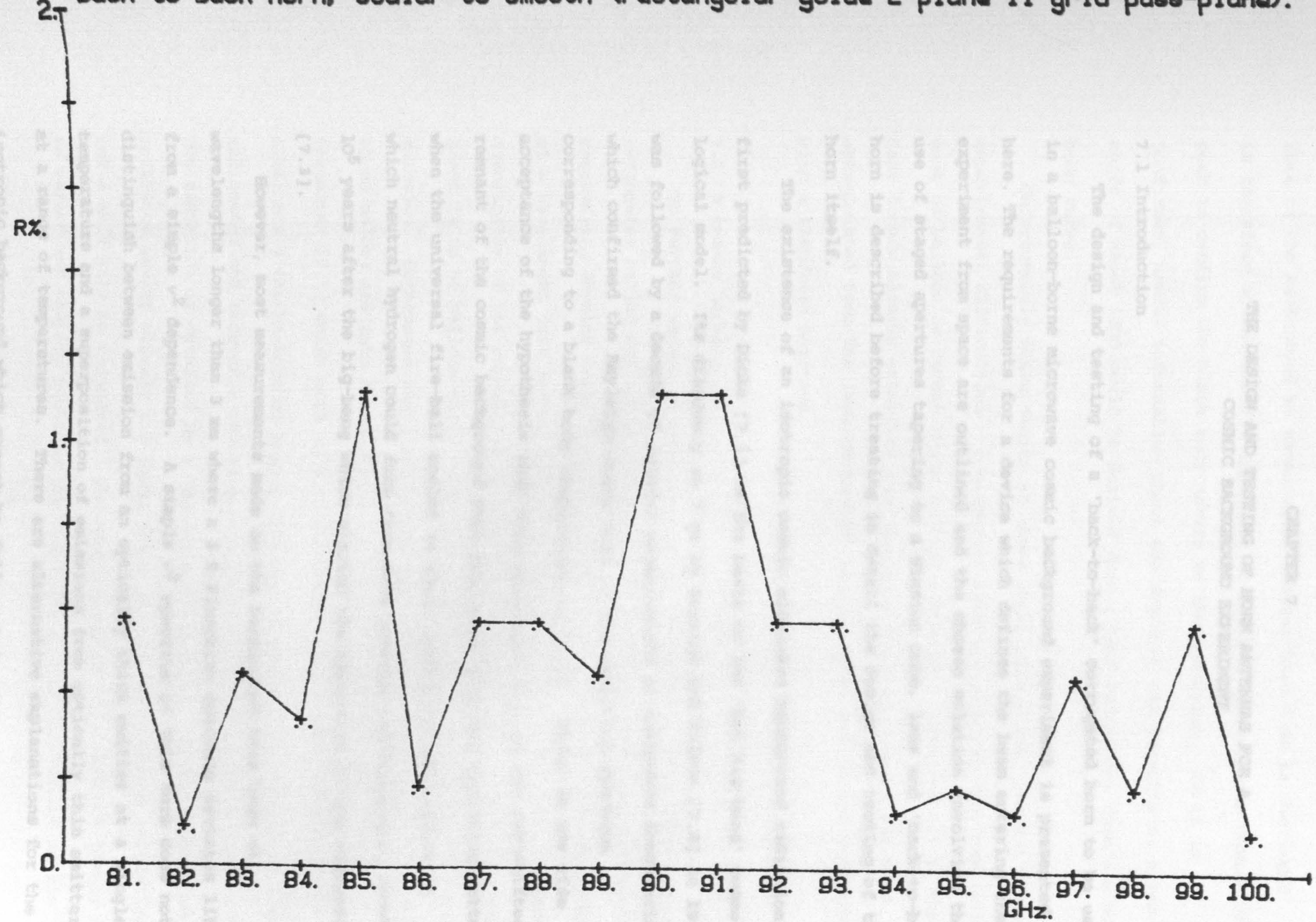

Fig. 6d

CHAPTER 7

THE DESIGN AND TESTING OF HORN ANTENNAS FOR A COSMIC BACKGROUND EXPERIMENT

7.1 Introduction

The design and testing of a 'back-to-back' corrugated horn to be used in a balloon-borne microwave cosmic background experiment is presented here. The requirements for a device which defines the beam entering the experiment from space are outlined and the chosen solution involving the use of staged apertures tapering to a Winston cone, lens and 'back-to-back' horn is described before treating in detail the design and testing of the horn itself.

The existence of an isotropic cosmic microwave background radiation was first predicted by Dicke [7.1] on the basis of the 'hot big-bang' cosmological model. Its discovery at 7 cm by Penzias and Wilson [7.2] in 1967 was followed by a decade of careful measurements at microwave frequencies which confirmed the Rayleigh-Jeans form of the radiation spectrum corresponding to a black body temperature of 2.7 K. There is now wide acceptance of the hypothesis that this microwave flux is the red-shifted remnant of the cosmic background that decoupled from the expanding matter when the universal fire-ball cooled to about 3000 K, a temperature at which neutral hydrogen could form from free protons and electrons, about 10^5 years after the big-bang which started the expansion of the universe [7.3].

However, most measurements made on the background have been at wavelengths longer than 3 mm where a 3 K Planckian spectrum deviates little from a simple ν^2 dependence. A simple ν^2 spectrum of this form does not distinguish between emission from an optically thick emitter at a single temperature and a superposition of emissions from optically thin emitters at a range of temperatures. There are alternative explanations for the isotropic background which cannot be fully ruled out until the Planckian

form of the background at wavelengths shorter than 3 mm is confirmed. It is therefore scientifically important to measure the spectrum across the peak to confirm the black body nature of the radiation. If it is confirmed, useful information about the state of the universe at a red-shift of about 1000 could be derived from slight deviations from a black body curve.

Unfortunately measurements at these short wavelengths present severe experimental difficulties - atmospheric emission requires that experiments must be balloon or rocket borne to high altitudes. Measurements in the last decade clearly establish that the flux falls well below the form extrapolated from the long wavelength measurements, and is not inconsistent with a Planckian spectrum.

7.2 A cosmic background radiometer

To further refine measurements around the peak, a cosmic background radiometer called CBS (Cosmic Background System) has been designed in the Engineering Physics Group in Queen Mary College to measure the background at a wavelength just longer than 2 mm, to an accuracy of 0.01 K. A general description of the experiment is given by Martin [7.4]. Briefly the experiment is to be balloon-borne to an altitude of 30 km to avoid atmospheric emission. Background radiation passes through a receiving antenna (described below) and into a radiometer unit which includes a polarizing interferometer [7.5] which acts as a Dicke switch, directing to the detector alternately the background signal beam and a reference cavity beam. The radiometer and reference cavity are cooled by liquid helium to about 1.5 K. The radiation is detected by a ^{3}He cooled bolometer. If the background and reference cavity signals are equal there will be no resultant modulation and a null will be indicated. The temperature of the reference cavity can be varied and thereby provides the means for a null calibration of the

background signal. The detector should give the required temperature resolution in about one hour's integration time.

7.3 The antenna for CBS.

To ensure that spurious sources do not generate signals above the required 0.01 K, the antenna system must have very low sidelobes. Spurious signals will come from the earth at 300 K and from earthshine reflected from the balloon. (The experimental package is to be lowered down from the balloon on a 500 m cable to reduce its optical presence.) Detailed calculations indicate that the requirements are:

Rejection $\geq$ 10^4 at 30 degrees off boresight

Rejection $\geq$ 10^7 at 60 degrees off boresight

Rejection $\geq$ 10^9 at 90 degrees off boresight

Moreover, the antenna system bridges the external parts of the CBS at ~ 300 K to the cold radiometer at 1.5 K; internal beam control is also of great importance therefore.

To achieve these levels of performance a sophisticated antenna is needed. The approach taken is (Fig. 7a) to form the main beam with a corrugated-horn and lens combination and to design this so that the beam is heavily tapered at the edges of the several apertures through which it passes on its way from the cold radiometer to the warm exterior of the system. The apertures are staged in diameter to give multiple diffraction and are connected by a reflecting cone to redirect diffracted power back into the boresight direction [7.6].

The horn-lens antenna defines the beam on the sky; in order to pass the signal beam to the detector through the quasi-optical Dicke switch system a second horn is connected back-to-back with the first (Figure 7a). The design, manufacturing and testing techniques developed in the work

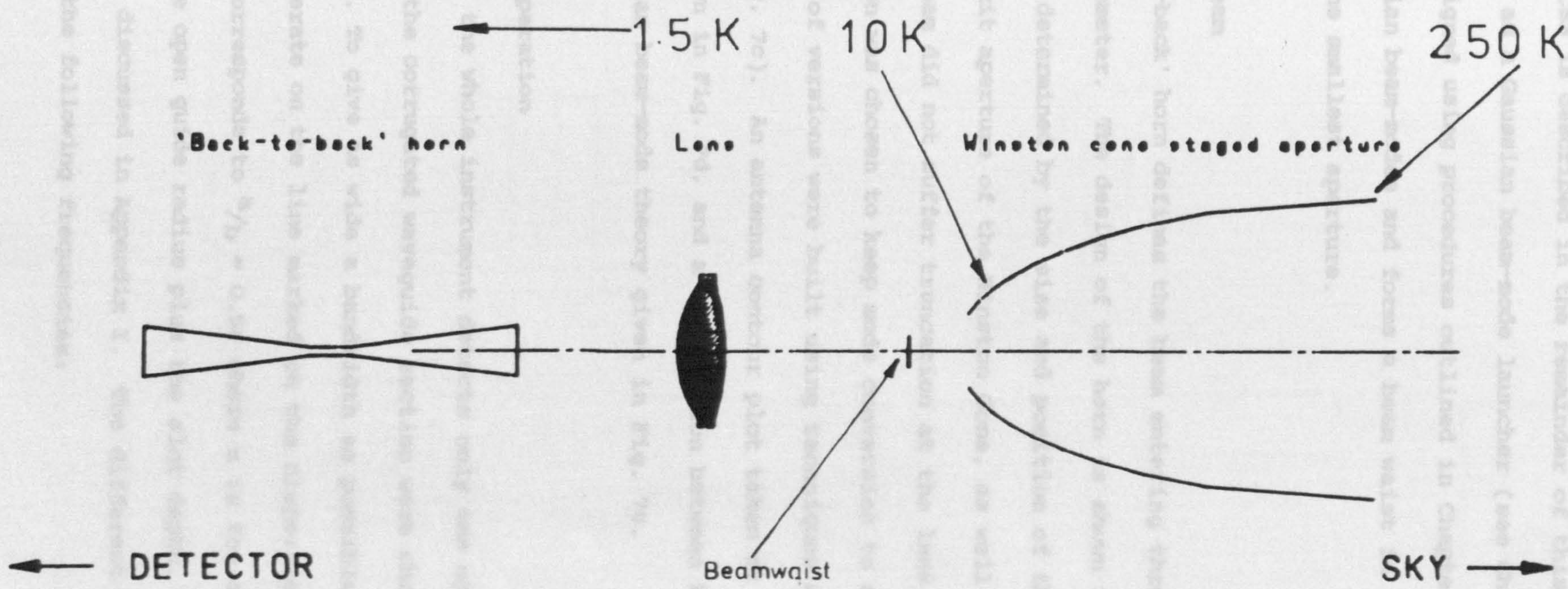

Fig. 7 a CBS ANTENNA DESIGN

described in this thesis were used for the horn-lens combination of CBS and that part of CBS is described in the remainder of this chapter.

The horn acts as a Gaussian beam-mode launcher (see Chapter 2 Section 5). The lens, designed using procedures outlined in Chapter 3, picks up the propagating Gaussian beam-modes and forms a beam waist in front of the Winston Cone at the smallest aperture.

7.4 Forming the beam

The 'back-to-back' horn defines the beam entering through the antenna and into the radiometer. The design of the horn is shown in Fig. 7b. The aperture size was determined by the size and position of the beamwaist required at the exit aperture of the Winston Cone, as well as the need to ensure that the beam did not suffer truncation at the lens. The length of the tapered section was chosen to keep mode conversion to acceptable limits. A number of versions were built using techniques described in Chapter 2 (see Fig. 7c). An antenna contour plot taken at 130 GHz of the IB version is shown in Fig. 7d, and a comparision between the experimental pattern and Gaussian beam-mode theory given in Fig. 7e.

7.5 Single mode operation

To ensure that the whole instrument detects only one optical mode, the dimensions of the corrugated waveguide section were chosen to pass only the HE_{11} mode. To give as wide a bandwidth as possible, the section was designed to operate on the line marked on the dispersion graph (Fig. I.1) which corresponds to $a/b = 0.58$ where a is the open guide radius and b is the open guide radius plus the slot depth. The form of the disperion graph is discussed in Appendix I. The different modes should cut on and off at the following frequencies:

Details of slots in guide
"T" and "R" to be as small
as possible

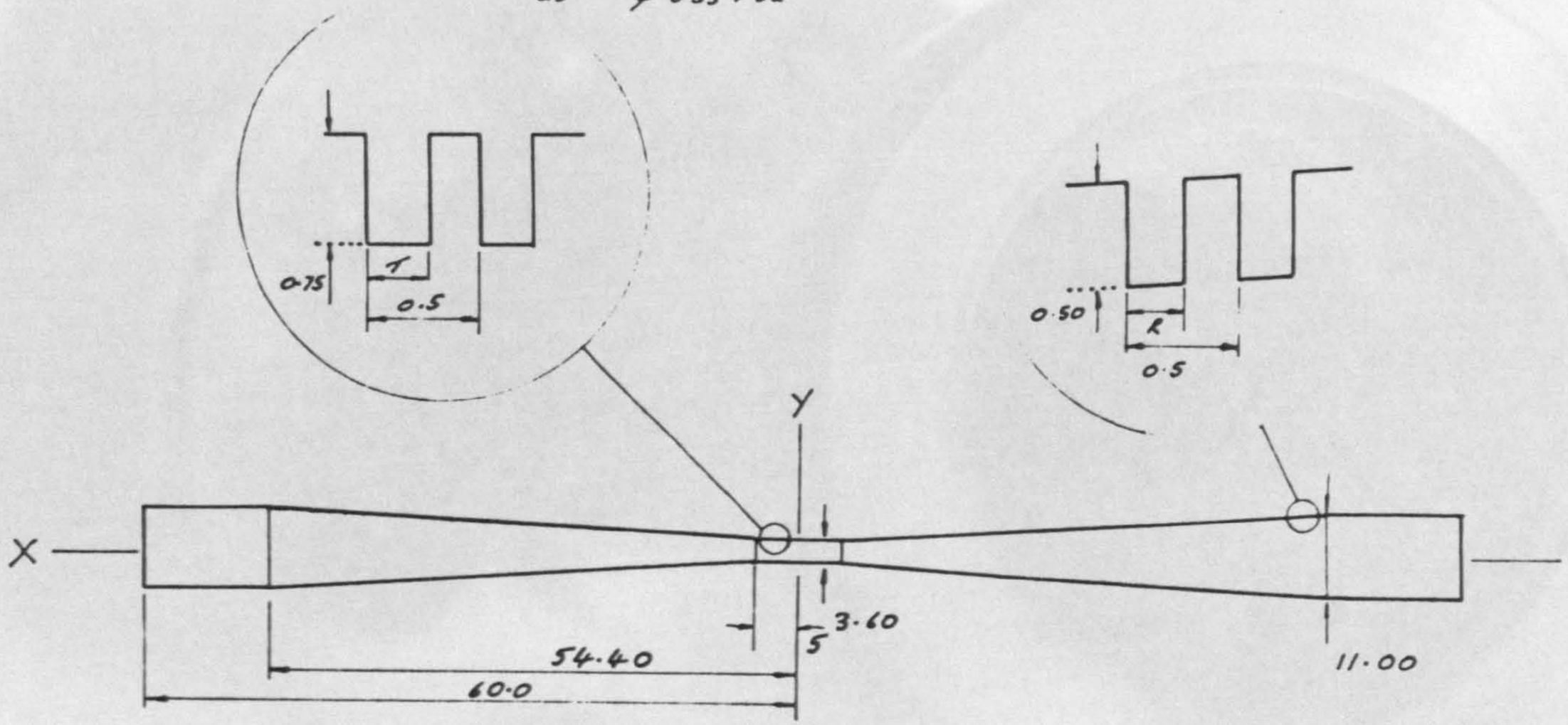

ROTATIONAL SYMMETRY ABOUT "X"

SYMMETRY IN PLANE THROUGH "Y"

TOLERANCE ± 0.05 DURAL

	NEW ISSUE	
REF.	REVISION	DATE

CUSTOMER C B S

TITLE Dual Corrugated Horn Assembly

PROJECTION 3RD. ANGLE	SCALE ~ 2 : 1	DRN. RDT	CHKD.
COMPONENT NR	TOOL NR	DRAWING NR	

THOS. KEATING LTD
BILLINGSHURST
SUSSEX.

NR OF SHTS. 1 | SHT NR 1

Fig. 7b

Fig. 7c

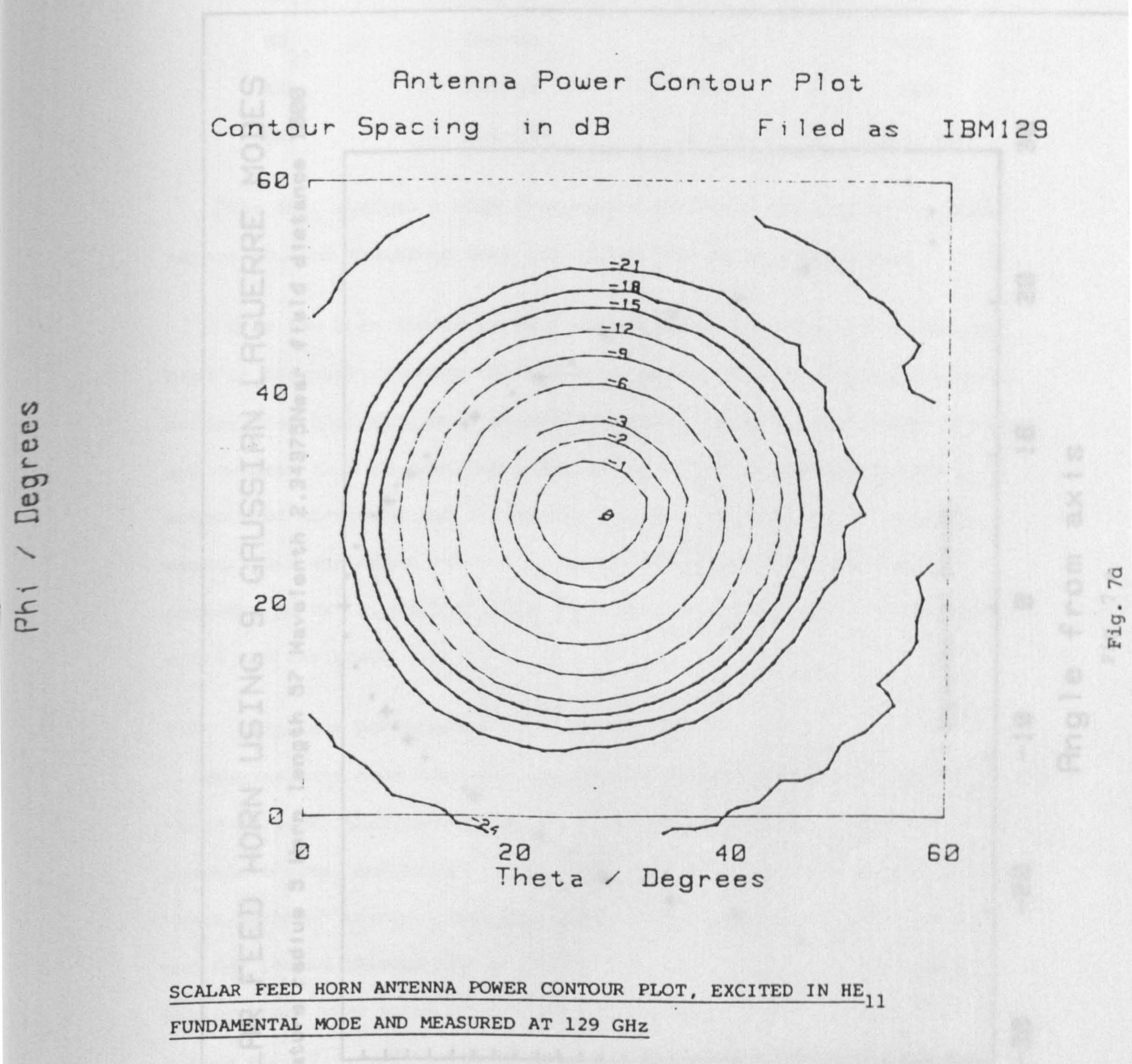

Fig. 7a

SCALAR FEED HORN ANTENNA POWER CONTOUR PLOT, EXCITED IN HE_{11} FUNDAMENTAL MODE AND MEASURED AT 129 GHz

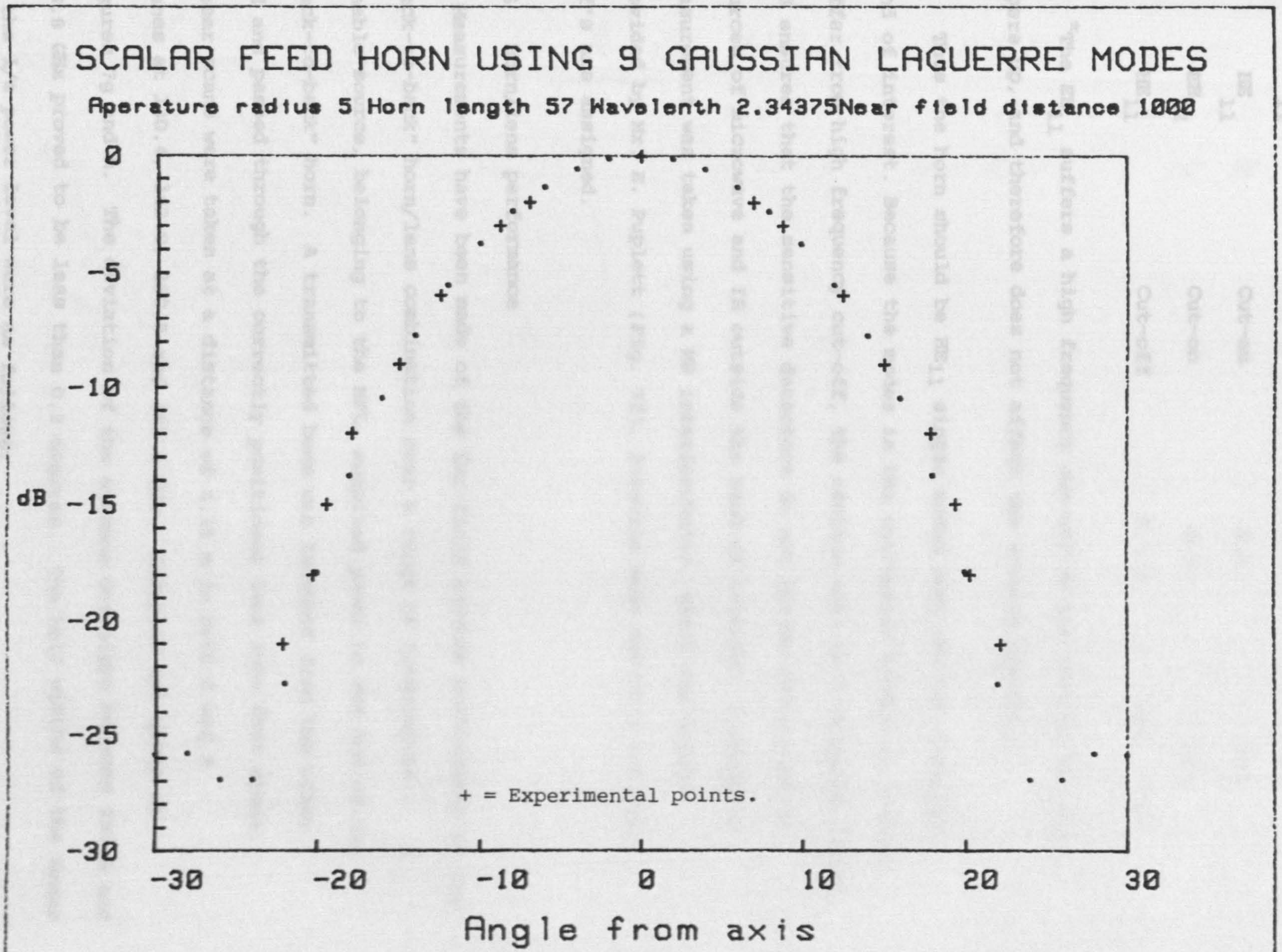
SCALAR FEED HORN USING 9 GAUSSIAN LAGUERRE MODES
Aperature radius 5 Horn length 57 Wavelenth 2.34375Near field distance 1000
0
-5
-10
dB -15
-20
-25
-30
-30
-20
-10
0
10
20
30
+ = Experimental points.
Angle from axis

Fig. 7 e

Mode	Type	$k_o a$	Frequency/GHz
EH_{11}*	Cut-on	1.8	80
HE_{11}	Cut-on	2.2	100
EH_{12}	Cut-on	4.1	185
HE_{11}	Cut-off	5 - 7	225 - 320

*The EH_{11} suffers a high frequency cut-off as the corrugated horn tapers up, and therefore does not affect the antenna operation.

Thus the horn should be HE_{11} single moded over the CBS frequency band of interest. Because the modes in the corrugated waveguide section suffer from high frequency cut-off, the section acts as a bandpass filter and ensures that the sensitive detectors do not become overloaded by sources of microwave and IR outside the band of interest. A bandpass measurement was taken using a MP interferometer, which was kindly provided by Mr. E. Puplett (Fig. 7f). Possible mode cut-on's and cut-off's are assigned.

7.6 Horn/lens performance

Measurements have been made of the far-field antenna performance of the "back-to-back" horn/lens combination over a range of frequencies*. A tunable source, belonging to the NPL, supplied power to one end of the "back-to-back" horn. A transmitted beam was launched from the other end and passed through the correctly positioned lens into free space. Linear scans were taken at a distance of 4.15 m in both E and H planes at 130.4, 142.9, 150.5 and 158.8 GHz. Examples are given in Figures 7g and h. The deviation of the antenna boresight between 130.4 and 158.8 GHz proved to be less than 0.3 degrees. The half widths of the beams at the 1/e power level were as follows:

*I am grateful to Mr. D. Adamson for making these measurements

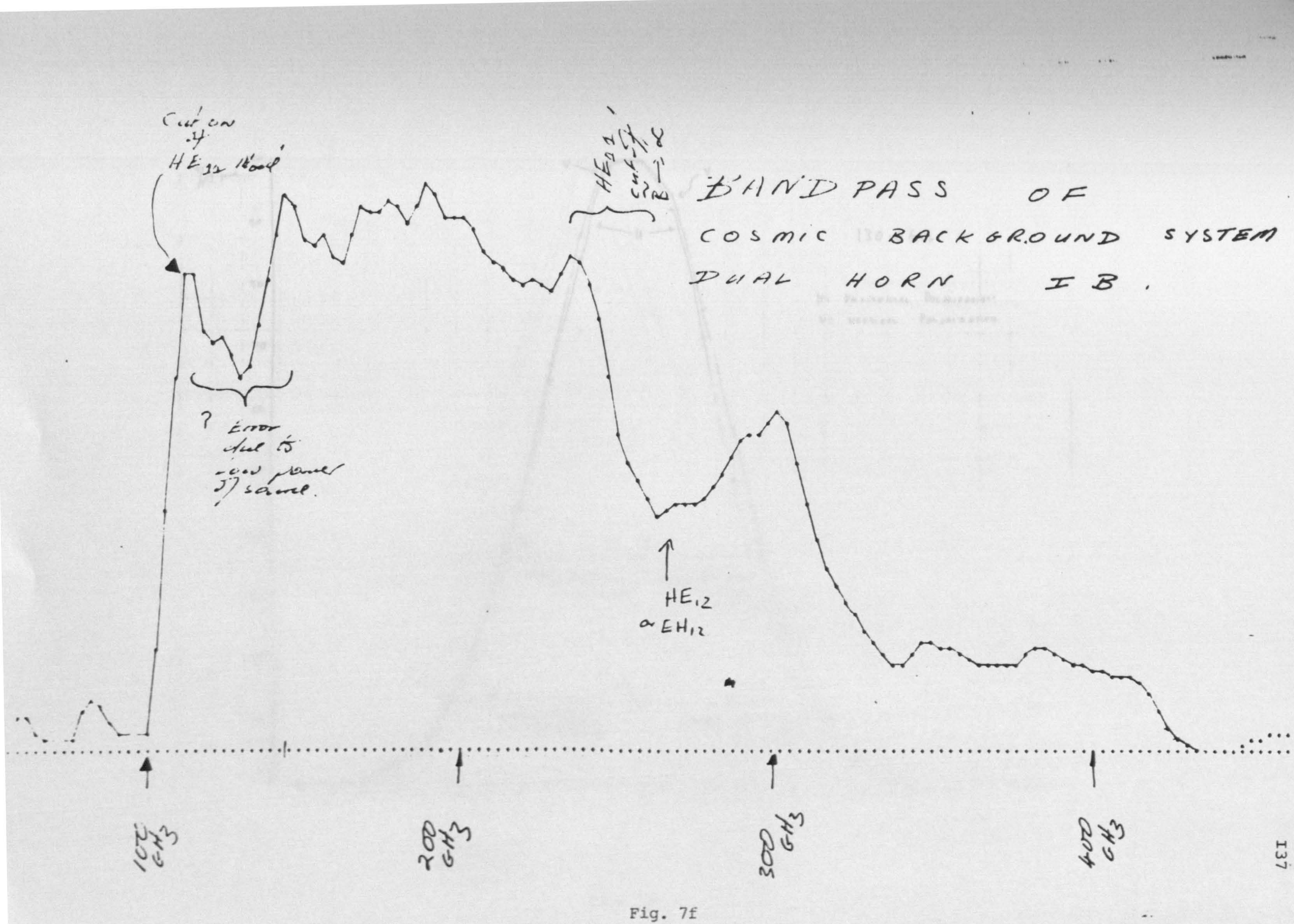

BAND PASS OF COSMIC BACKGROUND SYSTEM DUAL HORN IB.

Fig. 7f

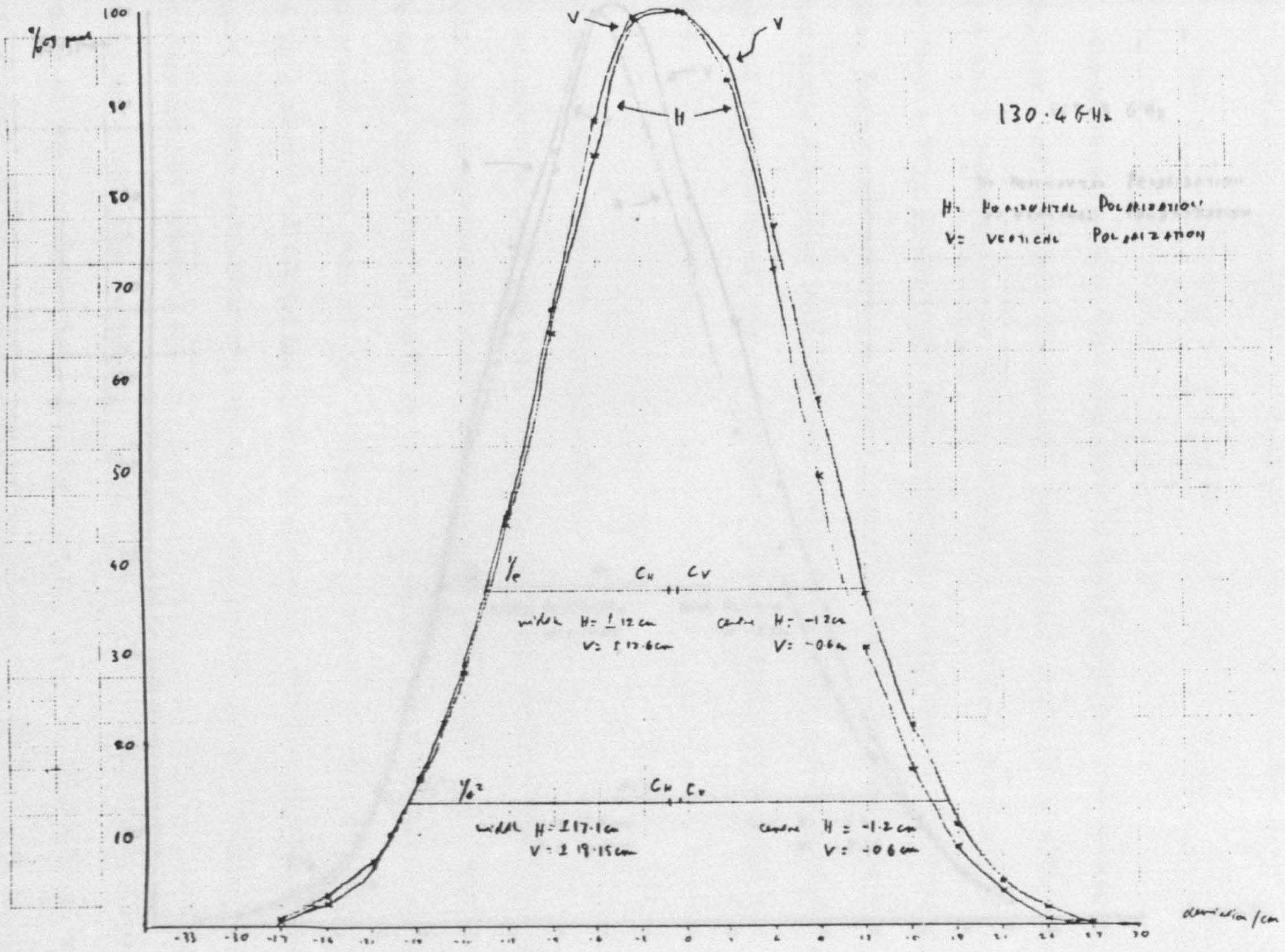
100
90
80
70
60
50
40
30
20
10
V
V
H
130·4 GHz
H: HORIZONTAL POLARIZATION
V: VERTICAL POLARIZATION
½e
CH CV
middle H: ± 12 cm
V: ± 17·6 cm
centre H: -1·2 cm
V: -0·6 cm
½e²
CH CV
middle H: ± 17·1 cm
V: ± 19·15 cm
centre H: -1·2 cm
V: -0·6 cm
deviation / cm

Fig. 7g

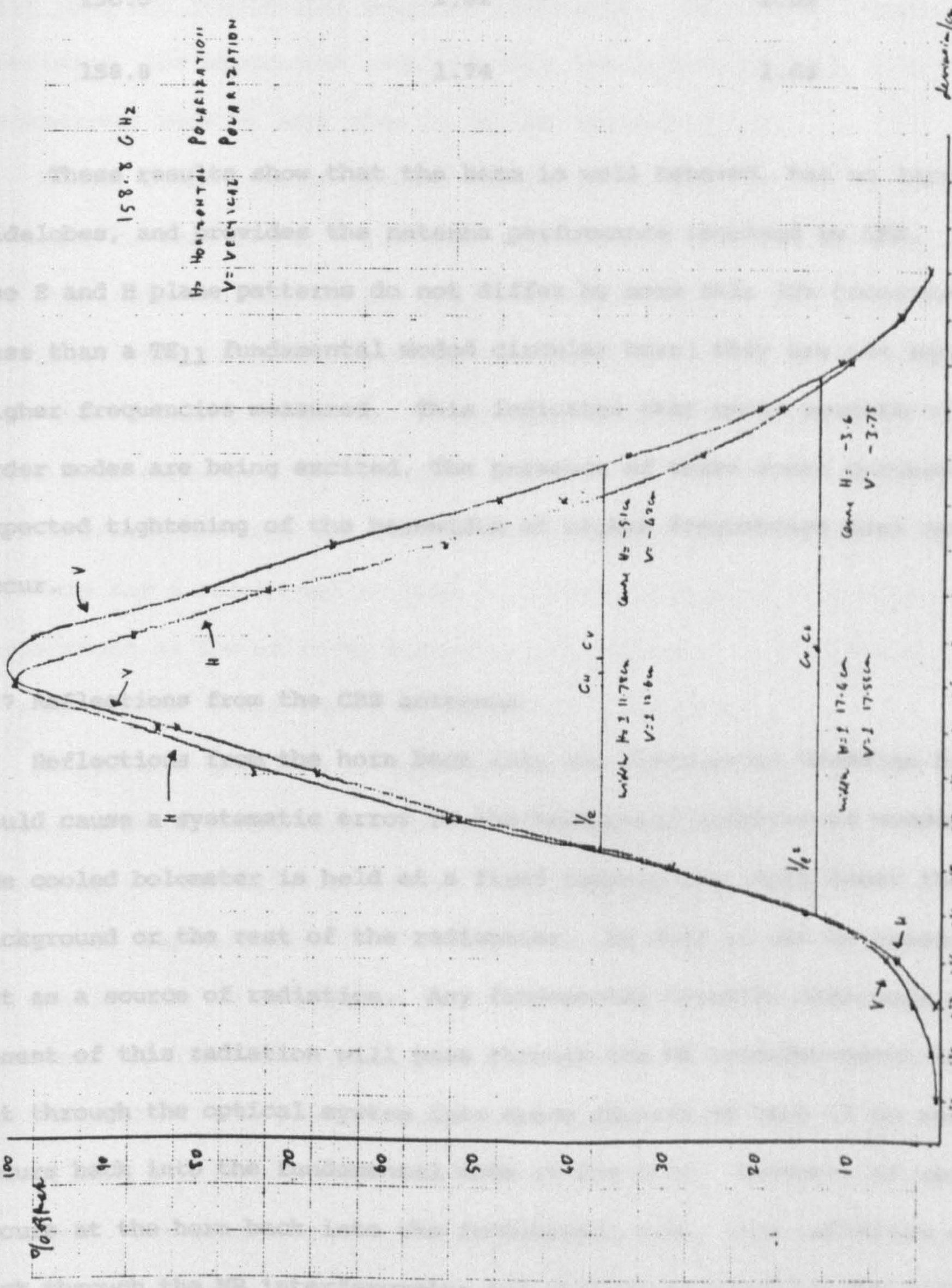
158.8 GHz
H= Horizontal Polarization
V= Vertical Polarization
V
H
V
H
V
H
V
H
Cw Cv
Cw Cv
Cw Cv
1/e
1/e²
Width H = 11.78cm
V = 13.6cm
Width H = 17.6cm
V = 17.55cm
Beam H: -3.6
V: -3.75
100
90
80
70
60
50
40
30
20
10
% of Peak

Fig. 7h

Frequency/GHz	Vertical/Degrees	Horizontal/Degrees
130.4	1.74	1.66
142.9	1.63	1.72
150.5	1.82	2.02
158.8	1.74	1.63

These results show that the beam is well behaved, has no large sidelobes, and provides the antenna performance required by CBS. Although the E and H plane patterns do not differ by more than 10% (considerably less than a TE_{11} fundamental moded circular horn) they are not equal at the higher frequencies measured. This indicates that small amounts of higher order modes are being excited. The presence of these modes ensures that the expected tightening of the beamwidth at higher frequencies does not occur.

7.7 Reflections from the CBS antennas

Reflections from the horn back into the fundamental Gaussian beam-mode could cause a systematic error in the background temperature measured. The ^{3}He cooled bolometer is held at a fixed temperature, much lower than the background or the rest of the radiometer. As such it can be considered to act as a source of radiation. Any fundamental Gaussian beam-mode component of this radiation will pass through the MP interferometer and out through the optical system into space causing no harm if no reflection occurs back into the fundamental mode at the horn. However, if reflection occurs at the horn back into the fundamental mode, this radiation will pass back through the MP interferometer and will be detected by the bolometer. This will cause a systematic error in the temperature measured. It is in principle possible to allow for the effect by measuring it. This is not as difficult as might at first be supposed since the error signal

will have passed twice through the MP interferometer, and so be distinguishable from a background signal. If the effect has to corrected however, the experiment ceases to be a truly null experiment. It is important therefore to be able to measure the reflection at the horn back into the fundamental Gaussian beam-mode. To achieve centikelvin precision, the experiment requires that the reflection back into the fundamental mode be less than 2% of the incident power.

A null reflectometer circuit was built up using 50 mm split cubes designed to work at 115 - 130 GHz. The results for the CBS IB horn at 130 GHz indicated that δ, the null reflection angle, was between 19 and 13 degrees. This indicates that the reflectivity back into the fundamental mode was between 0.4% and 1% at 130 GHz, which is acceptable and somewhat lower than expected. To develop a theoretical treatment of reflection from a corrugated horn and wave-guide is difficult. We have formulated a theory for a smooth-walled horn of similar dimensions and find that reflections as low as those measured with the CBS corrugated horn should be realisable. (This theory is presented in Appendix II).

It was also possible to estimate the transmission of the horn by placing a metal plate reflector hard up against one end of the horn and measuring the reflectivity of the horn to a Gaussian beam-mode entering the other end. Measurements of the null reflection angle gave a typical value for the IB horn of 70 degrees at 130 GHz. This converts to a single passage loss of 10%. However, more direct methods indicate that the loss is less than this. The power transmitted from an IMPATT driven corrugated source horn juxtaposed with an identical horn feeding a power meter was recorded. The IMPATT operated at 115 GHz. The IB 'back-to-back' horn was inserted, and the power drop was measured to be 3%. This result must also be treated with caution, as resonance and pulling effects could reduce the observed loss. However, because CBS is a null experiment, loss in the corrugated horn will only reduce the sensitivity of the instrument rather

than introduce any systematic errors. Loss therefore only increases the integration time required to reach any given level of accuracy.

7.8 Conclusion

The 'back-to-back' corrugated horn provides the desired beamforming for the CBS antenna. The sidelobes of the beam generated by the horn have been measured to be below -20 dB over the band of interest. Reflections from the horn back into the fundamental Gaussian beam-mode, which could cause a systematic distortion, are sufficiently low at 1% or less not to be a problem.

The antenna has been incorporated in the CBS system which is to be used in the ballon-borne measurement in September 1985.

CHAPTER 8

THE QUASI-OPTICAL DESIGN OF A 115 GHz RECEIVER USING A NOVEL SSB FILTER

8.1 Introduction

The second major purpose to which the work described in this thesis has been put is the design and testing of a quasi-optical front-end for an all-solid-state 115 GHz receiver suitable for unattended (possibly balloon-borne) operation including a novel single sideband filter.

High performance mm-wave superheterodyne receivers often employ vacuum tube local oscillator (LO) sources with associated bulky high voltage power supplies and water cooling. This tends to restrict their use in astronomy to ground-based attended operation. Recent advances in the design of solid state sources, such as IMPATT and GUNN diodes, as well as doublers and triplers using Schottky diodes, have opened the possibility of making much lighter receivers requiring only low voltage power supplies.

Unfortunately solid state sources tend to be of low power, noisy and susceptible to 'pulling' - their frequency changes if their output power is returned to them. The quasi-optical approach outlined in the previous chapters has been used to overcome these problems. Loss between the LO source and mixer was kept low through efficient optical coupling. A quasi-optical isolator reduced reflections from the mixer back into the LO source and a quasi-optical diplexer overlaid the LO and signal beams providing LO noise rejection at the signal frequency.

Basic superheterodyne receivers detect signals on both their upper and lower sidebands, above and below their LO frequency. In some radiometric measurements, double sideband (DSB) operation is satisfactory. However in many applications (e.g. molecular-line observations in radio astronomy) signals from only one sideband must be detected - the other sideband must

be rejected. Dichroic plate filters are quite attenuating (2 dB being typical) and are untunable. The receiver described in this chapter uses a novel arrangement to provide tunable low-loss sideband rejection.

8.2 The 115 GHz superheterodyne receiver

A block diagram of the receiver is shown in Fig. 8a. Linearly polarized signals first passes through the single-sideband filter. Signal and LO are then overlayed in the quasi-optical diplexer and are coupled into a waveguide-mounted mixer by a corrugated horn. The LO is generated in a waveguide-mounted oscillator and passes through the quasi-optical isolator before reaching the diplexer.

The signal and LO overlayed by the diplexer is then received by a corrugated horn and fed into the waveguide-mounted mixer, designed by Dr. Nigel Cronin, as a piece of stripline mounted in the waveguide couples the power onto a planar Schottky diode. The position of the mixer back-short and the bias current through the diode can be adjusted to optimise the sensitivity of the mixer. Down-converted signal is removed via an RF choke. The signal is bandpass filtered and amplified at an IF frequency of 3.8 GHz over a 100 KHz band.

The output of the receiver can be displayed on a spectrum analyser, whose ouput can be recorded by an auto-ranging digital filter bank. The signal can also be video-detected by a diode and a power meter used to average the received signal over the 100 KHz band.

8.3 Quasi-optical systems

The receiver's horns, lenses, grids and ferrite rotator were designed and made using principles outlined in Chapter 2,3 and 4. There are two Martin-Puplett (MP) interferometers in the circuit: One overlays signal and LO, the othe acts as the SSB filter. In each, a polarizing grid splits and input beam into two orthogonally polarized beams. One of the beams

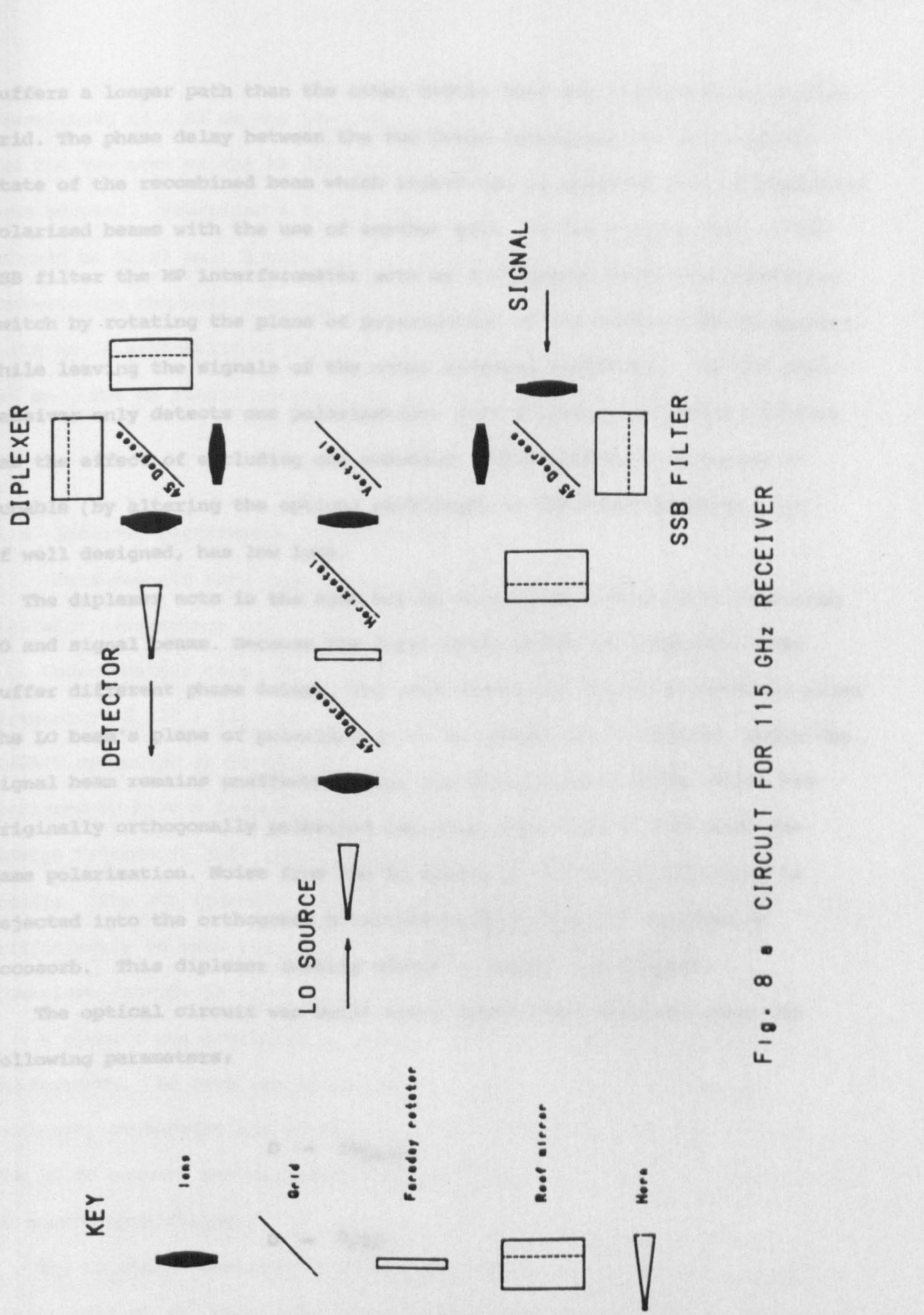

Fig. 8 • CIRCUIT FOR 115 GHz RECEIVER

suffers a longer path than the other before they are recombined by another grid. The phase delay between the two beams determines the polarization state of the recombined beam which itself can be resolved into orthogonally polarized beams with the use of another grid. In the simpler case of the SSB filter the MP interferometer acts as a frequency selective polarizing switch by rotating the plane of polarization of one sideband by 90 degrees while leaving the signals of the other sideband unaffected. As the basic receiver only detects one polarization, this frequency selective rotation has the effect of excluding one sideband. This method of filtering is tunable (by altering the optical pathlength in the interferometer) and, if well designed, has low loss.

The diplexer acts in the same way by overlaying orthogonally polarized LO and signal beams. Because the input beams differ in frequency, they suffer different phase delays. The path difference can be adjusted to allow the LO beam's plane of polarization to be rotated by 90 degrees, while the signal beam remains unaffected. Thus the LO and signal beams, which are originally orthogonally polarized can enter the detector horn with the same polarization. Noise from the LO source at the signal frequency is rejected into the orthogonal polarization by a grid and absorbed by Eccosorb. This diplexer ideally wastes no signal nor LO power.

The optical circuit was built using split-cubes designed using the following parameters:

$$D = 3W_{Lens}$$

$$U = 3/2D$$

where W_{Lens} is the beamwaist size in the lens, D the lens diameter and U the cube size. The receiver was designed to have an optimum performance at 115 GHz with an LO source operating at 111 GHz. A mean value of the

wavelength of 2.65 mm was adopted. To ensure no extra lenses were included in the two arms of the MP diplexer and filter a lens separation of 4 U(N=4) was adopted. Equations 5.2, 5.3 and 5.4 indicated that the cube size should be 68.35 mm. A cube size of 70 mm was chosen. The path difference between the channels required by the diplexer, to overlay a signal and LO with an IF separation of 3.8 GHz, needed a movable mirror displacement of 21 mm. The MP single sideband filter required half this displacement.

8.4 Receiver performance measurements.

Measurements were made of the loss between LO source and mixer, isolator performance and single sideband filter loss and rejection.

Unfortunately test signal sources were not available at the designed frequency of 110 - 115 GHz. Measurements were therefore taken using an IMPATT operating at 98 GHz as a source. The size of lenses had been designed to have a diameter of 3 times the lens beamwaist size at the design frequency, just large enough not to truncate the beams significantly. The 10% increase in wavelength increased the lens beamwaist size sufficiently to make truncation significant. Measurements at 98 GHz therefore provide an upper limit to losses.

A circuit was developed to measure LO chain losses and isolator performance. LO from the 98 GHz IMPATT passed through a waveguide isolator, attenuator and 10 dB coupler before entering the source horn. The 10 dB coupler was calibrated and then used to measure the power at the LO source horn flange.

The LO chain consisted of a corrugated feed horn set with its polarization axis at 45° which generated a diagonally polarized beam. This beam was picked by the first lens and then passed through a grid set at 45°. The first lens formed a waist at the matched ferrite rotator. The polarization axis was rotated through 45 degrees by the ferrite and a

second lens picked up the beam, now horizontally polarized, and reflected it off a vertical grid. It then passed through a third lens and into the Martin-Puplett diplexer. The LO finally passed through a fourth lens into the detector horn and power meter.

The loss through the LO chain was measured to be 5.0 ± 0.1 dB. The ferrite rotator was reversed and the loss in the chain rose to 25 dB indicating that isolation of about 20 dB was provided by the isolator. When the ferrite rotator and diagonal grid were removed, and the source horn rotated to generate a horizontally polarized beam, the LO chain loss dropped to 3.5 dB, indicating that the ferrite rotator loss was 1.5 dB.

The performance of the Martin-Puplett single sideband filter (SSB) was measured radiometrically. The receiver was operated using the 98 GHz IMPATT as the LO source in the configuration outlined above. The loss of the filter was measured as follows: first a piece of Eccosorb mm-wave absorber at room temperature, acting as a warm load, was inserted into the input beam before the filter and the receiver output zeroed. The room temperature Eccosorb was then replaced by a similar piece of Eccosorb soaked in liquid nitrogen - this acted as a black body at 77 K. The change in output from the receiver, in dB, was recorded. (This value is known as the Y factor.) The procedure was then repeated, but with the Eccosorb loads placed in front of the SSB filter, and the change in output again measured. The loss in the SSB filter including a lens, given by the reduction in signal detected, proved to be only 0.4 dB, a quite satisfactory result*.

The rejection of the MP SSB filter was measured using a tunable 102 - 110 GHz IMPATT as a source. (The tunable IMPATT was very noisy and therefore could not be used as an LO source.) It could be tuned to give an

*As the MP SSB filter is a polarization dependent device and the receiver only detects a single plane of polarization, the device has no filtering effect upon unpolarized signals, such as blackbody radiation.

output signal 3.8 GHz (the IF frequency) above the 98 GHz LO frequency. This line was observed using the receiver coupled to an HP spectrum analyser. The rejection provided by the SSB filter was determined by adjusting the moving mirror position to give the maximum line signal and then increasing the mirror's offset by a quarter wavelength to measure the drop in the line strength on the HP analyser. The rejection proved to be just over 20 dB.

The MP SSB filter is a frequency-dependent device and therefore must be correctly adjusted for each new operating frequency: if the LO frequency is changed the position of the moving mirror of the filter must also be adjusted.

A method for making this adjustment was devised which used the standard type of SSB filter - a dichroic plate formed by drilling, in close pack formation, a large number of holes in a thin metal plate. Each hole acts as a circular waveguide, transmitting incident power arriving on one side of the plate to the other side. The hole diameter is chosen so that the lower sideband is just below the circular waveguide cutoff frequency and the upper sideband is just above the cutoff frequency. The plate acts as a band pass filter. SSB filters of this form are quite easy to make using an NC milling machine which can be programmed to produce the large number of holes required automatically.

The MP SSB filter can be set up in the following way. A dichroic filter, with a cut-on close to the LO frequency, is placed at the input to the MP SSB filter and a broadband source, such as a liquid nitrogen saturated piece of Eccosorb placed in front of it. The adjustable mirror of the MP SSB filter is then moved to give the maximum output from the receiver. The receiver is then set for upper sideband operation. If lower sideband operation is required, the procedure is the same, but minimum signal output is looked for.

8.5 Conclusion

A 115 GHz receiver in which the quasi-optical techniques developed in this thesis were used to give low signal throughput loss, adjustable SSB filtering and LO isolation has been built. The performance of the quasi-optical components is good and the receiver is to be used in atmospheric and astronomical studies, making use of the receiver's all solid state operation.

CHAPTER 9

CONCLUSION

The quasi-optical circuit approach to the design of millimetre-wave systems, developed in this thesis, has proved to be a practical method for the construction of high bandwidth, low loss millimetre wave instruments.

Gaussian beam-mode analysis has been the main analytical tool used in this work. The maximum throw notion of propagating Gaussian beam-modes defines the minimum size of quasi-optical circuits, and leads directly to the split cube building block method of accurately positioning components. Corrugated feed horns are near-ideal Gaussian beam-mode launchers and their operation can be understood using Gaussian beam-mode analysis. Wire polarizing grids split and re-combine propagating beams and act as signal processing elements. Networks constructed with such grids can be analysed using Jones matrices. An example of this approach has been demonstrated in chapter 6 where Jones matices have been applied to the operation of the null reflectometer.

Isolators, used to suppress reflections in circuits, are all the more necessary in millimetre-wave quasi-optical systems with very high through-put and solid state sources subject to 'pulling'. Quasi-optical isolators, described in chapter 4, using hard ferrite Faraday rotators, which do not require bulky driving magnets, look promising and have a performance equal to that obtained at lower frequencies by waveguide isolators.

The performance of all of these devices, although capable of improvement and reduction in manufacturing cost, do not limit the performance of circuits. The current constraint is provided by reflections back into the fundamental Gaussian beam-mode from lens surfaces. These cause standing waves in and between lenses which distort measurements. The various techniques for reducing the problem - tuning the thickness of the lenses, blooming the surface or blazing the surface by cutting circular grooves

into it, and construction of lenses using low refractive index material, have some effect, but no technique is yet completely satisfactory. The problem is mainly a practical one of finding suitable materials and processes, although there are some theoretical questions concerning the application of Fermat's principle over surfaces whose radius of curvature is of the order of a wavelength or less. Work is continuing in this area.

Man's desire to understand and modify the world about him has led him to use all parts of the electromagnetic spectrum. The millimetre region has applications to many fields ranging from cosmology and nuclear fusion to communications and remote sensing of weather from space. Quasi-optical techniques will no doubt play their part in this growing area of interest.

APPENDIX I

THE DISPERSION OF MODES IN CORRUGATED GUIDE

The conditions for which modes in corrugated guide will propagate are of importance in the design of waveguide-fed horns (Chapter 2) and single mode back-to-back horns (Chapter 7).

For m = 1 modes (i.e. $HE_{1,n}$ or $EH_{1,n}$) the dispersion equation is (see Chapter 2):

$$k_c a \cdot \frac{J_1'(k_c a)}{J_1(k_c a)} - \frac{(\beta')^2 J_1(k_c a)}{k_c a\, J_1'(k_c a)} = -\frac{(k_c a)^2}{k_o a} \cdot \frac{Z_o}{X_{slot}} \qquad (I.1)$$

where $$X_{slot} = \left[\frac{J_1(k_c a)Y_1(k_o b) - J_1(k_o b)Y_1(k_o a)}{J_1'(k_c a)Y_1(k_o b) - J_1(k_o b)Y_1'(k_o a)} \right] Z_o \quad .$$

γ, the TE to TM amplitude ratio, is given by

$$\gamma = -\frac{\beta' J_1(k_c a)}{k_c a\, J_1'(k_c a)} \quad . \qquad (I.2)$$

(HE modes are distinguished from EH modes by the fact that γ is positive rather than negative.)

The dispersion relations (Plots of βa against $k_o a$) for modes in corrugated guide would be complex enough if X_{slot} was fixed. However the fact that X_{slot} does depend upon $k_c a$ makes the intuitive understanding of (I.1) very difficult. To reduced the complexity we look at points on the dispersion curves where special conditions prevail. The conditions we are interested in are the cut-off conditions when $\beta = 0$ or ∞, the balanced hybrid condition when $\gamma = \pm 1$ and the fast to slow wave transition where $\beta' = 1$. Fig. I.1, taken from Fig. 2 of [I.1] gives in part (d) the parametric dependence of these special points as well as dispersion curves for three values of b/a.

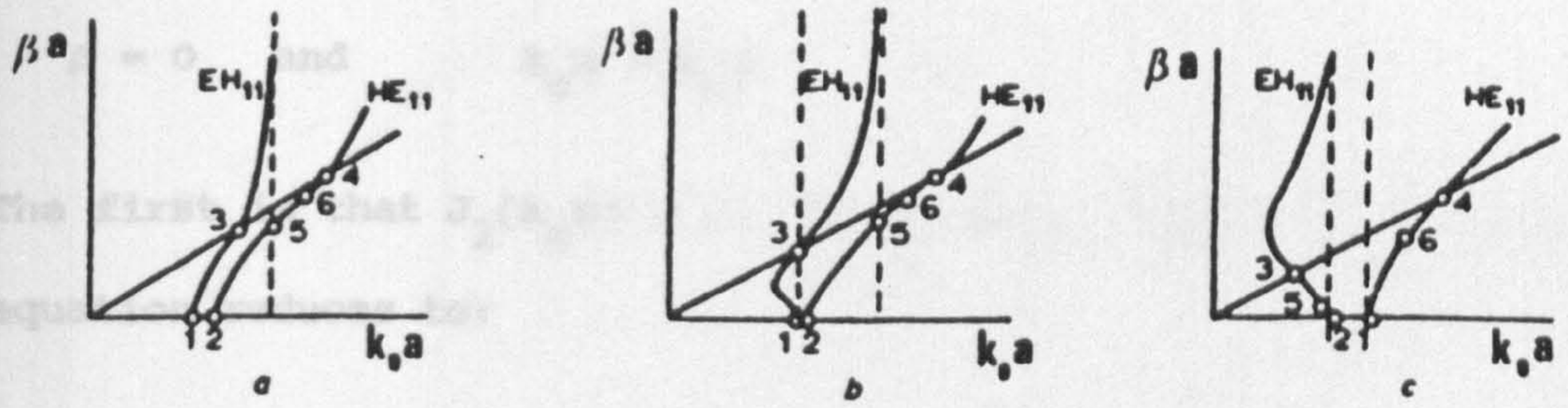

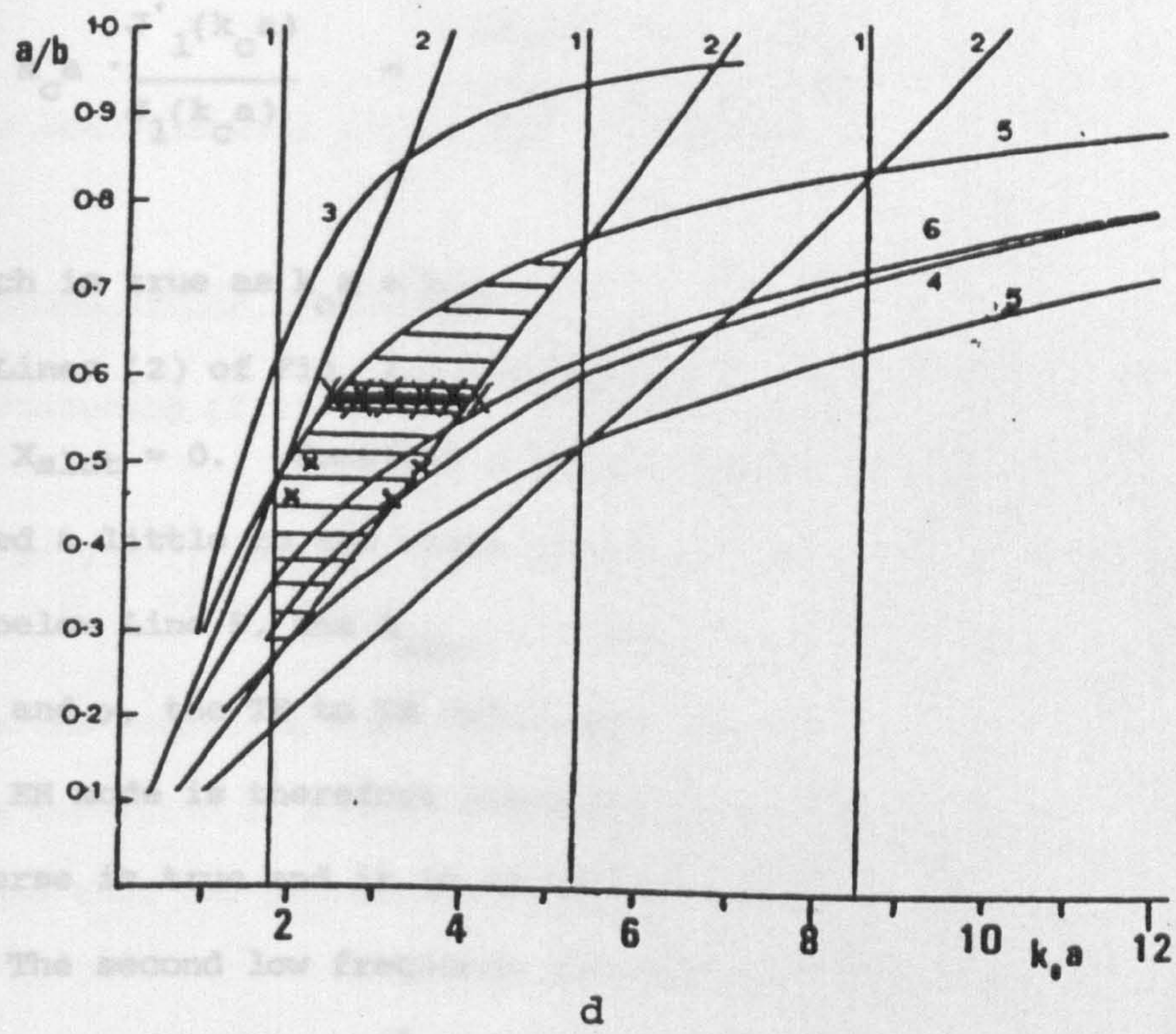

. Propagation characteristics for corrugated waveguide.

a-c. Dispersion diagrams for corrugated waveguide.

a. a/b = 0.9 b. a/b = 0.63 c. a/b = 0.4

d. Parametric dependence of special points.

Points 1 and 2 represent cutoff for modes with $E_z = 0$ and $H_z = 0$, respectively, at $\beta = 0$.

Points 3 and 4 represent condition $\tilde{\beta} = \beta/k_o = 1$, $X_{slot} = \frac{2Z_o}{k_o a}$.

Point 5 represents balanced hybrid or "open-circuit" boundary condition $X_{slot} = \infty$.

Point 6 represents short-circuit boundary condition $X_{slot} = 0$.

Fig. I.I

Low frequency cut-off conditions

There are two low frequency cut-off conditions which occur when

$\beta = 0$ and $k_c a = k_o a$

The first is that $J_1(k_o b) = 0$. Then, as $J_1'(k_o a) \neq 0$, the dispersion equation reduces to:

$$k_c a \cdot \frac{J'_1(k_c a)}{J_1(k_c a)} = \frac{(k_c a)^2}{k_o a} \left[\frac{J'_1(k_c a)}{J_1(k_c a)} \right] \qquad (I.3)$$

which is true as $k_c a = k_o a$.

Lines (2) of Fig. I.1 correspond to $J_1(k_o b) = 0$ and lines (5) are for $X_{slot} = 0$. Consider a point on Line (2) and suppose it is moved a little to the right (put $k_o a \to k_o a + \delta$). If the point is below Line 5, the $X_{slot} < 0$ (see Fig. (I.2). Thus $\frac{J'_1(k_c a)}{J_1(k_c a)}$ will be +ve and γ, the TE to TM ratio must be -ve.

The EH mode is therefore starting to propagate. Above Line (5) the reverse is true and it is an HE mode which is cut-on.

The second low frequency cut-off condition is slightly harder to understand. Suppose $J_1'(k_o a)$ equals 0. Then as $\beta' \to 0$, there must be some β', however small, such that

$$\frac{\beta'^2 J_1(k_c a)}{k_o a \; J'_1(k_c a)} = \frac{-(k_c a)^2 Z_o}{k_o a \; X_{slot}}$$

Then if $X_{slot} < 0$, $\frac{J_1(k_c a)}{J_1'(k_c a)}$ will be +ve and an EH mode will be cut on.

The converse also applies. Lines (1) correspond to this condition.

Thus one has cut-off's of the form (Fig. I.2)

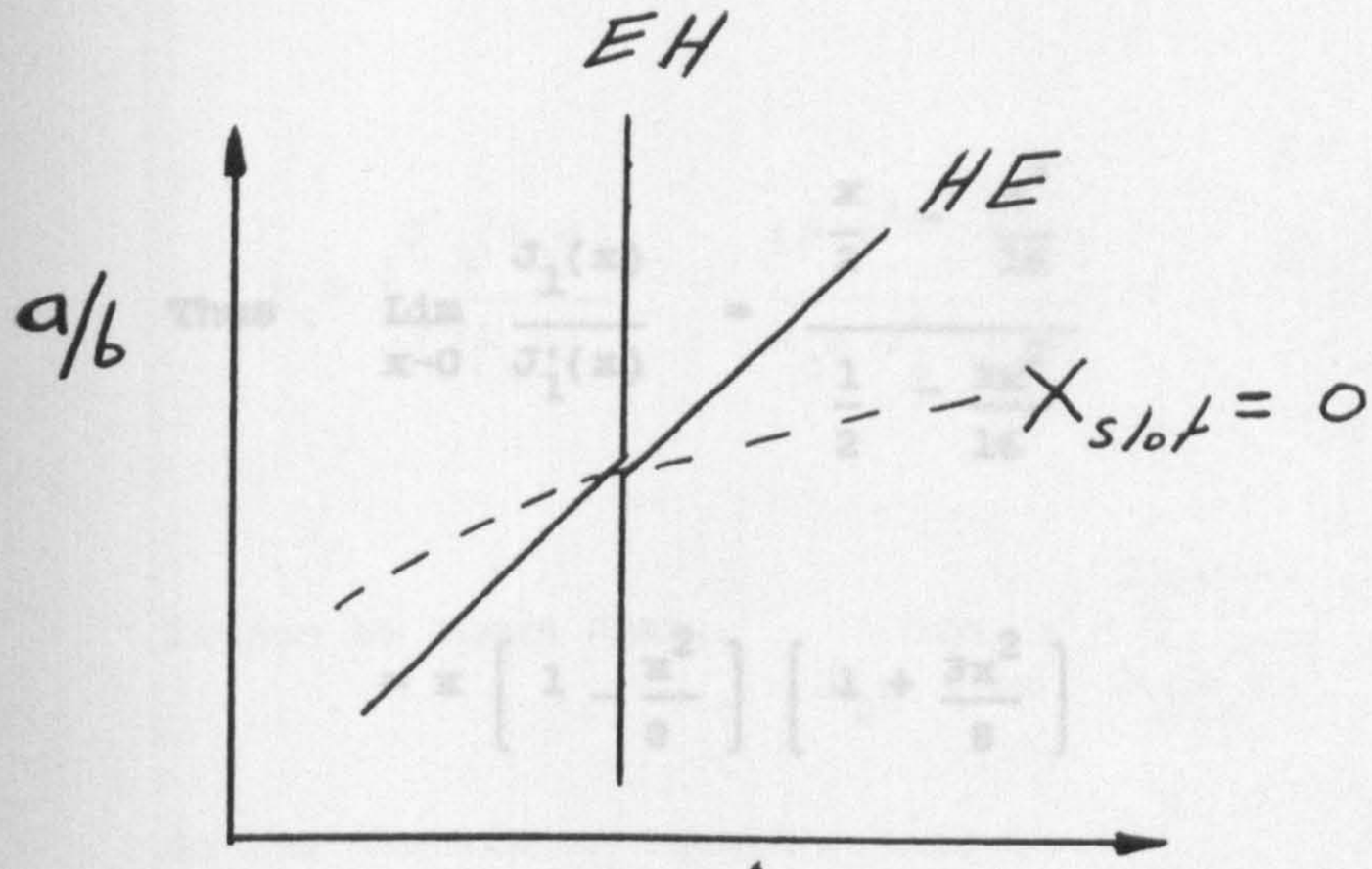

Fig. I2

This analysis will also apply for m ≠ 1.

Balanced Hybrid conditions ($\gamma = \pm 1$)

Substituting (I.2) into (I.1) gives

$$\beta' \left[\gamma - \frac{1}{\gamma}\right] = \frac{-\left[k_c a^2\right]}{k_o a} \left[\frac{Z_o}{X_{slot}}\right] . \qquad (I.4)$$

Thus the condition for γ to be ± 1 is that $X_{slot} = \infty$ (Lines (5)).

This condition is required at the aperture of radiating horns to ensure that the radiation pattern of the HE_{11} mode as axially symmetric.

The slow to fast wave transition ($\beta' = 1$)

It is well known that

$$J_n(x) = \sum_{r=0}^{\infty} \frac{(-1)^r \, (x/2)^{n+2r}}{r! \, \Gamma(n+r+1)} , \qquad (I.5)$$

$$\text{so} \quad J_1(x) = \frac{x}{2} - \frac{x^3}{16} \ldots\ldots , \qquad (I.6)$$

$$\text{and} \quad J_1'(x) = \frac{1}{2} - \frac{3x^2}{16} \ldots\ldots . \qquad (I.7)$$

$$\text{Thus} \quad \lim_{x \to 0} \frac{J_1(x)}{J_1'(x)} = \frac{\frac{x}{2} - \frac{x^3}{16}}{\frac{1}{2} - \frac{3x^2}{16}} \qquad \text{(I.8)}$$

$$\simeq x \left[1 - \frac{x^2}{8} \right] \left[1 + \frac{3x^2}{8} \right]$$

$$\approx x \left[1 + \frac{x^2}{4} \cdots \right] .$$

Using this result and substituting $\beta' = 1$ into equation (I.1) we have

$$k_c a \left\{ \frac{1}{k_c a \left[1 + \frac{(k_c a)^2}{4} \right]} \right\} - \frac{(1)^2 \, k_c a \left[1 + \frac{(k_c a)}{4} \right]^2}{k_c a} = - \frac{(k_c a)^2}{k_o a} \frac{Z_o}{X_{slot}} . \qquad \text{(I.9)}$$

I.9 is satisfied if:

$$X_{slot} = \frac{2 Z_o}{k_o a} \qquad \text{(Lines (3) and (4))}$$

<u>High frequency cut-off ($\beta = \infty$)</u>

When $\beta' > 1$ a mode becomes a surface wave and the field is concentrated at the surface of the guide, where it suffers ohmic losses and decays. However the high frequency cut-off occurs when $\beta = \infty$ and $k_c a = -i\infty$.

Returning to the main dispersion equation (I.1) we have

$$k_c a \cdot \frac{J'_1(k_c a)}{J_1(k_c a)} - \frac{(\beta')^2 J_1(k_c^2 a)}{k_c a\, J'_1(k_c a)} = -\frac{(k_c a^2)}{k_o a} \cdot \frac{Z_o}{X_{slot}} \qquad \text{(I.1 bis)}$$

It can be shown that $\lim_{k_c a \to i\infty} \frac{J_o(k_c a)}{J_1(k_c a)} \to -i$.

So the dispersion equation becomes

$$k_c a \cdot -i - \frac{\left[\frac{k_c a}{k_o a}\right]^2 \left[\frac{1}{-i}\right]}{k_c a} = -\frac{(k_c a)^2}{k_o a} \frac{Z_o}{X_{slot}} \cdot$$

$$X_{slot} = Z_o \frac{k_c a}{k_o a} \frac{1}{i\left[1 - \frac{1}{(k_c a)^2}\right]}$$

for $k_c a \to i\infty$.

Thus $X_{slot} = \infty$ is the high frequency cut-off condition (Lines (5)).

<u>The form of the dispersion curves</u>

The group velocity of any wave must not exceed the speed of light.

Then as $\frac{\omega}{k_o} = c$ so $\frac{\partial \beta}{\partial k_o} \geq 1$ and $\frac{\partial \beta\, r}{\partial k_o\, r} \geq 1$.

Thus a curve on the dispersion graph that has a gradient of less than 1 is not allowed. This argument insures that there exists only one values of $k_o a$, for each mode, which gives $\beta' = 1$. Consider the case of a piece of corrugated guide excited by a variable frequency source. It can be shown that, if $k_o a > 2.5$, $X_{slot} = \tan k_o d$ where d is the depth of the slots. As the frequency is increased the reduced depth of the slots increases and the slot impedence X_{slot} changes:

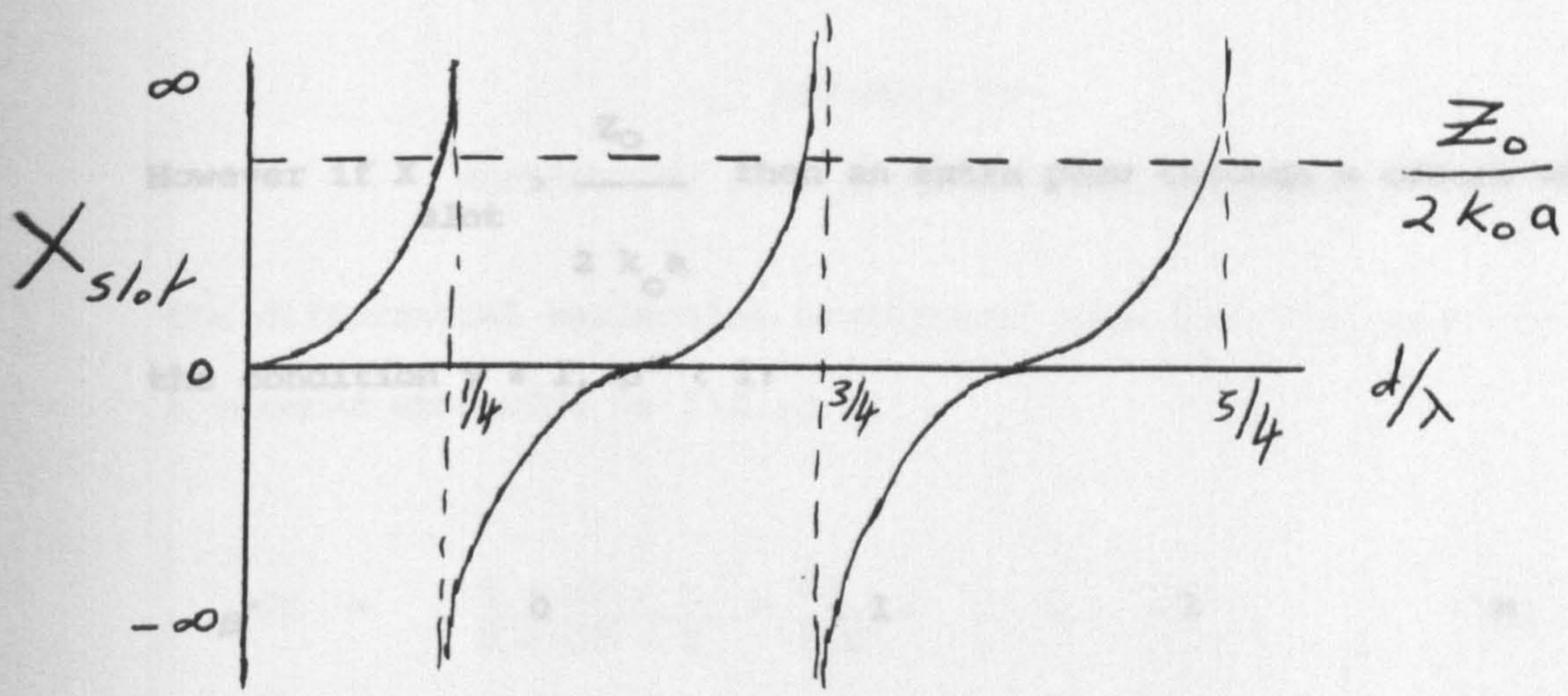

For each mode, the dispersion curve must start at $\beta = 0$. There are two ways in which β' can change:

If $X_{slot} < \frac{Z_o}{2k_oa}$ at cut-on then the β' will move:

	Cut-on		Cut-off
β'	0	1	∞
X_{slot}	$> \frac{Z_o}{2k_ca}$	$\frac{Z_o}{2k_ca}$	$-\infty$

An example of this is the EH_{11} dispersion curve for $a/b = 0.9$ (Fig. I.1 a). This ensures that the EH_{11} mode which has a lower cut-off frequency than the HE_{11} mode, is not present at the aperture of corrugated horns as its high frequency cut-off is reached before the guide has tapered up to the aperture.

However if $X_{slot} > \frac{Z_o}{2 k_o a}$ then an extra pass through ∞ occurs which gives the condition $\gamma \pm 1$, $\beta' < 1$:

β'	=	0	< 1	=	1	=	∞
X_{slot}	$<$	$\frac{Z_o}{2 k_o a}$	$-\infty/\infty$		$\frac{Z_o}{2 k_o a}$		$-\infty$

This argument shows that each mode has either one, or a maximum of two β' values when $Z_{slot} = \infty$ and that there are propagating HE and EH modes for $k_c a$ when $Z_{slot} = \infty$ if

$$X_{slot} > \frac{Z_o}{2 k_o a}$$ when the modes are cut-on.

Conclusion

The dispersion curves of corrugated guide are complex but their comprehension can be aided by an examination of the parametric dependence of special points. By an examination of where modes suffer low and high frequency cut-off it can be shown that the shaded area in Fig. I.1 d is HE_{11} single moded. Dimensions of the transition sections of corrugated horns (Chapter 2) are chosen to place operation in the shaded area to ensure that no other modes are excited. As the guide is tapered up the slot depth is reduced to give the required balance hybrid conditions at the aperture. The waveguide at the centre of the back-to-back horn described in Chapter 7 operates on the line marked XXXXXXX in Fig. I.1 d. This position was chosen to give a wide single-mode bandwidth.

APPENDIX II

REFLECTIONS FROM A TAPERED SMOOTH WAVEGUIDE

The differential reflection coefficient back into the same mode of a tapered waveguide is [II.1]

$$d\Gamma = \frac{Z + dZ - Z}{Z + dZ + Z} \approx \frac{dZ}{2\,Z} = \frac{1}{2}\, d(\ln Z) \quad , \qquad (II.1)$$

where Z is the impedence of the guide.

At the input to the taper, of length l, the contribution to the reflection will be

$$d\Gamma = e^{-i2\left[\int_0^z \beta(z')dz'\right]} \frac{1}{2} \frac{d(Ln\ Z)}{dz}\, dz \quad , \qquad (II.2)$$

where β is the forward wave-vector in the guide. The factor 2 comes from the double path taken by the reflected wave. The reflection from the guide is

$$\Gamma = \int_0^l e^{-i2\left[\int_0^z \beta(z')dz'\right]} - \frac{1}{2} \frac{d(Ln\ Z)}{dz}\, dz \, . \qquad (II.3)$$

Put $-\frac{1}{2}\,\frac{1}{Z}\,\frac{dZ}{dz} = k_{n,-n'}$ the fundamental mode reflection coefficient.

The impedence of a rectangular guide of major axis a and minor axis b for the fundamental TE_{01} mode is given by:

$$Z_n^{TE_{01}} = \frac{\pi^2}{8}\,\frac{b}{a}\left[\frac{\mu_o}{\epsilon_o}\right]^{1/2}\left[1 - \left[\frac{\pi}{k_o a}\right]^2\right]^{-1/2} , \qquad (II.4)$$

where k_o is the free space wavenumber. Then

$$k_{n,-n}^{TE_{01}} = -\frac{1}{2}\left[1-\left[\frac{\pi}{k_o a}\right]^2\right]^{1/2} \cdot -\frac{1}{2}\left[1-\left[\frac{\pi}{k_o a}\right]^2\right]^{-1.5} \cdot -\frac{\pi^2}{k_o^2} - \frac{2}{a^3} \cdot \frac{da}{dz} \cdot \qquad \text{(II.5)}$$

which reduces to

$$k_{n,-n}^{TE_{01}} = -\frac{1}{2}\left[\frac{k_o^2}{\pi^2} - \frac{1}{a^2}\right]^{-1} \frac{G}{a^3} \quad , \qquad \text{(II.6)}$$

where $G = \frac{da}{dz}$, the gradient of the taper.

It has been assumed that $\frac{b}{a}$, the ratio of guide width to height, does not vary along the taper. Consider the case of a circular smooth guide, of radius r_o, excited in the fundamental TE_{11} mode. The cut-off occurs when $k_c r_o = 1.8412$ instead of $k_c a = \pi$ for the TE_{11} mode. Thus it is reasonable to expect that substituting $\frac{1.8412}{\pi} r_o$ for a should give the fundamental mode reflection coefficient for circular guide as

$$k_{n,-n}^{TE_{11}} = -\frac{1}{2}\left[\frac{k_o^2}{\pi^2} - \frac{(1.8412\ a)^2}{\pi^2 a^2}\right]^{-1} \frac{(1.8412)^3\ G}{\pi^3 a^3} \quad . \qquad \text{(II.7)}$$

Note that G here refers to the radius of the guide.

Equations (II.3) and (II.7) have been programmed into a computer and used to predict reflection from a smooth horn transition of the same form as the CBS IB antenna. The results are presented as a function of frequency in Fig. II a. They indicate that at a frequency of 130 GHz a smooth CBS waveguide taper would reflect 2% and at higher frequencies less than 2% back into the fundamental Gaussian beam-mode. These calculations are for smooth rather than corrugated horns and can only provide a guide to the actual reflectivity of the CBS corrugated taper which was thought too complex to calculate analytically.

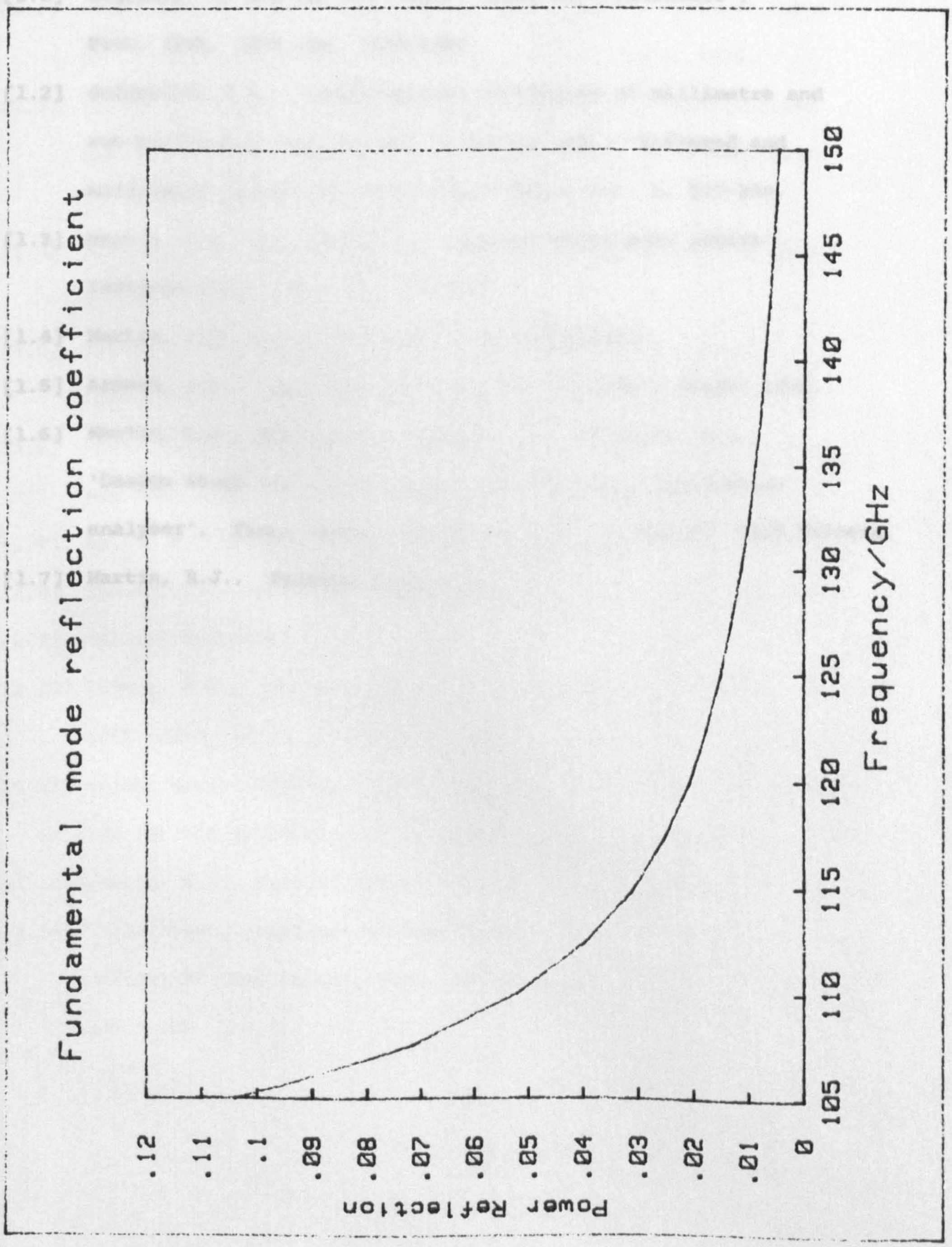
Fundamental mode reflection coefficient
Power Reflection
.12
.11
.1
.09
.08
.07
.06
.05
.04
.03
.02
.01
0
105
110
115
120
125
130
135
140
145
150
Frequency/GHz

Fig. IIa

REFERENCES

[1.1] Kogelnik, H. and Li, T., 'Laser beams and resonators', Proc. IEEE, 1966, 54, 1312-1325

[1.2] Goldsmith, P.F., 'Quasi-optical techniques at millimetre and sub-millimetre wavelengths' in Button (ed.) "Infrared and millimetre waves" (Academic Press 1982), Vol. 6, 227-338.

[1.3] Martin, D.H. and Lesurf, J., 'Submillimetre-wave optics', Infrared Phys. 1978, 18, 405-412.

[1.4] Martin, D.H. Lecture Notes (to be published).

[1.5] Arnaud, J.A., 'Beam and Fibre Optics' (Academic Press) 1976.

[1.6] Martin, D.H., Martin, R.J., Maries, K. and Wylde, R.J., 'Design study for an 80-94 GHz quasi-optical polarisation analyser'. Final Report IL/MW22B/887/3 for MOD(PE), RSRE Malvern.

[1.7] Martin, R.J., Private Communication.

[2.1] Clarricoats, P.J.B. and Olver, A.D., 'Corrugated horns for microwave antennas' (Peter Peregrinus Ltd.) 1984.

[2.2] Petterson, L., 'Corrugated horns - A review'. Research Report No. 138, Chalmers University of Technology, Sept. 1979.

[2.3] Aubry, C. and Bitter, D., 'Radiation pattern of a corrugated horn in terms of Laguerre Gaussian functions', Electron.Lett., 11, 1975, 154-156.

[2.4] Mathews, J. and Walker R.L., 'Mathematical Methods of Physics' (Addison Wesley, 2nd edn.) 1973

[2.5] Thomas, B. Mac A., 'Design of corrugated conical horns', IEEE Trans. AP-26, 1978, 367-372.

[2.6] Love, A.W., ed. 'Electromagnetic horn antennas', IEEE Press, New York 1976

[2.7] Spiro, P., 'Electroforming', (Robert Draper) 1971.

[2.8] Thomson-CSF, Operating Instructions for Carcinotron Type CO20B.

[2.9] Mullard Technical Note 79:TP1664, 1978.

[2.10] Ludwig, A.C., 'The definition of cross polarization', IEEE Trans. AP-21, 1973, 116-119.

[2.11] Wylde, R.J., 'Feed horns for Gaussian beam optics above 100 GHz', 7th Int.Con.Infrared and Millimetre Waves, Marseille, Feb. 1983.

[2.12] Martin, R.J., Private Communication.

[2.13] Wylde, R.J., 'Millimetre-wave Gaussian beam-mode optics and corrugated feed horns', Proc.IEE, Vol. 131, Pt.H, No.4, Aug. 1984 258 - 262.

[3.1] Mok, C.L., Chambers, W.G., Parker, T.J. and Costley, A.E., 'The far infrared performance and application of free standing grids wound from 5 μm diameter tungsten wire', Infared Phys. 19, 1979, 437–442.

[3.2] Kogelnik, H., 'Coupling and conversion coefficients for optical modes', Polytechnic Ins. Brooklyn Symp. Quasi–opt., 1964, 333–347.

[3.3] ICI Technical service note p.137, fourth edition 'Propathene for structural foams'.

[3.4] Sekisui (UK) Ltd. Technical Information E10–1 'Alveolit'.

[4.1] Rughooputh, S.D.D.V., 'A ferrite isolation for the far infrared', QMC Physics Department Design project 680/0701, 1982.

[4.2] Helszajn, J., 'Non-reciprocal microwave junctions and circulators' (John Wiley) 1975.

[4.3] Mullard, 'Permanent magnets', Data sheet Sept. 1970.

[4.4] Polypenco, 'Flurosint' data sheet F1-8/82.

[4.5] Llewellyn-Jones, D.T., Knight, R.J., Moffat, P.H. and Gebbie, H.A., 'New method of measuring low values of dielectric loss in the near millimetre wavelength region using unturned cavities', IEE Proc. Vol.127, Pt.A, No.8, Nov. 1980.

[6.1] Fymat, A.L., 'Jones's Matrix representation of optical instruments I : Beam splitters', Applied Optics, Vol.10, Nov. 1971, 2499-2505.

[6.2] Martin, D.H. and Martin, R.J., 'Feasibility study for an 80 to 94 GHz quasi-optical polarisation analyser'. Report IL/MW22B/887/4 for MOD(PE), RSRE Malvern.

[7.1] Dicke, R.H., Peebles, P.J.E., Roll, P.G. and Wilkinson, D.T., 'Cosmic black-body radiation'. Astrophys.J. 142, 414, 1965.

[7.2] Penzias, A.A., Wilson, R.W., 'A measurement of excess antenna temperature at 4080 mc/s'. Astrophys.J. 142, 1965, 419.

[7.3] Rowan-Robinson, M., 'Cosmology' Ch.5 (Clarendon Press, Oxford) 1977.

[7.4] Martin, D.H., 'Millimetre-wave cosmic background measurements' SERC Grant Application, March 1979.

[7.5] Martin, D.H., 'Polarizing (Martin-Puplett) Interferometric Spectrometers for the near and submillimetre spectra'. In Button (ed.) 'Infrared and Millimetre Waves' (Academic Press 1982), Vol.6, 65-148.

[7.6] Hinterberger, H. and Winston, R., 'Efficient light coupler for Threshhold Cerenkov Counters', Rev.Sci.Hist. 37, 2, 1966, 1094-1095.

[I.1] Clarricoats, P.J.B. and Saha, P.K., 'Propagation and radiation behaviour of corrugated feeds'. Proc. IEEE Vol. 118, Sept. 1971, 1167-1176.

[II.1] Collin, R.E., 'Foundations of microwave engineering' section 5.12 (McGraw-Hill Kodokusha Ltd.) 1966.